Transport and Kinetic Phenomena Linked to Power Performance of Lithium-Ion Batteries

by

Sang Woo Han

A dissertation submitted in partial fulfillment
of the requirements for the degree of
Doctor of Philosophy
(Mechanical Engineering)
in the University of Michigan
2014

Doctoral Committee:

Emeritus Professor Ann Marie Sastry, Co-Chair
Professor Wei Lu, Co-Chair
Associate Professor Christian M. Lastoskie
Assistant Research Scientist Jonghyun Park
Professor Margaret S. Wooldridge

DEDICATION

To My Parents

ACKNOWLEDGEMENTS

I would like to express gratitude and respect to my advisor Dr. Ann Marie Sastry for her guidance and support. I thank her for giving an opportunity to learn about the fascinating Li-ion battery technology, an energy storage system that could drastically ease pollution and energy shortage problems around the globe. Her tireless energy, persistent pursue for excellence, detail, and *good* science are characters that I will aspire to. I would also like to thank assistant research scientist Dr. Jonhyun Park for his availability for discussion. Working with them, not only I gained skills to tackle fundamental science and engineering problems but also lifelong professional skills.

I thank Professors Wei Lu, Margaret Wooldridge, and Christian Lastoskie for their time and service on my dissertation committee. Your support and valuable discussions are greatly appreciated.

I would also like to thank both current and former members of Sastry and Lu Groups, Dr. HyonCheol Kim, Dr. Xiangchun Zhang, Dr. Myoungdo Chung, Dr. Min Zhu, Dr. Dong Hoon Song, Dr. Jeong Hun Seo, Dr. Greg Less, Dr. Ethan Eagle, Dr. Joseph Gallegos, Dr. Sangmin Lee, Dr. Seungjun Lee, Mr. Hosop Shin, Mr. Yoonkoo Lee, Mr. Xianke Lin, and Mr. Guangyu Liu. Thank you all for many helpful discussions and support. Also I would like to thank Ms. Leah Wright, Ms. Nichole Washington, and Ms. Eve Bernos for their kind assistance and availability.

Thank you to all of my friends whom I met in Ann Arbor. Although many of you already left Ann Arbor, I cherish all the memories I shared with you all and hope to see you soon outside Ann Arbor. I would also like to thank members at Friday Tennis Club. With all the fun I shared with you all, both on and off tennis courts, you guys made Friday a long-awaited day of the week in the past year.

Above all, I would like to express my deepest gratitude to my family. My family's unconditional support has sustained me through this endeavor. Thank you Mom, Dad, Grandma, Kristine, and Janet, brother-in-laws, Justin and Yongtae, and adorable nephews, Andrew and Ethan.

I gratefully acknowledge the support of my research sponsors, including the U.S. Department of Energy through the BATT program and General Motors Corporation.

TABLE OF CONTENTS

LIST OF TABLES

LIST OF FIGURES

LIST OF SYMBOLS

c	lithium concentration	$mol \cdot m^{-3}$
C_p	specific heat capacity	$J \cdot kg^{-1} \cdot K^{-1}$
D	diffusion coefficient in the electrolyte phase	$m^{2} \cdot s^{-1}$
E	Young's modulus	Pa
E_a	activation energy	$J \cdot mol^{-1}$
$f_{\pm}$	mean molar activity coefficient	-
F	Faraday number	96,487 $C \cdot mol^{-1}$
h	heat transfer coefficient	$W \cdot m^{-2} \cdot K^{-1}$
j	local current density	$A \cdot m^{-2}$
k	reaction rate constant	$m^{5/2} s^{-1} \cdot mol^{-1/2}$
K	planar thermal conductivity	$W \cdot m^{-1} \cdot K^{-1}$
q	volumetric heat generation rate	$W \cdot m^{-3}$
r_p	spherical particle radius	m
R	universal gas constant	8.314 $J \cdot mol^{-1} \cdot K^{-1}$
S_a	specific surface area	m^{-1}
t_+	cationic transference number	-
T	temperature	K
U	open circuit potential	V
z	charge number	-
Greek symbols		
β	symmetry factor	-
ε	volume fraction	-
γ	Bruggeman constant	-
μ	chemical potential	$J \cdot mol^{-1}$
η	surface overpotential	V
Ω	partial molar volume	$m^{3} \cdot mol^{-1}$

κ	ionic conductivity in the electrolyte phase	$S \cdot m^{-1}$
σ	electronic conductivity in the electrode phase	$S \cdot m^{-1}$
Φ	electrode electric potential	V
ρ	density	$kg \cdot m^{-3}$
ν	Poisson's ratio	-

Subscripts

e	electrolyte phase
eff	effective
env	environment
f	filler
g	grain domain
gb	grain boundary domain
h	hydrostatic
pos	positive electrode
loc	local
max	stoichiometric maximum
neg	negative electrode
s	solid or electrode phase
surf	electrode surface
v	void space

LIST OF ABBREVIATIONS

AFM	Atomic Force Microscopy
DEC	Diethyl Carbonate
DOD	Depth-of-Discharge
DMC	Dimethyl Carbonate
EC	Ethylene Carbonate
ECM	Equivalent Circuit Model
EIA	Energy Information Administration
EIS	Electrochemical Impedance Spectroscopy
EPA	Environmental Protection Agency
EV	Electric Vehicle
HEV	Hybrid Electric Vehicle
OCP	Open Circuit Potential
PVdF	Poly Vinylidene Fluoride
SEI	Solid Electrolyte Interphase
SEM	Scanning Electron Microscopy
SOC	State-of-Charge
USABC	United States Advanced Battery Consortium
VC	Vinyl Carbonate
XPS	X-ray Photoelectron Microscopy

ABSTRACT

While energy density of a Li-ion cell depends on the choice of Li-ion active materials, power density depends on cell design and a set of well-balanced transport and kinetic material properties. Furthermore, the Li-ion cell rate capability improvement often comes at the expense of underutilizing available energy due to safety and cycle-life constraints. Hence, in this study, various transport and kinetic phenomena occurring inside a cell are examined to optimize the cell power performance.

Lithium-ion battery active materials are polycrystalline consisting of crystallites of varying size and orientation separated by grain boundaries. To investigate the grain boundary influence on battery performance, a single polycrystalline particle Li-ion cell model is developed. A Voronoi grain size distribution is employed in generating polycrystalline particles. Under galvanostatic and potentiodynamic cycling conditions, intercalation-induced stress, effective Li^+ diffusivity, and capacity utilization are examined. It is found that the effective Li^+ diffusivity is highly correlated with the grain boundary density while the maximum intercalation-induced stress depends on both the grain boundary density and the network structure. In addition, the particle capacity utilization improves with increasing grain boundary density, especially at high C-rates.

During cycles, many Li-ion active materials undergo a volumetric strain that may cause the material to fracture. On the other hand, the stress field has a benefit of enhancing Li^+ diffusivity inside active materials. To estimate the intercalation-induced

stress level, an *in-situ* AFM system is utilized in measuring particle morphological changes during cycles. Furthermore, a numerical method is used to quantify the Li^+ diffusivity enhancement caused by the intercalation-induced stress field.

The rate capability of a Li-ion cell depends on multiple transport and kinetic phenomena occurring inside the cell, and the rates at which such phenomena occur depend on cell material properties. To understand how a cell electrochemical dynamic response changes with material properties, a sensitivity analysis of transport and kinetic parameters on cell performance is performed. It is found that different types of material properties have a significant influence on specific parts of a cell operating potential profile. Moreover, given a set of material properties, associated overpotentials are quantified.

CHAPTER I

INTRODUCTION

LI-ION RECHARGEABLE BATTERY: APPLICATIONS AND BENEFITS

Nowadays people can carry a smartphone with a processing power (~1 GHz CPU) that is about a thousand times faster than the guidance computer used in the Apollo mission (~1 MHz CPU). With ever increasing computing power and portability of devices, people want to do more with their devices while being unplugged. To operate such devices unplugged, batteries are required. Although various types of rechargeable batteries are available, lithium-ion (Li-ion) rechargeable batteries dominate the market for consumer portable electronic devices because of their energy density, cost, and service life. Li-ion batteries are slowly being adopted in private transportations as well. Although Li-ion batteries cannot compete with internal combustion engines in terms of energy density and cost, Li-ion batteries are energy efficient and emission free in vehicles. According to the U.S. Environmental Protection Agency (EPA), about 15% of the total carbon dioxide (CO_2) greenhouse gas emission is from the ground transportation [1] in year 2011. The ground transportation sector is also a major source of air pollutant. For example, in China, the world's largest auto market since 2009, vehicular emissions account for as much as two-thirds and one-third of total carbon monoxide (CO) and nitrogen oxides (NOx) emissions in China, respectively [2]. The electrical grid system is another area where Li-ion batteries can play an important role. The current main grid system in the U.S. is approximately 100 years old and its annual maintenance cost is

steadily rising while becoming less reliable. According the U.S. Energy Information Administration (EIA), power outages of 100 megawatts or greater occurred, 156 times between 2000-2004, and 264 times between 2005-2009, excluding power outages due to natural disasters [3]. Li-ion batteries, therefore, could be used in individual homes for off-grid applications or as a part of a microgrid system in the event of power disruptions.

The use of Li-ion batteries may be beneficial in many ways. However, the technology requires improvements in various aspects. First, the energy density needs to be improved. The energy density of Li-ion batteries is improving approximately 10% a year. Battery researchers are, therefore, constantly looking for novel materials that could drastically increase the energy density. Secondly, the cost needs to be reduced, especially for vehicle applications. The United States Advanced Battery Consortium (USABC) targets the cost to be about <$150/kWh [4] from the current cost of about >$400/kWh. Thirdly, safety needs to be improved. The organic electrolyte used in Li-ion batteries is exothermic in nature. Hence, when a cell temperature rises above ~90 °C [5] or a cell becomes short-circuited due to an accident, it could quickly catch on fire and lead to an explosion. For vehicle applications, Li-ion batteries need to perform well in extreme temperatures too. In general, when a cell operating temperature is above 50 °C the cell capacity rapidly diminishes [6-7] and below −20 °C the cell performance drastically reduces [8]. Finally, the cell cycle- and calendar-life need to be improved. Because capacity fading mechanisms are often very complex, the related research is quite active within the Li-ion battery research.

LI-ION BATTERY RESEARCH OVERVIEW

According to the Nernst equation shown in Equation 1, the voltage (emf) measured across the anode and the cathode is equal to the difference of the lithium chemical potentials between the two electrodes.

$$V_{cell} = \frac{\mu_{+ve}^{Li} - \mu_{-ve}^{Li}}{zF} \quad (1)$$

The voltage measured across the two electrodes is often called the cell open circuit potential (OCP). In Eq. 1, V_{cell} is the cell OCP, μ^{Li} is the Li chemical potential expressed in $\text{J}\cdot\text{mol}^{-1}$, z is the charge number during an electrochemical reaction, and F is the Faraday's constant. A cell is called, a galvanic cell when the electrochemical reaction is spontaneous, and an electrolytic cell when input energy is required to generate the electrochemical reaction. When a cell is in a galvanic or current discharge mode, lithium ions are oxidized at the anode and transported to the cathode across the electrolyte while electrons move to the cathode via an external circuit. The lithium ions are then reduced at the cathode. This process is reversed in an electrolytic or current charge mode. The lithium ion insertion and extraction processes from the electrode are called intercalation and de-intercalation, respectively. The cell energy capacity is equal to the charge capacity of a cell, Q_{cell}, multiplied by the cell potential, V_{cell}. Since common negative electrodes such as graphite and silicon operate at potentials close to lithium redox potential, ~ 0.1 V vs. Li/Li^+, the V_{cell} is often dictated by the type of the cathode materials.

In a search for cathodes with a higher energy density, Li-ion battery researchers are focused on developing cathodes with a higher working potential. Promising high-voltage cathode materials include phosphates, spinels, and Li-rich layered oxides.

Examples of such materials are shown in Table 1.1. Cathodes listed in Table 1 exhibit a wide variety of crystal structures with a range of interstitial sites having one-, two-, and one-, two-, and three-dimensional lithium ion diffusion pathways. Phosphates have an olivine crystal structure [9] with one-dimensional (1D) lithium ion diffusion pathways. Although phosphates exhibit a high working potential with a high theoretical capacity, such materials typically have a low electronic conductivity (~10^{-9} $S \cdot cm^{-1}$) and a low Li^+ ionic conductivity relating to the 1D diffusion pathway [10]. The spinel $LiMn_2O_4$ is a popular cathode due to its environmental benignity, low cost, and safety. The Li^+ diffusion pathway in spinel materials is three-dimensional (3D), and hence, the spinel delivers a relatively high rate capability. However, it suffers from a structural instability, in which spinel irreversibly transforms to tetragonal phase caused by the Jahn-Teller distortion of Mn^{3+} and the dissolution of Mn ions in the electrolyte. However, when some of Mn ions are replaced with transition metals such as Ni, Cr, and Fe (e.g., $LiNi_{0.5}Mn_{1.5}O_4$ and $LiCr_yMn_{2-y}O_4$), the structural instability associated with Mn^{3+} diminishes and the average working potential increases leading to a higher energy density cathode material. Another promising class of cathodes is Li-rich layered oxides with the two-dimensional (2D) Li^+ diffusion pathways. It has a chemical formula of $xLi_2MnO_3 \cdot (1-x)LiMO_2$, where M may be Ni, Co, and Mn. This type of material exhibits an extreme high discharge capacity of 300 $mAh \cdot g^{-1}$. However, Li-rich layered structures are yet difficult to synthesize and undergo irreversible structure changes from a layered to a defect spinel which can lead to a lower capacity.

With the high voltage class of cathodes, the thermodynamic stability of electrolyte must improve as well. When an electrode operates outside stable potential window of an

electrolyte, its components will be reduced/oxidized near the electrode surface and the unnecessary solid electrolyte interphase (SEI) [18,19] will be formed on the active material surface. Although an SEI passive layer helps to contain electrons from being transferred to the electrolyte and prevent further side reactions, continuous formation of the SEI will consumes cyclable lithium ions as well as hinder facile lithium ions intercalation/deintercalation process. Therefore, a poor thermodynamic stability of the electrolyte will lead to accelerated cell capacity fading. The electrolyte used in Li-ion batteries can be broadly classified into three types: (i) organic or alkyl-carbonate-based, (ii) solid state, and (iii) ionic liquids (IL). An organic electrolyte consists of lithium salts (e.g., $LiPF_6$) dissolved in two or more carbonate-based solvents. Although the organic electrolyte typically exhibits a high ionic conductivity (1~10 $S{\cdot}cm^{-1}$) [20] at room temperature and forms a stable SEI layer on anode surface, it lacks stability at high temperature. The upper limit of stable potential window of organic carbonate solvents are about 5 V vs Li/Li^+. However, the transition metal ions tend to catalyze the oxidation of the electrolyte at about 4.5 V leading to the SEI formation on cathodes and lower the cell capacity. The solid state electrolyte, on the other hand, are stable at high temperatures and have a wider stable potential window. The solid state electrolyte may be further classified into three types – gelled-polymer, crystalline compound, and glassy. In solid state electrolytes, lithium ions travel along polymer chains and crystalline or amorphous framework. Disadvantages of the solid state electrolyte include low ionic conductivity (10^{-9}~10^{-3} $S{\cdot}cm^{-1}$) and high manufacturing cost. Another alternative to the organic electrolyte is the ionic liquid (IL) electrolyte which is largely made up of ions. Compared

Active material	**Average discharge potential (V vs. Li/Li^+)**	**Potential range (V vs Li/Li^+)**	**Theoretical capacity ($mAh \cdot g^{-1}$)**	**ref**
$LiCoPO_4$	~4.8	3.0−5.1	167	11
$LiNiPO_4$	~5.1	3.0−5.5	167	12
$LiNi_{0.5}Mn_{1.5}O_4$	~4.7	3.5−4.9	147	13
$LiCr_yMn_{2-y}O_4$ ($0.5 \leq y \leq 1$)	~4.7	3.4−5.4	151	14
$LiCo_yMn_{2-y}O_4$ ($0.5 \leq y \leq 1$)	~4.8	3.0−5.3	145	15
$LiFe_{0.5}Mn_{1.5}O_4$	~4.5	3.0−5.3	148	16
$x Li_2MnO_3 \cdot (1-x)LiMO_2$ ($0 < x < 1$, M = Ni, Co, Mn)	~3.5	2.0−4.8	314	17

Table 1.1: Selected positive electrode active materials that exhibit high average discharge potential.

to the organic electrolyte, the IL electrolyte has a high thermal stability, low flammability, and a wider stable potential window (1.5 V~ 6.0 V vs. Li/Li^+). Although the ionic conductivity of IL electrolytes are higher than the solid state type, it is still lower than the that of organic electrolytes, especially at low temperature. Other drawbacks of the IL electrolyte include low wettability as well as poor SEI formation ability on electrode surfaces. Such drawbacks may be mitigated by adding additives such as vinyl carbonate (VC) or organic solvents such as dimethyl carbonate (DMC) [21].

Research on Li-ion Battery Capacity Fading Mechanisms

All secondary batteries including the Li-ion type show a decreasing performance with usage and time. This permanent reduction in battery performance is often referred to as battery aging. Moreover, the capacity fade associated with the storage time is referred to as a calendar life and with the number of cycles is referred to as a cycle life. The calendar life test is often carried out in a fixed temperature and state-of-charge (SOC). The cycle life test is often repeated full charge-discharge cycles with a fixed current and temperature or based on actual device loading conditions. However, the results from the two methods can be quite different because the cell degradation is non-linear. The battery aging is usually quantified as capacity or power loss as a function of cycle number or storage period. The capacity fade may be more relevant in portable consumer electronics or pure electric vehicles (EVs), whereas the power fade may be more relevant in hybrid electric vehicles (HEVs) where the battery is in a continuous charge-sustaining mode. For Li-ion batteries, various aging mechanisms have been identified and they may be classified into two major categories – chemical and structural.

The chemical degradation mechanisms are any capacity loss due to irreversible chemical reaction. Examples include the electrolyte oxidation/reduction near the active material and

subsequent formation of the SEI layer [18], lithium plating [22], evolution of gaseous products [23], and dissolution of a transition metal element [24]. Often when a capacity fading occurs due to any chemical degradation mechanism, insoluble solid byproducts are formed and become a part of the SEI layer. Therefore, a chemical degradation mechanism may be inferred by analyzing the chemical constituents of the SEI layer. In analyzing the chemical constituents of the SEI layer, X-ray photoelectron spectroscopy (XPS) is frequently used. However, because a chemical reaction may involve a single or multi-electron transfer process in multiple steps, identifying the exact chemical reactions from the SEI layer components may not be straightforward. Another important physical characteristic of the SEI layer is its thickness because a lithium ion needs to diffuse through the layer before being intercalated into the active material. The SEI layer thickness may be estimated by an Ar-sputtering method combined with an XPS technique [25,26], an atomic force microscopy (AFM) technique [27,28], and an optical ellipsometry technique [29,30]. Besides the physical characteristics of the SEI layer, the layer may also be characterized in terms of its associated impedance. The associated impedance may be measured with an electrochemical impedance spectroscopy (EIS) method.

The second major type of degradation mechanism is the structural degradation mechanism and it is associated with any capacity loss due to irreversible structural changes of the active material. Many Li-ion active materials undergo volume expansion/contraction as well as phase transformation during lithium intercalation/deintercalation process. If the intercaltion-induced stress due to inhomogeneous volume change exceeds the material yield stress, the active material will fracture. For active materials with significant volume changes such as silicon anode fracturing is the major cause of capacity fading. When a fracture occurs a branch of an active material may be isolated from the percolated body and become permanently inactive. In

mitigating the intercalation-induced stress, a reduced particle size with a high aspect is favorable. An irreversible phase transformation of active materials may also be classified as a structural degradation mechanism. A $LiMn_2O_4$ cubic spinel phase may transform to a tetragonal phase and a Li-rich layered phase may transform to a spinel phase. Typically, a capacity is reduced when an irreversible phase transformation occurs.

Li-ion Battery Rate Capability

The role of Li-ion batteries in HEVs is to assist in supplying power in an operating region where the main internal combustion engine is inefficient or to capture energy during regen braking periods. Hence, for Li-ion batteries used in hybrid electric vehicles (HEVs), the rate capability or the power performance of the battery may be more relevant than the battery energy density. A gravimetric cell capacity is determined by the mass of the limiting electrode plus the total mass of inactive materials such as polymer binders, current collectors, and cell housing. On the other hand, a cell rate capability depends on transport, kinetic, and thermodynamic material properties of the electrode and the electrolyte phases. Because many material properties are a function of Li^+ concentration and temperature, the rate capability depends on the cell state-of-charge (SOC) and the ambient temperature as well. In addition, due to Li^+ diffusive transport properties, the rate capability also depends on the dimensional and structural aspects such as the electrode porosity and tortuosity, the active material particle size, and the thickness of the electrode and the electrolyte phases. When a cell degrades, not only the cell internal ohmic impedance rises, but also transport and kinetic material properties may deteriorate. For example, the effective electrochemical reaction kinetic properties may be reduced due to the undesired SEI formation or the effective Li^+ diffusive properties within active materials may be reduced due to irreversible phase transformations. Temperature also has a significant influence on the rate

capability. When the cell temperature rises to about 50 °C or higher, the degradation mechanisms tend to accelerate. When the cell temperature decreases, the OCP of the active materials tends to rise; however, the thermal activation loss associated with transport and kinetic material properties often significantly outweigh the OCP rise, leading to the reduced overall cell capability.

The cell open circuit potential (OCP) is determined by the thermodynamic properties of the positive and negative electrodes. During cycles, however, the actual cell potential profile will deviate from the cell OCP due to polarization, or losses. This polarization can be classified into three types – (i) activation, (ii) concentration, and (iii) ohmic. The activation polarization describes the loss associated with the charge transfer kinetics of an electrochemical reaction. The concentration polarization is the loss associated with the diffusive mass transport limitations. Lastly, the ohmic polarization represents the potential drop due to electronic and ionic resistivity in the electrodes and electrolyte, respectively. The potential loss will not only depend on material properties, which are dependent on SOC and temperature, but also on cell loading conditions because different types of potential losses occur on different timescales. For example, the potential drop due to ohmic loss will occur instantaneously, whereas the potential drop due to diffusive mass transport limitations will span over a longer period.

Li-ion Battery Models

Various types of Li-ion battery models are available in the literature for optimizing battery design parameters. Classes of Li-ion battery models include equivalent circuit models (ECM) [31,32], pseudo 2D models [33,34], single particle 3D models [35], multi-physics multi-dimensional models [36], and molecular/atomistic models [37,38]. Each class of model has a different predictive capabilities with different computational time. For example, a

molecular/atomistic model would be appropriate for studying an active material surface coating effect on the electrochemical reaction kinetics, whereas a simple equivalent circuit model may be suitable in an on-board battery management system where computational time is critical. In this study, the effect of grain boundaries on the battery performance is studied using a single particle 3D model. In addition, the sensitivity of transport and kinetic material properties on the cell electrochemical behavior is investigated using a thermal electrochemical pseudo 2D model.

SCOPE AND OUTLINE OF THE DISSERTATION

In Chapter 2, a 3D single particle containing grain boundaries is used in a Li-ion cell model to investigate the effect of grain boundaries on the overall Li+ diffusivity and intercalation-induced stress. A Voronoi grain distribution is employed in modeling grain boundaries. The grain boundary effect on Li^+ diffusivity is evaluated by computing an apparent diffusion coefficient from the particles containing different grain boundary densities. Many Li-ion active materials undergo volumetric strains during Li^+ intercalation/deintercalation process. However, the volumetric strain at the crystallographic level and at the aggregate particle level may be different due to crystallographic defects such as grain boundaries and geometrical constraints within particles. Hence, In Chapter 3, volumetric strains of $LiMn_2O_4$ particles are measured with *in-situ* atomic force microscopy (AFM) and compared against crystallographic strain measurements with an X-ray diffraction method. In addition, the intercalation-induced stress influence on Li^+ diffusivity is estimated numerically. In Chapter 4, the sensitivity of various transport and kinetic cell material properties on the cell electrochemical behavior is investigated using an electrochemical pseudo-2-dimensional model. Based on the numerical

sensitivity finding, material properties of a commercial cell are estimated and identified which properties are the rate-limiting factor on the cell performance.

BIBLIOGRAPHY

1. The U.S. Environmental Protection Agency official website, http://www.epa.gov/climatechange/ghgemissions/sources/transportation.html (accessed December, 26, 2013).

2. Lang, J. L.; Cheng, S. Y.; Wei, W.; Zhou, Y.; Wei, X.; Chen, D. S., A study on the trends of vehicular emissions in the beijing-tianjin-hebei (bth) region, china. *Atmos. Environ.* **2012,** *62*, 605-614.

3. The U.S. Energy Information Administration official website, http://www.eia.gove (accessed December 26, 2013)

4. The united states advanced battery consortium (USABC) goals for advanced batteries for evs, http://www.uscar.org/guest/article_view.php?articles_id=86 (accessed December 27, 2013).

5. Spotnitz, R.; Franklin, J., Abuse behavior of high-power, lithium-ion cells. *Journal of Power Sources* **2003,** *113* (1), 81-100.

6. Ramadass, P.; Haran, B.; White, R.; Popov, B. N., Capacity fade of sony 18650 cells cycled at elevated temperatures part i. Cycling performance. *Journal of Power Sources* **2002,** *112* (2), 606-613.

7. Amine, K.; Liu, J.; Belharouak, I., High-temperature storage and cycling of c-lifepo4/graphite li-ion cells. *Electrochem. Commun.* **2005,** *7* (7), 669-673.

8. Zhang, S. S.; Xu, K.; Jow, T. R., The low temperature performance of li-ion batteries. *Journal of Power Sources* **2003,** *115* (1), 137-140.

9. Padhi, A. K.; Nanjundaswamy, K. S.; Goodenough, J. B., Phospho-olivines as positive-electrode materials for rechargeable lithium batteries. *J. Electrochem. Soc.* **1997,** *144* (4), 1188-1194.

10. Yang, S. F.; Song, Y. N.; Zavalij, P. Y.; Whittingham, M. S., Reactivity, stability and electrochemical behavior of lithium iron phosphates. *Electrochem. Commun.* **2002,** *4* (3), 239-244.

11. Lloris, J. M.; Vicente, C. P.; Tirado, J. L., Improvement of the electrochemical performance of licopo(4)5vmaterial using a novel synthesis procedure. *Electrochem. Solid State Lett.* **2002,** *5* (10), A234-A237.

12. Zhou, F.; Cococcioni, M.; Kang, K.; Ceder, G., The li intercalation potential of limpo4 and limsio4 olivines with m = fe, mn, co, ni. *Electrochem. Commun.* **2004,** *6* (11), 1144-1148.

13. Xia, Y. Y.; Sakai, T.; Fujieda, T.; Wada, M.; Yoshinaga, H., A 4 v lithium-ion battery based on a 5 v linixmn2-xo4 cathode and a flake cu-sn microcomposite anode. *Electrochem. Solid State Lett.* **2001,** *4* (2), A9-A11.

14. Sigala, C.; Guyomard, D.; Verbaere, A.; Piffard, Y.; Tournoux, M., Positive electrode materials with high operating voltage for lithium batteries - licrymn2-yo4 (0-less-than-or-equal-to-y-less-than-or-equal-to-1). *Solid State Ionics* **1995,** *81* (3-4), 167-170.

15. Kawai, H.; Nagata, M.; Kageyama, H.; Tukamoto, H.; West, A. R., 5 v lithium cathodes based on spinel solid solutions li2co1+xmn3-xo8 :-1 <= x <= 1. *Electrochim. Acta* **1999,** *45* (1-2), 315-327.

16. Shigemura, H.; Tabuchi, M.; Kobayashi, H.; Sakaebe, H.; Hirano, A.; Kageyama, H., Structural and electrochemical properties of li(fe, co)(x)mn2-xo4 solid solution as 5 v positive electrode materials for li secondary batteries. *J. Mater. Chem.* **2002,** *12* (6), 1882-1891.

17. Lu, Z. H.; Dahn, J. R., Understanding the anomalous capacity of li/li nixli(1/3-2x/3)mn(2/3-x/3 o-2 cells using in situ x-ray diffraction and electrochemical studies. *J. Electrochem. Soc.* **2002,** *149* (7), A815-A822.

18. Peled, E., The electrochemical-behavior of alkali and alkaline-earth metals in non-aqueous battery systems - the solid electrolyte interphase model. *J. Electrochem. Soc.* **1979,** *126* (12), 2047-2051.

19. Verma, P.; Maire, P.; Novak, P., A review of the features and analyses of the solid electrolyte interphase in li-ion batteries. *Electrochim. Acta* **2010,** *55* (22), 6332-6341.

20. Park, M.; Zhang, X. C.; Chung, M. D.; Less, G. B.; Sastry, A. M., A review of conduction phenomena in li-ion batteries. *Journal of Power Sources* **2010,** *195* (24), 7904-7929.

21. Navarra, M. A., Ionic liquids as safe electrolyte components for li-metal and li-ion batteries. *MRS Bull.* **2013,** *38* (7), 548-553.

22. Neudecker, B. J.; Dudney, N. J.; Bates, J. B., "Lithium-free" thin-film battery with in situ plated li anode. *J. Electrochem. Soc.* **2000,** *147* (2), 517-523.

23. Kong, W. H.; Li, H.; Huang, X. J.; Chen, L. Q., Gas evolution behaviors for several cathode materials in lithium-ion batteries. *Journal of Power Sources* **2005,** *142* (1-2), 285-291.

24. Amatucci, G. G.; Schmutz, C. N.; Blyr, A.; Sigala, C.; Gozdz, A. S.; Larcher, D.; Tarascon, J. M., Materials' effects on the elevated and room temperature performance of c/limn2o4 li-ion batteries. *Journal of Power Sources* **1997,** *69* (1-2), 11-25.

25. Bar-Tow, D.; Peled, E.; Burstein, L., A study of highly oriented pyrolytic graphite as a model for the graphite anode in li-ion batteries. *J. Electrochem. Soc.* **1999,** *146* (3), 824-832.

26. Ruffo, R.; Hong, S. S.; Chan, C. K.; Huggins, R. A.; Cui, Y., Impedance analysis of silicon nanowire lithium ion battery anodes. *Journal of Physical Chemistry C* **2009,** *113* (26), 11390-11398.

27. Leroy, S.; Blanchard, F.; Dedryvere, R.; Martinez, H.; Carre, B.; Lemordant, D.; Gonbeau, D., Surface film formation on a graphite electrode in li-ion batteries: Afm and xps study. *Surf. Interface Anal.* **2005,** *37* (10), 773-781.

28. Yazami, R., Surface chemistry and lithium storage capability of the graphite-lithium electrode. *Electrochim. Acta* **1999,** *45* (1-2), 87-97.

29. Lei, J. L.; Li, L. J.; Kostecki, R.; Muller, R.; McLarnon, F., Characterization of sei layers on limn2o4 cathodes with in situ spectroscopic ellipsometry. *J. Electrochem. Soc.* **2005,** *152* (4), A774-A777.

30. McArthur, M. A.; Trussler, S.; Dahn, J. R., In situ investigations of sei layer growth on electrode materials for lithium-ion batteries using spectroscopic ellipsometry. *J. Electrochem. Soc.* **2012,** *159* (3), A198-A207.

31. Peled, E.; Golodnitsky, D.; Ardel, G.; Eshkenazy, V., The sei model - application to lithium polymer electrolyte batteries. *Electrochim. Acta* **1995,** *40* (13-14), 2197-2204.

32. Liaw, B. Y.; Jungst, R. G.; Nagasubramanian, G.; Case, H. L.; Doughty, D. H., Modeling capacity fade in lithium-ion cells. *Journal of Power Sources* **2005,** *140* (1), 157-161.

33. Doyle, M.; Fuller, T. F.; Newman, J., Modeling of galvanostatic charge and discharge of the lithium polymer insertion cell. *J. Electrochem. Soc.* **1993,** *140* (6), 1526-1533.

34. Doyle, M.; Newman, J.; Gozdz, A. S.; Schmutz, C. N.; Tarascon, J. M., Comparison of modeling predictions with experimental data from plastic lithium ion cells. *J. Electrochem. Soc.* **1996,** *143* (6), 1890-1903.

35. Zhang, X.; Shyy, W.; Sastry, A. M., Numerical simulation of intercalation-induced stress in li-ion battery electrode particles. *J. Electrochem. Soc.* **2007,** *154* (10), A910-A916.

36. Stephenson, D. E.; Hartman, E. M.; Harb, J. N.; Wheeler, D. R., Modeling of particle-particle interactions in porous cathodes for lithium-ion batteries. *J. Electrochem. Soc.* **2007,** *154* (12), A1146-A1155.

37. Van der Ven, A.; Aydinol, M. K.; Ceder, G.; Kresse, G.; Hafner, J., First-principles investigation of phase stability in li(x)coo(2). *Phys. Rev. B* **1998,** *58* (6), 2975-2987.

38. Van der Ven, A.; Marianetti, C.; Morgan, D.; Ceder, G., Phase transformations and volume changes in spinel lixmn2o4. *Solid State Ionics* **2000,** *135* (1-4), 21-32.

CHAPTER II

NUMERICAL STUDY OF GRAIN BOUNDARY EFFECT ON LI^+ EFFECTIVE DIFFUSIVITY AND INTERCALATION-INDUCED STRESSES IN LI-ION BATTERY ACTIVE MATERIALS

INTRODUCTION

An ideal secondary battery for hybrid electric vehicles would feature low cost, high gravimetric energy and power densities, an absence of thermal runaway for safety, and minimal capacity degradation. High gravimetric power density in particular allows for increased vehicle acceleration and a reduced battery charging time. The power performance of a lithium ion (Li-ion) secondary battery is primarily determined by Li-ion diffusivity in the host electrode materials. In the host electrode material, Li-ion diffusivity is influenced by intercalation-induced stress fields [31, 35-37], phase boundary mobilities [38-40], and crystallographic defects [41-42]. Both thin-film and primary particle Li-ion active materials are polycrystalline materials, which are dense aggregates of single crystals joined by a network of interfacial crystallographic defects known as grain boundaries. It is widely recognized that the grain boundary network in these materials influence their properties, including transport properties. The more loosely packed structures of the grain boundaries result in a higher diffusivity compared to that inside the grain. For polycrystalline materials, the measured activation energy for self-diffusion at the grain boundary is only a fraction of that in the lattice, resulting in a diffusivity that is 3-16 orders of magnitude higher in the grain boundary than in the lattice [43-45]. These experiments have

shown that as the average grain size is refined to nanoscale, the grain boundary increasingly dominates the transport properties.

To investigate the grain boundary effect on overall diffusivity, Fisher first modeled a single fast diffusing grain boundary embedded in a semi-infinite bulk of much lower diffusivity [46]. The model and its variants are today widely used in understanding grain boundary diffusion. For simplified polycrystalline geometries, where grain boundaries are lamaller [47] or square matrices [48-49], expressions for an effective diffusion coefficient have been formulated using rules-of-mixture or volumetric averages of the constituent diffusion coefficients. Although the rules-of-mixture method has also been used to study more complex structural effects such as grain size distributions [50] or triple junction densities [51], numerical methods such as molecular dynamics or the Monte Carlo method are more common in studying the effective diffusivity in the presence of grain boundaries. Moreover, effective diffusivities have been classified into different regimes of diffusion kinetics [52-53]. For example, based on the ordering of bulk diffusion length, grain boundary diffusion length, grain boundary thickness, and the average grain size, the overall diffusion kinetics may be determined by grain boundary diffusivity or a mixture of both bulk and grain boundary diffusivities.

Based on various experimental studies, the role of grain boundaries in Li-ion active materials has been postulated. For example, in a $LiCoO_2$ thin-film where grains are oriented in a preferred (0 0 3) direction that lithium ions have difficulty diffusing through, grain boundaries may facilitate lithium ions to diffuse into the bulk [54]. A study with *in situ* scanning probe microscopy (SPM) also showed that the formation of (LiF) particles at the grain boundaries lead to reduced lithium ion flux into the active material, as reflected on cyclic voltammograms [55]. Conversely, other studies suggest that grain orientations have a more significant influence on the

overall Li-ion diffusivity than the grain boundary density, especially for materials with two dimensional lattice diffusion mechanisms such as $LiCoO_2$ [56] and V_2O_5 [57]. In one study, using the electrochemical strain microscopy (ESM) method, relatively higher Li^+ diffusivity was observed in certain grain facets and grain boundary-like features in a $LiCoO_2$ thin-film [58]. Another study showed that Sn-containing grain boundaries may be used as intercalation sites among inactive $SnMn_3C$ grains [59]; it demonstrates that grain boundaries may be utilized in controlling large volume expansion/contraction in metal anodes, which lead to energy capacity degradation. Indeed, many Li-ion active materials, including metal-alloys [60-61], $LiCoO_2$ [62], $LiMn_2O_4$ [63], and $LiFePO_4$ [64], undergo reversible lattice expansion during charging/discharging. Hence, internal strains/stresses may develop, leading to a gradual loss of energy capacity by dislocations, microcracks [62, 64], or isolation of the active material from the current collector [65]. Several models have been developed to estimate the intercalation-induced stress in Li-ion active materials during charging/discharging [31, 35-36]. These models show that intercalation-induced stress is roughly proportional to the concentration gradient developed in the particle. Because a grain boundary network can modify the concentration distribution within active materials, it would also affect intercalation-induced stress and its associated energy capacity degradation.

Although various postulations have been made in regards to the role of grain boundaries in Li-ion active materials, the effect of grain boundaries in Li-ion batteries has never been studied systematically. This is possibly due to difficulty in controlling the grain boundary density without affecting material phase and grain size/orientation distributions. Furthermore, in composite electrodes, the porosity can complicate the analysis. To study grain boundary effect on Li-ion battery performance, we model ellipsoidal cathode particles embedded with grain

boundaries using a finite element method approach. By integrating a Fisher-type grain boundary model with a Li-ion stress-diffusion model, the role of grain boundary on overall Li^+ diffusivity, intercalation-induced stress, and energy capacity utilization is investigated. We have the following objectives:

1. To develop an electrochemical-mechanical model that considers grain boundaries in Li-ion active materials
2. To investigate the grain boundary effect on Li-ion battery performance including lithium ion diffusivity, intercalation-induced stress, and capacity utilization

METHODS

To investigate grain boundary effect on overall lithium diffusivity as well as intercalation-induced stress, a Fickian diffusion equation coupled with a Hookean stress-strain constitutive equation was solved. Diffusion-stress coupling was achieved by including the elastic energy of the solute in the chemical potential [31, 66-67].

Diffusion-Stress Model in the Grain Domain

Lithium ion diffusion is driven by the chemical potential gradient. For a given lithium ion concentration and hydrostatic stress gradients, the diffusion flux for a dilute or ideal system [3] is given by

$$\mathbf{J}_g = -D_g\left(\nabla c_g - \frac{\Omega c_g}{RT}\nabla\sigma_k\right) \tag{1}$$

where subscript g indicates the grain or bulk domain, D_g is the diffusion coefficient, c_g is the concentration, Ω is partial molar volume, R is the universal gas constant, T is temperature, and σ_h is hydrostatic stress, defined as $\sigma_h = (\sigma_{11} + \sigma_{22} + \sigma_{33})/3$ (where σ_{ij} is the element in the stress

tensor). Substituting Eq. 1 into the mass conservation equation, the following species transport equation in the grain domain was obtained

$$\frac{\partial c_g}{\partial t} + \nabla \cdot \left[-D_g \left(\nabla c_g - \frac{\Omega c_g}{RT} \nabla \sigma_k \right) \right] = 0 . \quad (2)$$

In the cubic $Li_xMn_2O_4$ ($0 < x < 1$) phase, the lattice parameter of the host material was assumed to change linearly with the amount of ions inserted [68]; this results in intercalation-induced stresses. Therefore, the stress can be calculated using a thermal-analogy stress model [31, 69]. The stress–strain relation with the effect of intercalation is given by

$$\varepsilon_{ij} = \frac{1}{E}\left[(1+\nu)\sigma_{ij} - \nu\sigma_{kk}\delta_{ij} \right] + \frac{\Omega \Delta c_g}{3}\delta_{ij}, \quad (3)$$

where Δc_g is the concentration change of the diffusion species from the original stress-free value. Equations 2 and 3 are coupled through concentration, c_g, and stress, σ_h.

Li^+ transport in the grain boundary domain

Fisher grain boundary modeling [46, 70] was adopted here. One assumption made in the model is that the concentration change across the grain boundary is negligible. Hence, the grain boundary domain can be modeled as a 2D surface embedded in 3D grain domains. In a finite element method, this assumption significantly reduces the computational cost because a high concentration of meshing near the very thin grain boundary can be avoided. Assumptions made in the grain boundary modeling are as follows:

i. Fick's laws are obeyed in the grain boundary domain
ii. Unlike in the grain domain, intercalation-induced stress is neglected in the grain boundary domain due to its amorphous nature and negligible associated volume expansion/contraction

iii. The grain boundary diffusion coefficient D_{gb} is isotropic and independent of concentration and time

iv. D_{gb} is greater than D_g

v. Concentrations and normal fluxes at the grain and grain boundary interface are continuous (i.e., no segregation effect)

vi. Concentration across the grain boundary is symmetrical on either side of the middle plane

An expression of species flux in the grain boundary domain is as follows

$$\mathbf{J}_{gb} = -D_{gb}\nabla c_{gb}\left(n,t_1,t_2,t\right). \tag{4}$$

The subscript *gb* denotes the grain boundary and *t* represents time. Here, the concentration gradient is decomposed into normal, *n*, and two tangential components, t_1 and t_2, relative to the middle plane of the grain boundary; hence, the gradient is taken as $\nabla = \left(\partial/\partial n, \partial/\partial t_1, \partial/\partial t_2\right)$. Conservation of mass in the grain boundary domain is expressed as

$$\frac{\partial c_{gb}}{\partial t} + \nabla \cdot \mathbf{J}_{gb} = 0. \tag{5}$$

A simplified schematic diagram of the grain boundary between two grains is shown in Fig. 2.1, where the thickness of the grain boundary is δ. The model assumes that the concentration and normal fluxes at the grain/grain boundary interface are continuous, as described in Equations 6(a) and 6(b).

$$c_g\left(n,t_1,t_2,t\right) = c_{gb}\left(n,t_1,t_2,t\right) \qquad n = \pm\delta/2 \tag{6a}$$

$$\mathbf{n}\cdot\mathbf{J}_g\left(n,t_1,t_2,t\right) = \mathbf{n}\cdot\mathbf{J}_{gb}\left(n,t_1,t_2,t\right) \quad n = \pm\delta/2 \tag{6b}$$

A Taylor series expansion of the grain boundary concentration with respect to $n = 0$ is written as

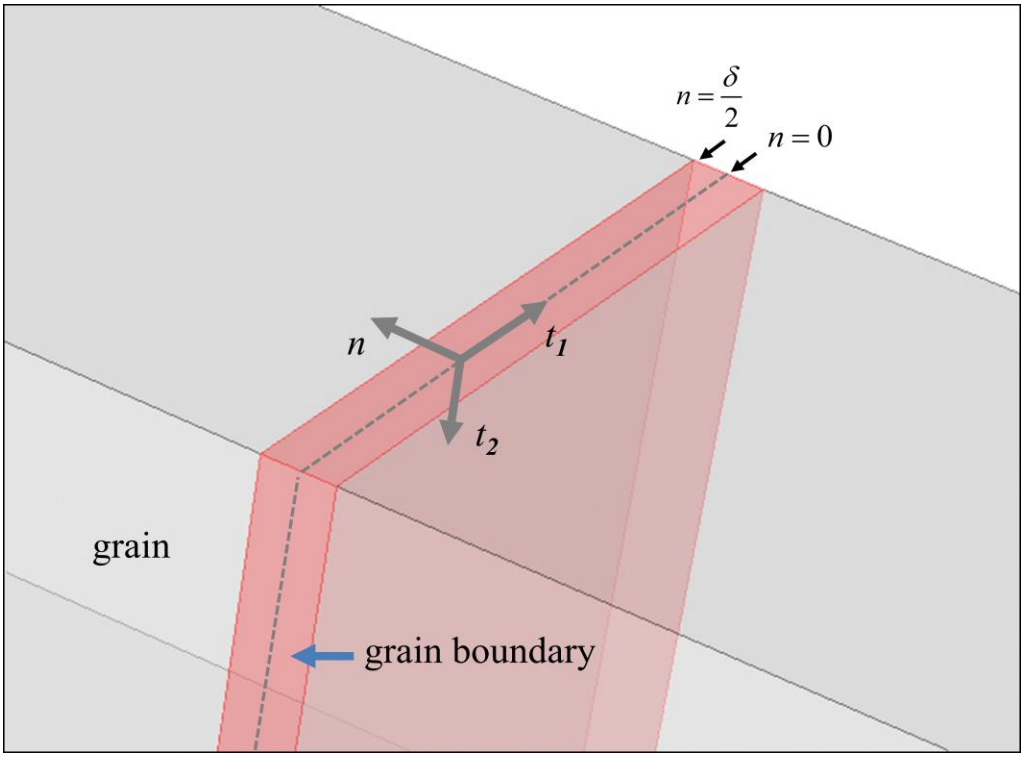

Figure 2.1: A schematic diagram of a grain boundary embedded between two semi-infinite grains.

$$c_{gb}\left(n,t_1,t_2,t\right)=c_{gb}\left(n,t_1,t_2,t\right)\Big|_{n=0}+n\frac{\partial c_{gb}\left(n,t_1,t_2,t\right)}{\partial n}\Big|_{n=0}+\frac{n^2}{2}\frac{\partial^2 c_{gb}\left(n,t_1,t_2,t\right)}{\partial n^2}\Big|_{n=0}+\ldots+\frac{n^m}{m!}\frac{\partial^m c_{gb}\left(n,t_1,t_2,t\right)}{\partial n^m}\Big|_{n=0}$$

where m = 1, 2, 3,… (7)

Here it is assumed that the concentration across the grain boundary thickness is an even function about n = 0 due to symmetry. Because the first derivative of an even function evaluated at the point of symmetry is zero, all the odd functions in Eq. 7 are neglected. Taking a derivative with respect to n and neglecting third order and higher terms in Eq. 7, the following expression can be obtained.

$$\frac{\partial c_{gb}\left(n,t_1,t_2,t\right)}{\partial n}=n\frac{\partial^2 c_{gb}\left(n,t_1,t_2,t\right)}{\partial n^2}\Big|_{n=0}\quad . \tag{8}$$

Eq. 8 evaluated at the grain/grain boundary interface $n = \pm\delta/2$ is:

$$\frac{\partial c_{gb}\left(n,t_1,t_2,t\right)}{\partial n}\Big|_{n=\pm\delta/2}=\pm\frac{\delta}{2}\frac{\partial^2 c_{gb}\left(n,t_1,t_2,t\right)}{\partial n^2}\Big|_{n=0}\quad . \tag{9}$$

Combining Eq. 9 with Eqs. 4, 5, and 6(b), then solving in terms of $\mathbf{J}_g$, yields:

$$\mathbf{n}\cdot\mathbf{J}_g\Big|_{n=+\delta/2}=-\frac{\delta}{2}\frac{\partial c_{gb}(t_1,t_2,t)}{\partial t}+\frac{\delta}{2}D_{gb}\nabla_t^2 c_{gb}(t_1,t_2,t)\ \text{, and} \tag{10a}$$

$$\mathbf{n}\cdot\mathbf{J}_g\Big|_{n=-\delta/2}=\frac{\delta}{2}\frac{\partial c_{gb}(t_1,t_2,t)}{\partial t}-\frac{\delta}{2}D_{gb}\nabla_t^2 c_{gb}(t_1,t_2,t)\ . \tag{10b}$$

The right-hand side of Eq. 10 are all quantities on the middle plane of the grain boundary (n = 0) and $\nabla_t=\left(\partial/\partial t_1,\partial/\partial t_2\right)$. Thus the grain boundary becomes a 2D object. Although Fig. 2.1 shows a grain boundary with a thickness δ, in the actual model, grain boundaries are modeled as 2D surfaces between two grains without geometric thickness. Equations 10(a) and 10(b) may be considered as a boundary condition for $\mathbf{J}_g$ at the grain/grain boundary interface. Prior to

implementing the boundary condition, Equations 10(a) and 10(b) are converted to a boundary weak form as follows:

$$\mathbf{n}\cdot\mathbf{J}_g\Big|_{n=+\delta/2} = -\int_S w\frac{\delta}{2}\frac{\partial c_{gb}}{\partial t}dS + \int_S wD_{gb}\frac{\delta}{2}\nabla_t^2 c_{gb}dS \text{ , and} \tag{11a}$$

$$\mathbf{n}\cdot\mathbf{J}_g\Big|_{n=-\delta/2} = \int_S w\frac{\delta}{2}\frac{\partial c_{gb}}{\partial t}dS - \int_S wD_{gb}\frac{\delta}{2}\nabla_t^2 c_{gb}dS \,. \tag{11b}$$

In Eq. 11, S represents the grain boundary interface domain, and w is the weighting function. Noting that

$$wD_{gb}\nabla_t{}^2 c_{gb} = -D_{gb}\nabla_t w\cdot\nabla_t c_{gb} + \nabla_t\cdot\left(wD_{gb}\nabla_t c_{gb}\right), \tag{12}$$

Eq. 11(a) and 11(b) can be re-written as

$$\mathbf{n}\cdot\mathbf{J}_g\Big|_{n=+\delta/2} = -\frac{\delta}{2}\int_S w\frac{\partial c_{gb}}{\partial t}dS - \frac{\delta}{2}\int_S D_{gb}\nabla_t w\cdot\nabla_t c_{gb}dS + \frac{\delta}{2}\int_S \nabla_t\cdot(wD_{gb}\nabla_t c_{gb})dS \text{ , and} \tag{13a}$$

$$\mathbf{n}\cdot\mathbf{J}_g\Big|_{n=-\delta/2} = \frac{\delta}{2}\int_S w\frac{\partial c_{gb}}{\partial t}dS + \frac{\delta}{2}\int_S D_{gb}\nabla_t w\cdot\nabla_t c_{gb}dS - \frac{\delta}{2}\int_S \nabla_t\cdot(wD_{gb}\nabla_t c_{gb})dS \,. \tag{13b}$$

By the Divergence theorem, the last terms in Eq. 13(a) and 13(b) can be re-written as

$$\int_S \nabla_t\cdot(wD_{gb}\nabla_t c_{gb})dS = \int_l wD_{gb}\nabla_t c_{gb}\cdot\mathbf{m}dl \,, \tag{14}$$

where **m** is the normal direction of the edge curve of the grain boundary surface. Assuming that the net flux along the edges of the grain boundary is zero, the above term was neglected. Hence,the final boundary weak form of the flux at the grain/grain boundary interface is:

$$\mathbf{n}\cdot\mathbf{J}_g\Big|_{n=+\delta/2} = -\frac{\delta}{2}\int_S w\frac{\partial c_{gb}}{\partial t}dS - \frac{\delta}{2}\int_S D_{gb}\nabla_t w\cdot\nabla_t c_{gb}dS \text{ , and} \tag{15a}$$

$$\mathbf{n}\cdot\mathbf{J}_g\Big|_{n=-\delta/2} = \frac{\delta}{2}\int_S w\frac{\partial c_{gb}}{\partial t}dS + \frac{\delta}{2}\int_S D_{gb}\nabla_t w\cdot\nabla_t c_{gb}dS \,. \tag{15b}$$

Using COMSOL Multiphysics, Equations 2 and 15 for lithium transport in the grain and grain boundary domains were solved using a general PDE and a weak boundary form module, respectively. Equation 3 for intercalation-induced stress was solved using a general PDE module.

Electrochemical Kinetics under Galvanostatic and Potentiodynamic Controls

In this study, a cell consisting of a micron-scale single-particle positive electrode with lithium metal negative electrode was modeled. The positive electrode was isotropic cubic-phase $Li_xMn_2O_4$ ($0 \le x \le 1$) prolate spheroids containing grain boundaries. During charging, species are oxidized at the positive electrode, and lithium ions are extracted. During discharging, species are reduced at the positive electrode, and lithium ions are inserted. The reactions for the $LiMn_2O_4$ positive electrode are

$$LiMn_2O_4 \Leftrightarrow Li_{1-x}Mn_2O_4 + xLi^+ + xe^-. \tag{16}$$

Under a galvanostatic control, a constant diffusion flux **J** was applied at the particle surface,

$$\mathbf{n} \cdot \mathbf{J} = i_n / F, \tag{17}$$

where F is Faraday's constant, and the discharge/charge current density i_n was determined based on the C-rate. Under a potentiodynamic control, the diffusion flux boundary condition at the particle surface was determined by the Butler-Volmer equation [71],

$$\mathbf{n} \cdot \mathbf{J} = \frac{i_n}{F} = \frac{i_0}{F}\left\{\exp\left[\frac{(1-\beta)F}{RT}\eta\right] - \exp\left[-\frac{\beta F}{RT}\eta\right]\right\}. \tag{18}$$

Here i_0 is the exchange current density, η is surface overpotential, and β is a symmetry factor which represents the fraction of the applied potential that promotes the cathodic reaction. The exchange current density, i_0, is given by

$$i_0 = Fkc_l^{1-\beta}\left(c_{\max} - c_s\right)^{1-\beta} c_s^{\beta}, \tag{19}$$

where c_l is the concentration of lithium ion in the electrolyte, c_s is the Li^+ concentration at the particle surface, $(c_{max} - c_s)$ is the concentration of available vacant sites on the surface ready for lithium intercalation (or equivalently, the difference between stoichiometric maximum concentration and current concentration on the surface of the electrode), and k is a reaction rate constant [72]. The surface overpotential, η, is the difference between the applied potential at the solid phase surface, V, and the equilibrium open circuit potential, U:

$$\eta = V - U. \tag{20}$$

As for the applied potential, V, a linear ramp potential with a sweep rate of 1.0 mV/s was used. An experimental fit of the open circuit potential (OCP) [30] s a function of state-of-charge (SOC) x in $Li_xMn_2O_4$ was used in the simulation. The $LiMn_2O_4$ spinel material properties and simulation parameters are listed in Table 2.1. In all simulations, the lattice diffusion coefficient was assumed to be isotropic and constant irrespective of the SOC.

Generation of Particles with Grain Boundaries

Polycrystalline primary particles in composite electrodes are agglomerated using polymeric binders [e.g., polyvinylidene fluoride (PVDF)] and carbon-based conductive additives (e.g., carbon black, graphite) to form secondary particles. Reported secondary particle sizes range from 6 to 60 μm [73-75]. Primary particle sizes vary with synthesis techniques and range from 0.3 to 4 μm [73, 75-76]. Primary particles as well as thin-film electrodes consist of crystalline grains, and their sizes also depend on synthesis methods. An annealing step in the synthesis process is often performed to yield a desired phase, but it may also be used to control grain sizes. Typical grain sizes in primary particles and thin-film electrodes are shown in Table 2.2. Grain sizes range from 25 nm to > 1 μm in primary particles [76-79] and from 10 to 300 nm

Symbol and unit	Name	Value
E (GPa)	Young's modulus	100
ν	Poisson's ratio	0.3
D_g (m^2/s)	bulk or lattice diffusion coefficient	7.08×10^{-15} [1]
Ω (m^3/mol)	partial molar volume	3.497×10^{-6}
c_{max} (mol/m^3)	$LiMn_2O_4$ stoichiometric maximum concentration	2.29×10^4
V (V)	applied ramp potential	3.5-4.3 V with 1 mV/s sweep rate
U (V)	open circuit potential	curve fit [51]
c_l (mol/m^3)	electrolyte Li^+ salt concentration	1,000
β (-)	symmetry factor	0.5
k ($m^{5/2}\,s^{-1}\,mol^{-1/2}$)	reaction rate constant	1.9×10^{-9} [50]
F (C/mol)	Faraday's constant	96,487
T (K)	temperature	300
R ($J\,mol^{-1}\,K^{-1}$)	universal gas constant	8.314

Table 2.1: $LiMn_2O_4$ material property values used in the simulation.

Active material	Configuration	Synthesis method	Primary particle size	Grain size	Ref.
$LiMn_2O_4$	Particles	Spray pyrolysis	~1.1 μm	25 nm	45
$LiMn_2O_4$	Particles	Calcination	~3 μm	< 100 nm	44
$Li[Ni_{1/3}Co_{1/3}Mn_{1/3}]O_2$	Particles	Spray pyrolysis	~500 nm	10-50 nm	46
$LiCoO_2$	Particles	Unknown	> 10 μm	~0.5-5 μm	47
Active material	**Configuration**	**Synthesis method**		**Grain size**	**Ref.**
$LiMn_2O_4$	thin film	PLD		200-300 nm	48
$LiCoO_2$	thin film	rf sputtering		~10-100 nm	49
$LiFePO_4$	thin film	PLD		~200 nm	50
$LiNi_{0.5}Mn_{0.5}O_2$	thin film	PLD		100-200 nm	51

Table 2.2: . Representative grain sizes in Li-ion particles and thin-films.

in thin-film electrodes [80-83]. As for the grain boundary thickness, a thickness of 4-25 nm has been observed for metal oxides including Al_2O_3 [84], $MgAl_2O_4$ spinel [85], and Mg_2GeO_4 spinel [86], under high resolution transmission electron microscopy (HRTEM). Grain boundary diffusivity is typically several orders of magnitude greater than in the lattice [43-45]. The grain boundary diffusivities for transition metal oxides such as Cr_2O_3 [87], Fe_3O_4 [88], and ZnO [89] typically range 3 to 7 orders of magnitude greater than the lattice diffusion. For the $LiMn_2O_4$ spinel, a grain boundary diffusion coefficient measured by secondary ion mass spectroscopy (SIMS) was approximately 3 to 4 orders greater than in the lattice [90]. In representing grain size distributions in polycrystalline materials, various distributions such as a monodispersed Tetrakaidecahedra distribution [50], a spread Johnson-Mehl distribution [50, 91], and a nearly log-normal Voronoi distribution [50, 91] have been used. In this study, a Voronoi distribution that consists of convex polyhedron grains was used. To generate Voronoi polycrystalline particles, the Multi Parametric Matlab Toolbox [92] was used. Each Voronoi structure was generated by specifying a number of grains. The particles containing grain boundary structures were then imported to COMSOL Multiphysics to run simulations. A prolate ellipsoid particle shape was used in all simulations. Assuming symmetry about *x*, *y*, and *z*, only one-eighth of the particle was used in the simulation.

Potentiodynamic control simulation input and output parameters

In the potentiodynamic control simulation, intercalation-induced stress and lithium ion diffusivity were investigated as a function of grain boundary network structure, grain boundary Li^+ diffusivity, and grain boundary thickness. A total of 31 prolate ellipsoidal particles with identical dimensions were used in the simulation. The 31 particles consisted of 1 particle without grain boundary and 30 particles with a unique grain boundary network structure. To control grain

Potentiodynamic control	**Values**
D_{gb}/D_g	10^3 and 10^4
Ellipsoidal particle geometry dimensions (*a* x *b* x *c*, μm)	1.2 x 1.2 x 2.0
Number of crystallites/grains	3-15
Grain boundary thickness, δ (nm)	0, 2, 4, 8, and 16
Galvanostatic control	**Values**
D_{gb}/D_g	10^3
Ellipsoidal particle geometry dimensions (*a* x *b* x *c*, μm)	Set 1: 1.2 x 1.2 x 2.0
	Set 2: 3.0 x 3.0 x 5.0
Number of crystallites/grains	3-15
Grain boundary thickness, δ (nm)	0 and 5

Table 2.3: Simulation design variables and their levels.

boundary Li^+ diffusivity, the ratio of grain boundary-to-bulk diffusion coefficient, D_{gb}/D_g, varied between 10^3 and 10^4, while the bulk diffusion coefficient, D_g, remained fixed. Finally, grain goundary thickness, δ, varied from 2 nm to 16 nm. Input variables and their levels used in the potentiodynamic control simulation are summarized in Table 2.3. In quantifying the grain boundary effect on intercalation-induced stress, the maximum principal stress was evaluated. To quantify relative changes in the overall diffusivity, rather than attempting to estimate a true effective diffusion coefficient, an apparent diffusion coefficient was computed based on the peak current from the potentiodynamic control simulation. Assuming that the intercalation/de-intercalation process is fully reversible, an apparent diffusion coefficient was computed based on the cyclic voltammetry (CV) diffusion equation [93-94], as shown in Eq. 21; the equation is valid when T = 300 K.

$$D_{Li} = \left(\frac{i_p / v^{1/2}}{(2.68 \times 10^5) n^{3/2} a c_O^0} \right)^2 . \tag{21}$$

In Eq. 21, i_p is the peak current, ν is the linear potential sweep rate, n is the number of moles of electrons transferred in the reaction, a is the electrode surface area, and c_o^0 is the initial lithium ion concentration in the fully lithiated system, which is 2.29 mol/m^3 for $LiMn_2O_4$.

Galvanostatic Control Simulation Input and Output Parameters

To test the particle size and the grain boundary effects on the capacity utilization, two sets of particles with different sizes were tested. The particle dimensions were identical within each set. The first set of particles consisted of 1 particle without grain boundary and 10 particles with unique Voronoi grain boundary network structures. The second set of particles consisted of the same 11 particles in the first set but the dimension was scaled up by a factor of 2.5 in all *x*-, *y*-, and *z*-directions. The grain boundary structures within the particles scaled accordingly. A fixed grain boundary thickness of δ = 5 nm and a grain boundary-to-lattice diffusion coefficient

ratio, D_{gb}/D_g = 10^3 were used in both sets. With various C-rates, each particle was galvanostatically discharged from 4.3 V to 3.5 V, or equivalently until the lithium ion concentration at a particle surface reached c_{max}. Input variables and their levels used in the galvanostatic control simulation are summarized in Table 2.3. The output discharge capacity utilization, denoted as Γ, was calculated by dividing the amount of lithium inserted at the particle surface over the maximum amount of lithium ions a particle can contain, or

$$\Gamma = \frac{1}{V_p \cdot c_{max}} \cdot \int_0^{t_f} \left(\int_S \frac{i_n}{F} dS \right) dt . \quad (22)$$

Here V_p represents particle volume, t_f is time when the lithium ion concentration at the particle surface reached 3.5 V or c_{max}, and S is the particle surface.

RESULTS AND DISCUSSION

Generated grain boundary network structures – The average grain sizes and associated standard deviations *vs*. grain boundary surface areas for the polycrystalline particles generated for the simulation are shown in Fig. 2.2. Figures 2.2a and 2.2b correspond to the particles used in the potentiodynamic control simulation and the galvanostatic control simulation, respectively. In Fig. 2.2, the particles have the same size but different number of grains. Thus for those particles with the same number of grains, their average grain sizes are the same. Moreover, because the specified number of grains was a multiple of three, the grain boundary surface areas are not evenly populated, as seen in Fig. 2.2a. In the galvanostatic control simulation, two sets of particles were used. In Fig. 2.2b, the bottom abscissa and the left ordinate correspond to the first set of particles, and the top abscissa and the right ordinate correspond to the second set of particles. Because the second set of particles was created by scaling up particles in the first set by a factor of 2.5 in *x*-, *y*-, and *z*-direction, the grain boundary network structures between the two

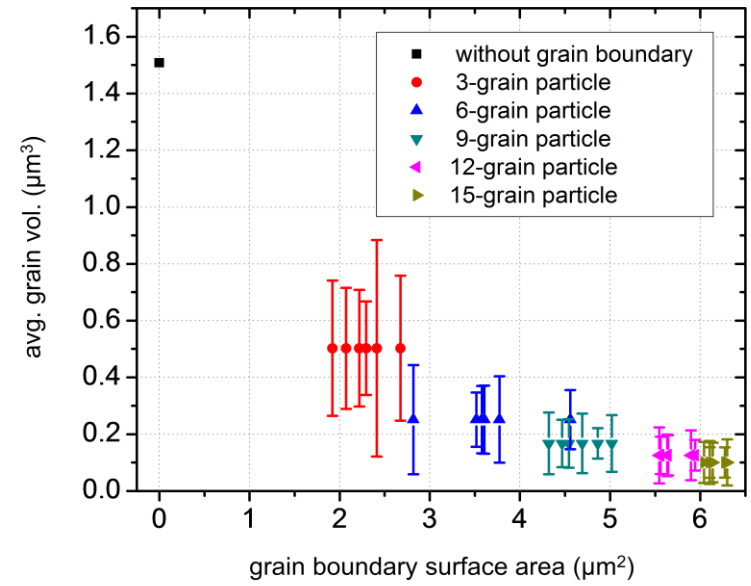

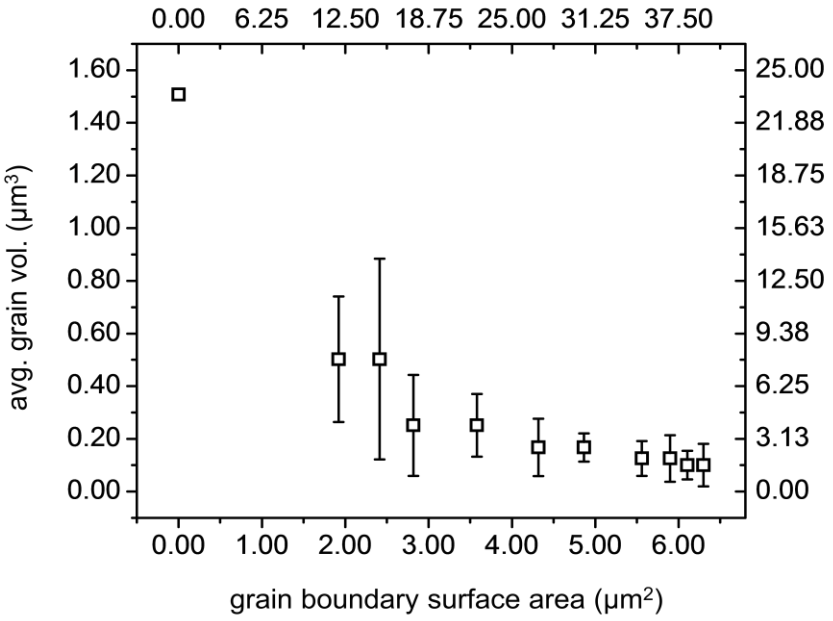

Figure 2.2: A summary of the average grain size and the grain boundary surface area for polycrystalline particles generated for: (above) the potentiodynamic control simulation and (below) the galvanostatic control simulation.

sets were conserved. After scaling, the surface area and the volume of each grain increased by a factor of 2.5^2 and 2.5^3, respectively. However, the grain boundary surface area-to-particle volume ratio, s_{gb}/v_g, was reduced by a factor of 2.5 after the scaling. The grain sizes in the generated polycrystalline particles are comparable to those grain sizes estimated from cross-sectioned images of $LiCoO^2$ composite electrodes [79].

The Grain Boundary Effect on Intercalation-Induced Stress

Particles were first charged and then discharged with a potential sweep rate of 1.0 mV/s in the potential range between 3.5 V and 4.3 V. Figure 2.3 shows the time history of reaction flux at the particle surface for a particle without grain boundary. During charging the flux is negative, as lithium ions are extracted; during discharging the flux is positive, as lithium ions are inserted. Figure 2.3 also shows two flux peaks during each half cycle, similar to results from simulations [72] and experiments [95]. According to the Bulter-Volmer electrochemical kinetics shown in Eq. 18, the reaction flux is a function of surface overpotential η and exchange current density i_0. The exchange current density, i_0, depends on the type of electrolyte, temperature, and nature of the electrode surface [71]. A reaction with a large value of i_0 is often described as fast. Also in Eq. 18, the current density varies linearly with η for small values of η, and exponentially with η for large values of η. If the surface overpotential is plotted as a function of time, it would peak twice during each half cycle because the applied potential increases linearly while $LiMn_2O_4$ OCP contains two plateaus. Hence, the reaction flux peaks shown in Fig. 2.3 are largely determined by the thermodynamic property of $LiMn_2O_4$. In addition, the exchange current density may shift the time location of the peak slightly. During charging, lithium ions are extracted from the particle surface. Therefore, during charging the outer layer becomes lithium-poor relative to the inner core, creating a concentration gradient. As lithium ions are extracted from the surface, the outer

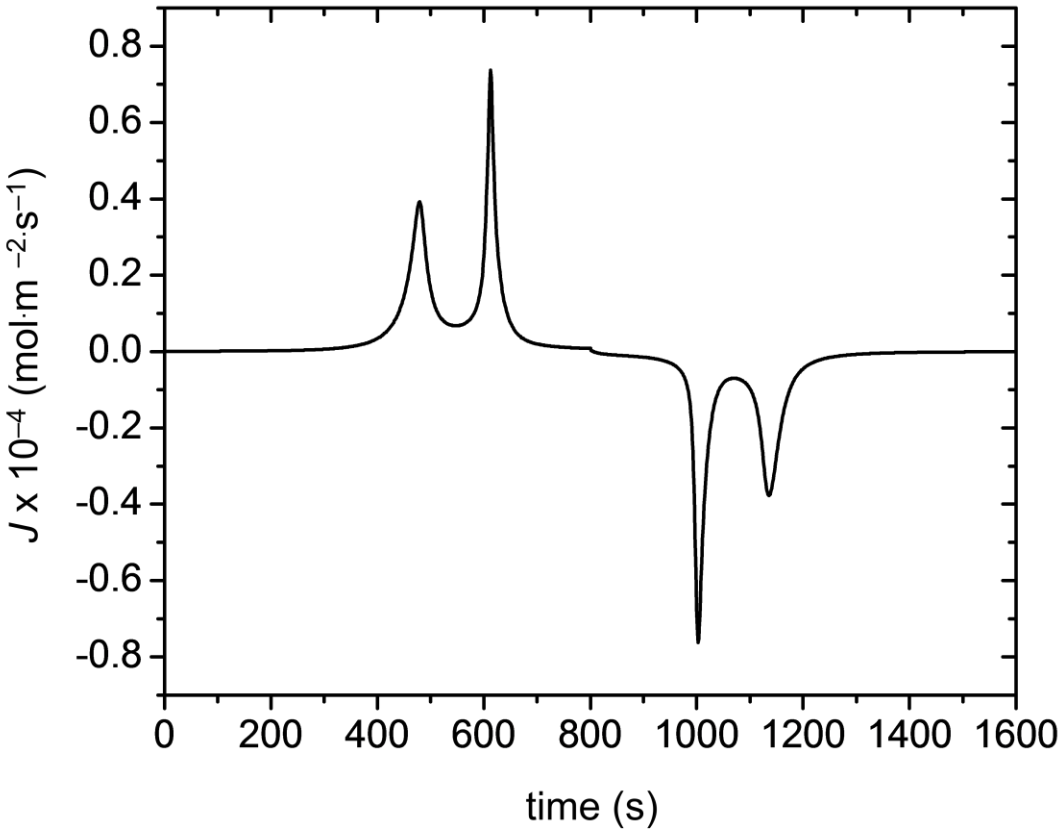

Figure 2.3: A time history of reaction flux during the potentiodynamic control simulation for a particle without grain boundary.

layer contracts and applies a compressive (negative) stress to the inner core. However, the outer layer cannot contract freely due to the inner core. As a result, it experiences a tensile (positive) stress. During discharging, the outer layer expands as lithium ions are inserted from the particle surface. In the case of discharging, the outer can expand freely, and therefore, experiences almost no stress. The inner core, on the other hand, is pulled by the expanding outer layer and experiences tensile (positive) stress.

Figure 2.4 shows the time history of the maximum first principal stress during charging and discharging for particles with and without grain boundaries. The profiles shown in Figure 2.4a correspond to a particle without grain boundary and the profiles shown in Figures 2.4b and 2.4c correspond to particles with grain boundaries. Grain boundary structures and cycling conditions in Figures 2.4b and 2.4c were identical. The only different condition between Figures 2.4b and 2.4c was the diffusion coefficient ratio, D_{gb}/D_g. Ratios of 10^3 and 10^4 were used in Fig. 2.4b and 2.4c, respectively. The three stress profiles in each figure correspond to the particle center point and two surface points located on the minor and major axes. During charging, the two surface points undergo tensile stress, while the center point undergoes compressive stress. During discharging, the surface experiences almost no stress, as it can freely expand, while the inner core experiences tensile stress. In the presence of grain boundaries, lithium ions can be inserted into and extracted from the particle inner core more rapidly through grain boundaries, lowering the overall concentration gradient as well as intercalation-induced stress during both charging and discharging. With increasing grain boundary Li^+ diffusion coefficient, intercalation-induced stress is reduced even further, as seen in Fig. 2.4c. Figure 2.5 shows the lithium ion concentration distribution at the point in time when the first principal stress is at its maximum during charge. Figures 2.5a, 2.5b, and 2.5c correspond to the particles in Figs. 2.4a,

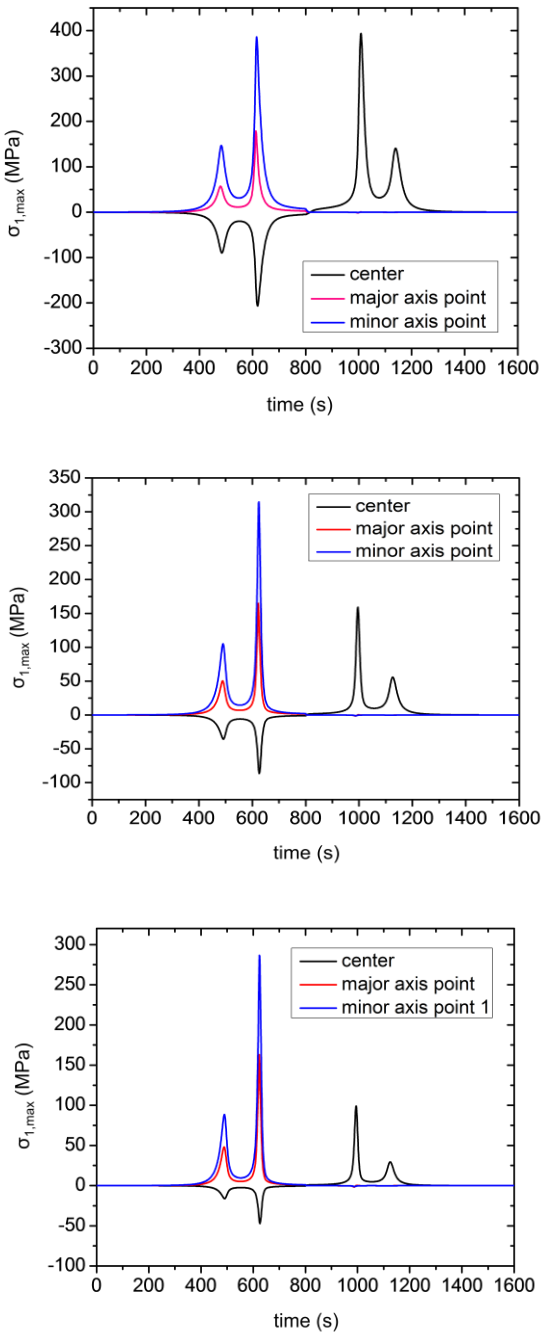

Figure 2.4: A time history of intercalation-induced stress at three specific points (particle center and two surface points located on minor and major ellipsoidal axes) during the potentiodynamic control simulation for: (top) a particle without grain boundary, (middle) a particle with a grain boundary network structure with $D_{gb}/D_g = 10^3$, and (bottom) a particle with the same grain boundary network structure as in (middle) but with $D_{gb}/D_g = 10^4$.

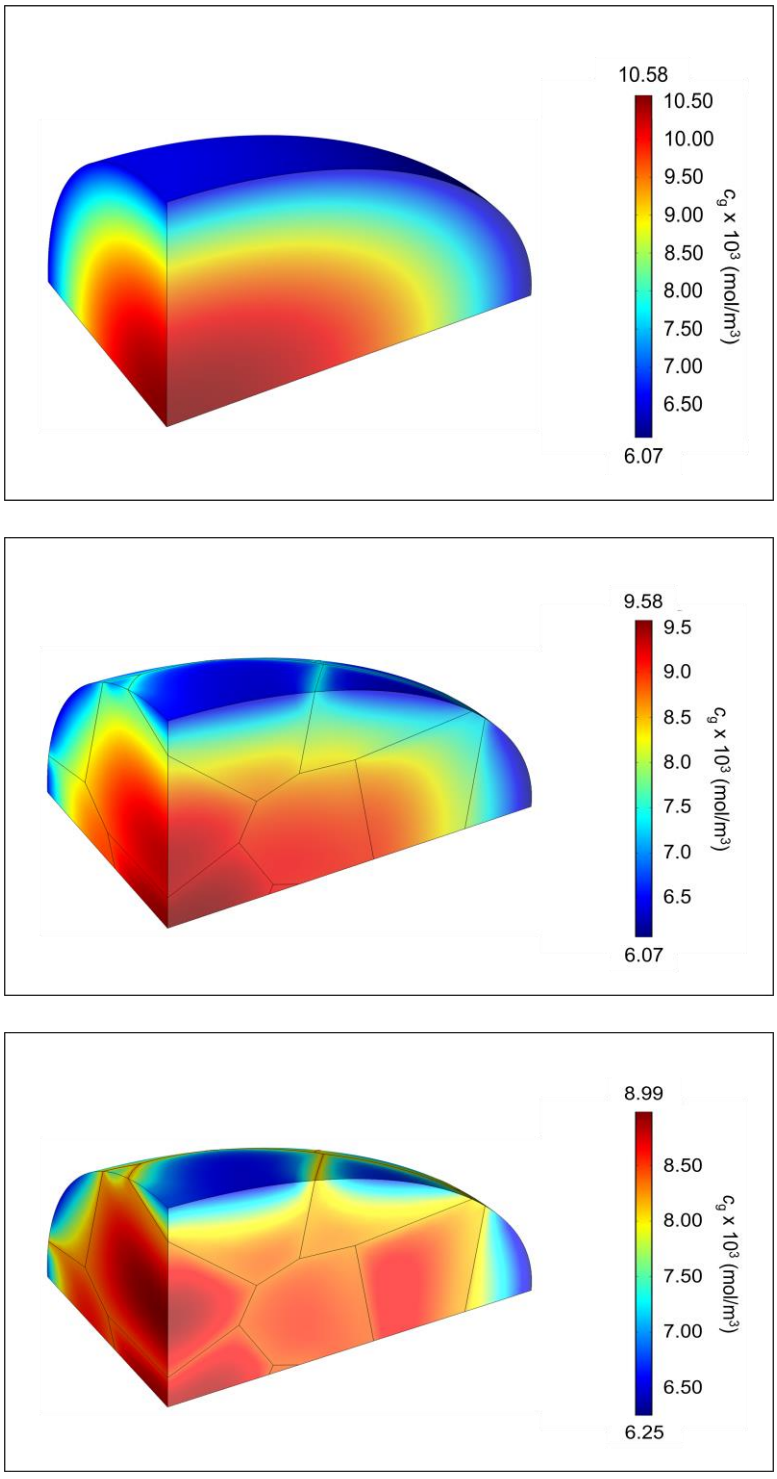

Figure 2.5: Lithium ion concentration distribution when intercalation-induced stress is at its maximum during charge for the same three particles in Figure 2.4: (top) the particle without grain boundary, (middle) the particle with a grain boundary network structure for $D_{gb}/D_g = 10^3$, and (bottom) the particle with the same grain boundary network structure as in (middle) but for $D_{gb}/D_g = 10^4$.

2.4b, and 2.4c, respectively. Lithium ion concentrations being higher along the grain boundaries near the particle surface can be clearly seen in Figs. 2.5b and 2.5c. For the three particles represented in Fig. 2.4, the maximum first principal stress experienced at the surface point located on the minor axis is higher than at the surface point located on the major axis. This is due to a higher net Li^+ concentration gradient in the minor axis than in the major axis. Fig. 2.6 shows the lithium ion concentration profiles along the minor and major axes when the intercalation-induced stress is at a maximum during charging. Figures 2.6a, 2.6b, and 2.6c correspond to the same particles in Fig. 2.4a, 2.4b, and 2.4c, respectively. For the particle without grain boundary, as represented in Fig. 2.6a, the difference between the lithium ion concentration at the particle center and at the surface points in the minor and major axes are 3,945 mol/cm^3 and 4,145 mol/cm^3, respectively. However, the minor axis length is 1.2 μm, whereas the major axis length is 2.0 μm. Hence, the net concentration gradient along the minor axis is approximately more than 50% higher than along the major axis, which leads to higher tensile stress. Moreover, the concentration decrease is monotonic along the minor and major axes for the particle without grain boundary. For particles with grain boundary, however, the concentrations along minor and major axes do not decrease monotonically, as shown in Figures 2.6b and 2.6c. Instead, the concentration increases slightly whenever a grain boundary is encountered. This concentration increase becomes pronounced when D_{gb}/D_g increases from 10^3 to 10^4, as shown in Figures 2.6b and 2.6c. When the diffusion coefficient ratio D_{gb}/D_g increases from 10^3 to 10^4, the net concentration gradient along the minor axis reduces by 29%, and the maximum principal stress decreases by 9%. For an ideal or dilute solid solution system where the activity coefficient of diffusing species is independent of concentration, intercalation- or diffusion-induced stress always enhances Li-ion diffusivity [31, 67], as described in Eq. 1. Although high diffusivity of

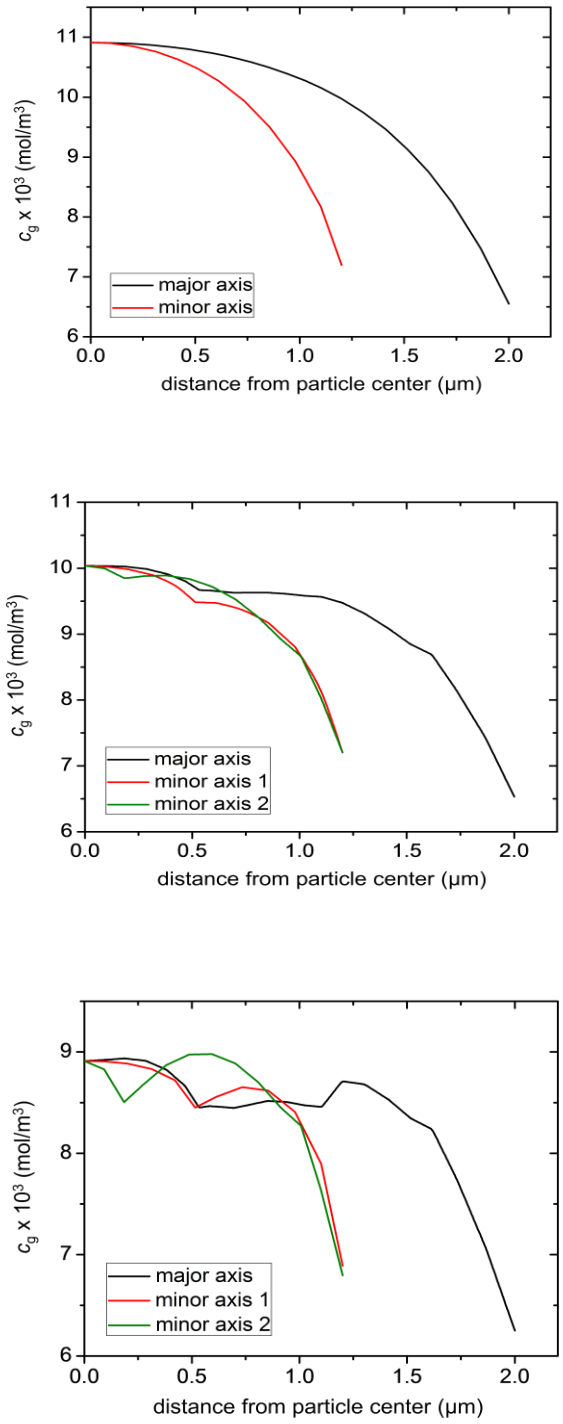

Figure 2.6: Lithium ion concentration profiles along the minor axes when intercalation-induced stress is at its maximum during charge for the same three particles in Figure 2.4: (top) the particle without grain boundary, (middle) the particle with a grain boundary network structure for $D_{gb}/D_g = 10^3$, and (bottom) the particle with the same grain boundary network structure as in (middle) but for $D_{gb}/D_g = 10^4$.

grain boundaries may reduce the enhanced diffusivity caused by intercalation-induced stress, the high diffusivity of grain boundaries itself results in even higher overall diffusivity.

Potentiodynamic control simulations were performed on 31 particles, and the maximum first principal stress induced during charging and discharging is summarized in Figures 2.7a and 2.7b, respectively. A fixed grain boundary thickness of δ = 8 nm was used for particles with grain boundaries. The maximum first principal stress generally decreases with an increasing grain boundary surface area-to-lattice volume ratio, s_{gb}/v_g. However, it does not show a strong correlation with the s_{gb}/v_g ratio (although discussed later, the apparent diffusion coefficients show a stronger correlation with increasing s_{gb}/v_g ratio). Assuming a linear relationship between $\sigma_{1,max}$ and s_{gb}/v_g, adjusted-R^2 values are 0.46 and 0.40 for charge and discharge data set, respectively. The intercalation-induced stress is primarily determined by the lithium ion concentration distribution inside particles. As seen in Figures 2.6b and 2.6c, the lithium ion concentration distribution may be modified significantly with the grain boundary network structure and the grain boundary-to-bulk diffusion coefficient ratio. To investigate the grain boundary network structure effect on intercalation-induced stress, three particles containing a single grain boundary surface with the same surface area were considered. In the first case (case 1), a grain boundary bisects a particle away from the particle center; in the second case (case 2), a grain boundary is parallel to the long axis; in the last case (case 3), a grain boundary passes through the particle center. All three cases contained a single grain boundary with an identical grain boundary surface area of 1.315 μm^2 (s_{gb}/v_g = 0.872 μm^{-1}). The time histories of intercalation-induced stress at the particle center point and two surface points located on the major and minor axes are shown in Fig. 2.8. In all three cases, the maximum stress during

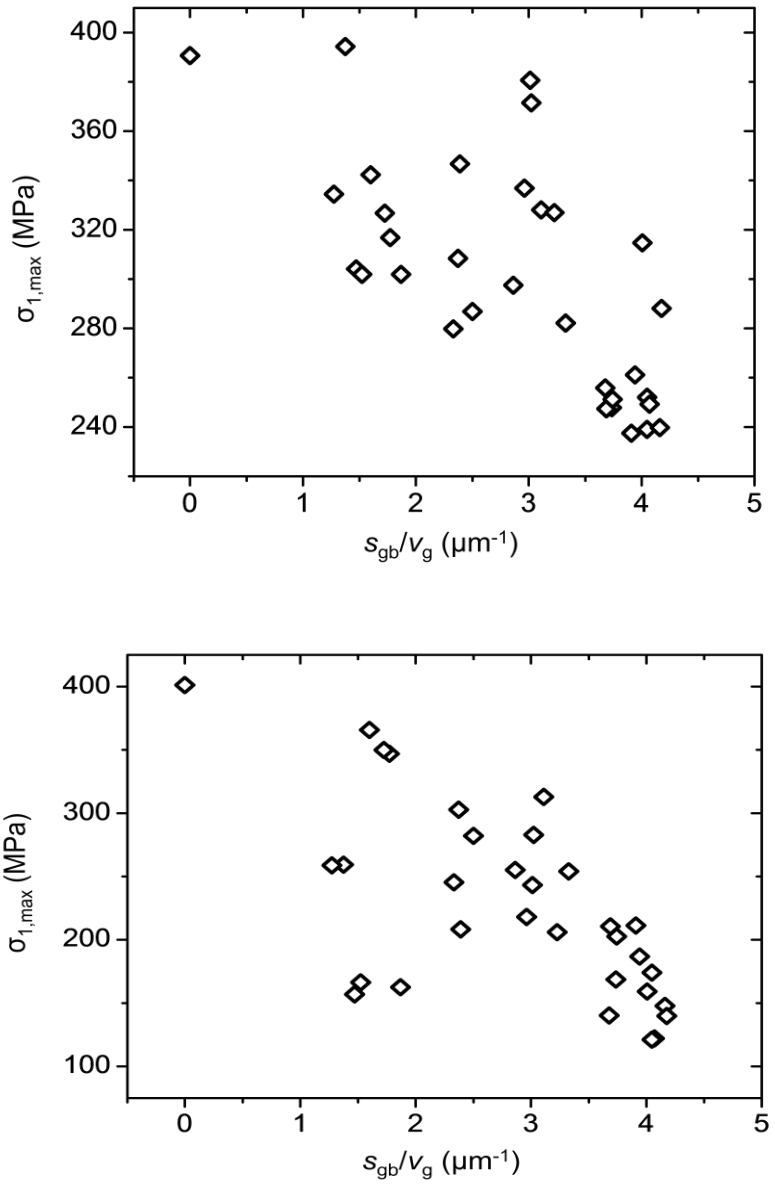

Figure 2.7: of the maximum intercalation-induced stress in the 31 particles observed during the potentiodynamic control simulation: (above) during charge and (below) during discharge.

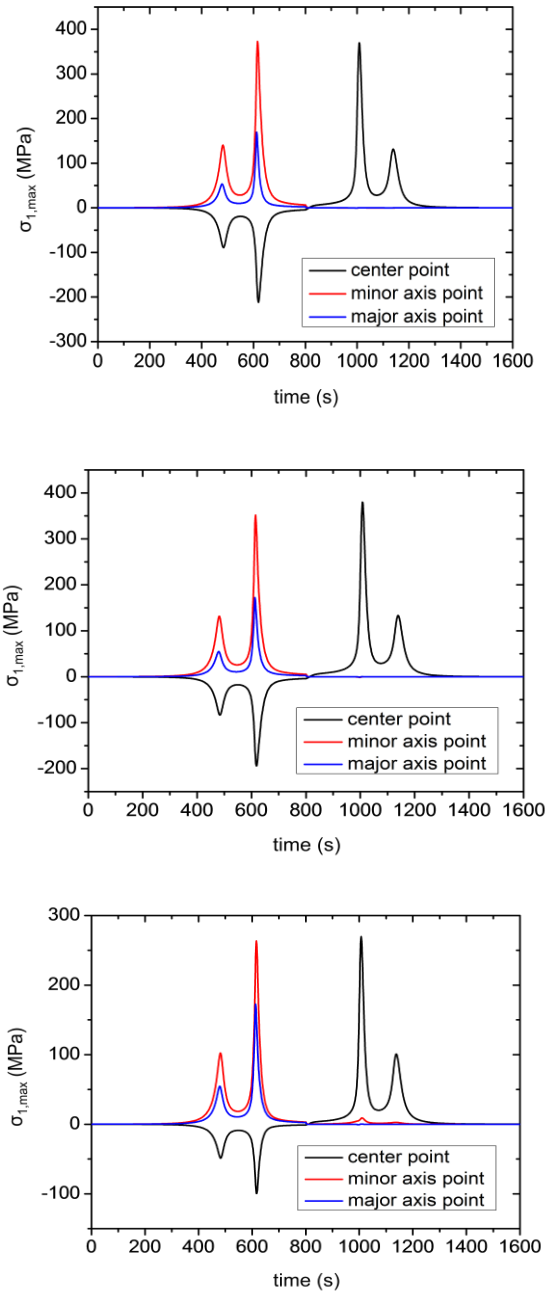

Figure 2.8: . Intercalation-induced stress profiles at three specific points (particle center and two surface points located on minor and major ellipsoidal axes) for three particles containing a single grain boundary with the same surface area oriented at different angles: (top) case 1 – a grain boundary oriented away from the particle center, (middle) case 2 – a grain boundary oriented in parallel with the major axis, and (bottom) case 3 – a grain boundary oriented such that it passes through the particle center.

charging occurs at the surface point located on the minor axis. During charging, the maximum intercalation-induced stress for the three cases is 372 MPa for case 1, 368 MPa for case 2, and 330 MPa for case 3. During discharging, the maximum intercalation-induced stress at the particle center is 369 MPa for case 1, 380 MPa for case 2, and 270 MPa for case 3. Fig. 2.9 shows the concentration along the minor axis for the three cases when intercalation-induced stress is at their maximum during charge. Also Fig. 2.10 shows the 3D lithium ion concentration distribution for the three particles when intercalation-induced stress is at their maximum during charging. The three cases demonstrate that an orientation of a grain boundary itself can have an influence on the maximum intercalation-induced stress by modifying Li^+ concentration gradients within particles.

The Grain Boundary Effect on Li^+ Diffusivity

Figure 2.11 shows the computed apparent diffusion coefficients as a function of grain surface-area-to-particle-volume ratios s_{gb}/v_g for various grain boundary thicknesses. The apparent diffusion coefficients are based on the first reaction flux peak during discharge. For a given grain boundary thickness, the apparent diffusion coefficient increases almost linearly in the tested s_{gb}/v_g range. Assuming a linear relationship between D_{app} and s_{gb}/v_g, adjusted-R^2 values do range between 0.91 and 0.92 for all grain boundary thicknesses. Moreover, as the grain boundary thickness increases, apparent diffusion coefficients rise faster with s_{gb}/v_g. This is because in the governing equation for the lithium ion transport in the grain boundary domain, as described in Eq. 15, the grain boundary thickness, δ, and the grain boundary diffusion coefficient, D_{gb}, are multiplied together and input as a constant. Therefore, the two effects are confounded in the model. For example, a twofold increase in the

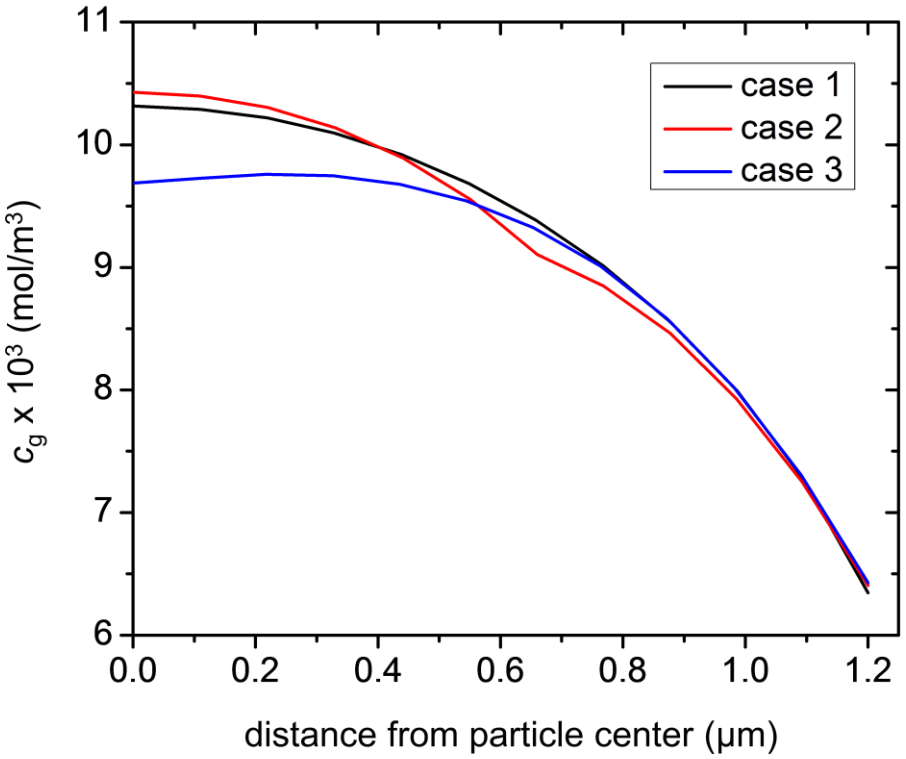

Figure 2.9: Lithium ion concentration profiles along the minor axes when intercalation-induced stress is at its maximum during charging for the same three particles containing a single grain boundary: Case 1 – a grain boundary oriented away from the particle center, Case 2 – a grain boundary oriented in parallel with the major axis, and Case 3 – a grain boundary oriented such that it passes through the particle center.

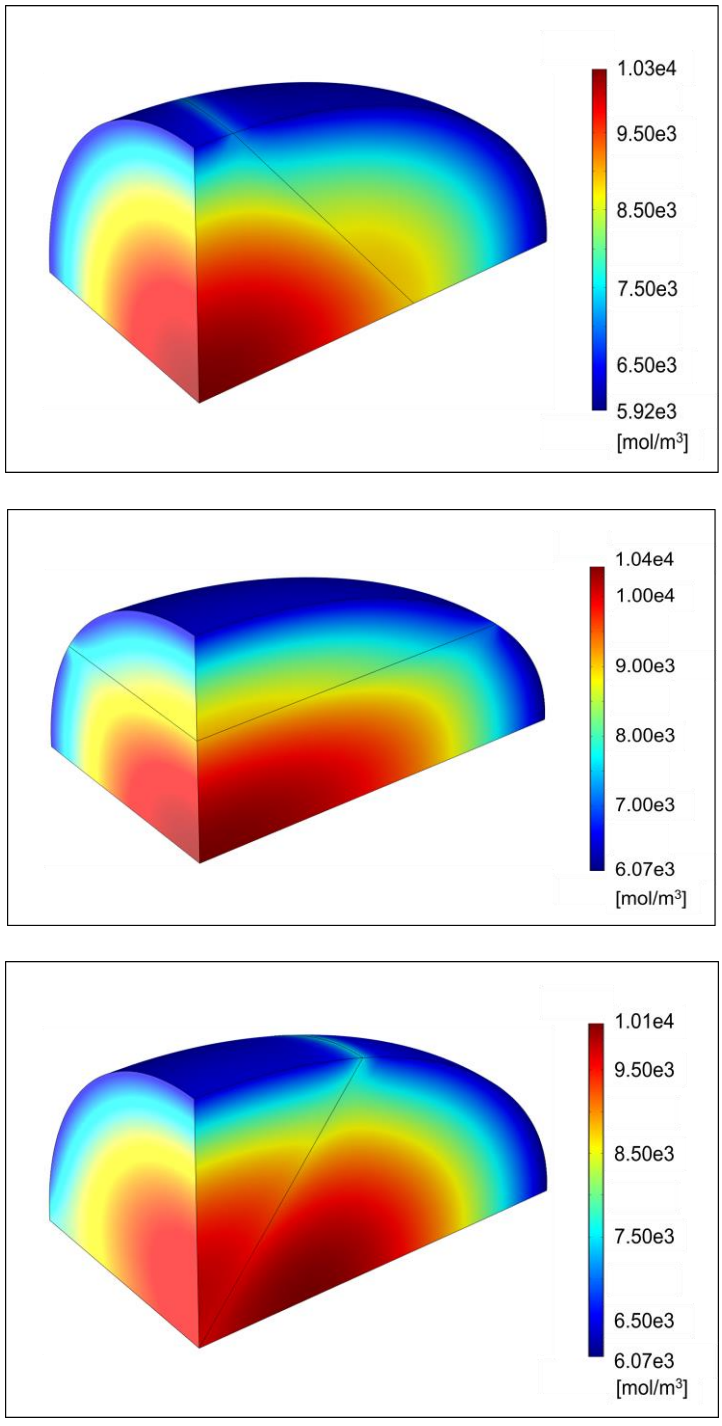

Figure 2.10: . 3D surface plots of lithium ion concentrations when the maximum intercalation-induced stress has reached its maximum during charge for the three particles containing a single grain boundary: (top) Case 1 particle, (middle) Case 2 particle, and (bottom) Case 3 particle.

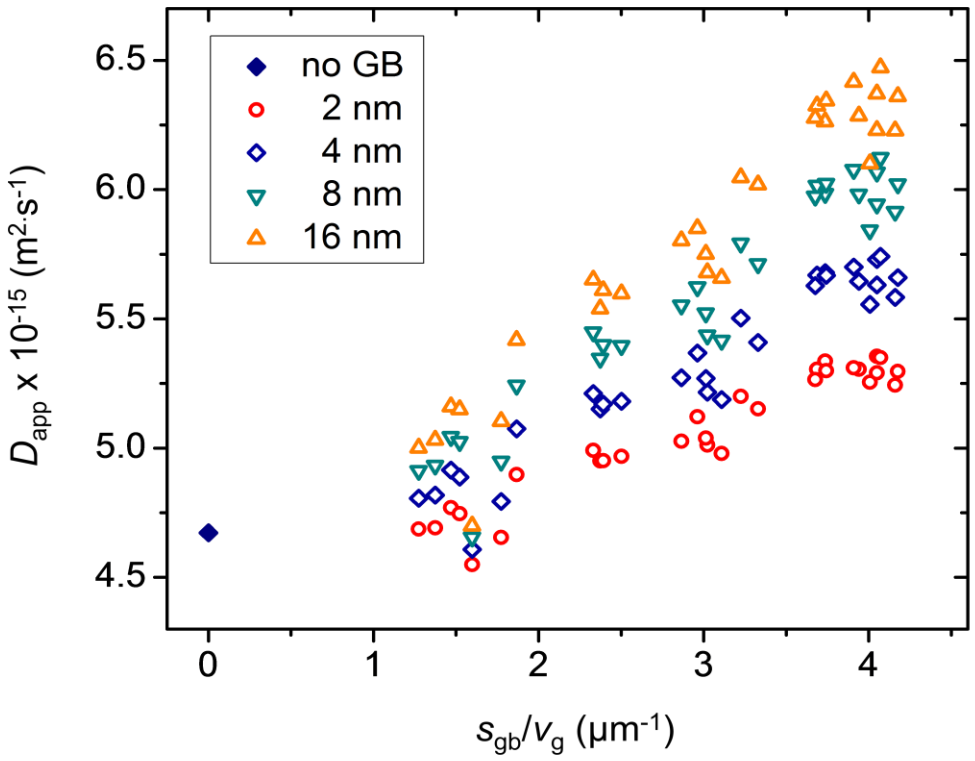

Figure 2.11: A summary of apparent diffusion coefficients based on the second reaction flux peak during discharge for the 31 particles with a fixed diffusion coefficient ratio, D_{gb}/D_g = 1,000 but varying grain boundary thicknesses.

grain boundary thickness yields the same results as a twofold increase in the grain boundary diffusion coefficient.

To investigate the individual effect of grain boundary diffusion coefficient and the thickness on diffusivity, a 2D model containing an actual grain boundary thickness was considered. The shape of the cathode particle was a circle with 2 μm radius and assuming symmetry about *x*- and *y*-axes, only a quarter of the circle was modeled. A schematic image of the cathode particle is shown in Fig. 2.12. In parallel with the 3D model, the 2D model included the plane thermal-analogy intercalation-induced stress in the grain domain only. Two sets of potentiodynamic control simulations were performed with the 2D model. In the first set, a grain boundary thickness was fixed while the grain boundary diffusion coefficient varied, while in the second set, the grain boundary diffusion coefficient was fixed while the grain boundary thickness varied. The design of experiments is summarized in Table 2.4 and the same material properties in Table 2.2 were used.

Apparent Li^+ diffusion coefficients evaluated from the two sets of simulations are summarized in Fig. 2.13. Using Eq. 22, diffusion coefficients are evaluated based on the first reaction flux peak during charging. In the first set, D_{app} increases with increasing D_{gb}/D_g ratio although the D_{app} quickly approaches a saturation limit. In the second set, in contrast, D_{app} peaks when δ = 16 nm then decreases with a further increase in the grain boundary thickness. Because D_{app} is proportional to the reaction flux squared, the reaction flux contributions from grain and grain boundary domains are calculated separately and shown in Fig. 2.14.

In the first set, as grain boundary diffusion coefficient increases, the species flux contribution from the grain boundary remains almost the same whereas the reaction flux

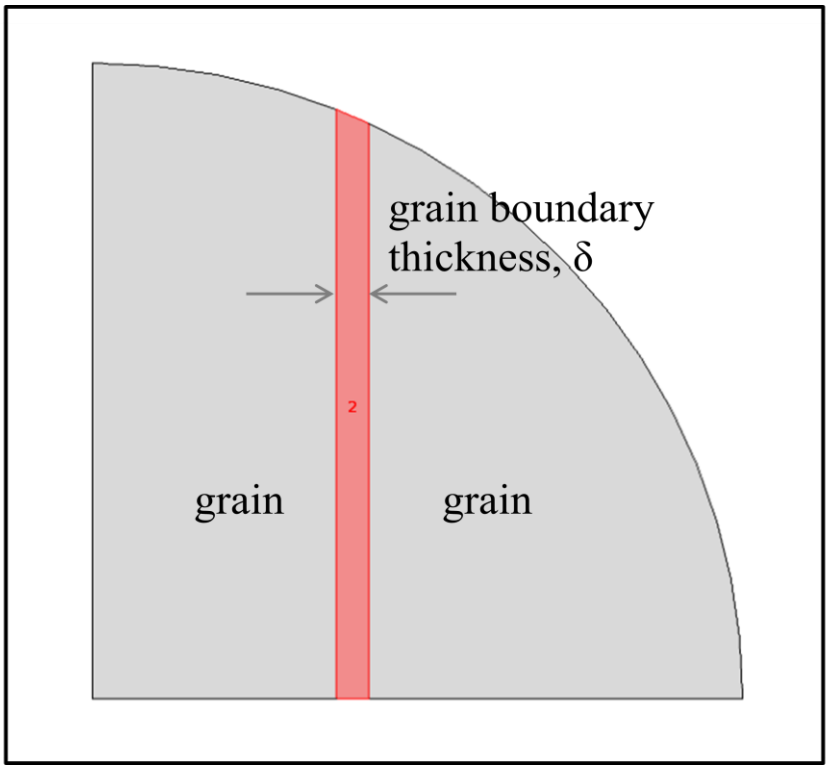

Figure 2.12: schematic diagram of a 2D particle containing a single grain boundary.

	Fixed variable/value	**D_{gb}/D_g levels**				
Set 1	δ = 4 nm	1000	2000	4000	8000	16000
		δ levels				
Set 2	D_{gb}/D_g = 1000	4 nm	8 nm	16 nm	32 nm	64 nm

Table 2.4: 2D grain boundary simulation design of experiment table.

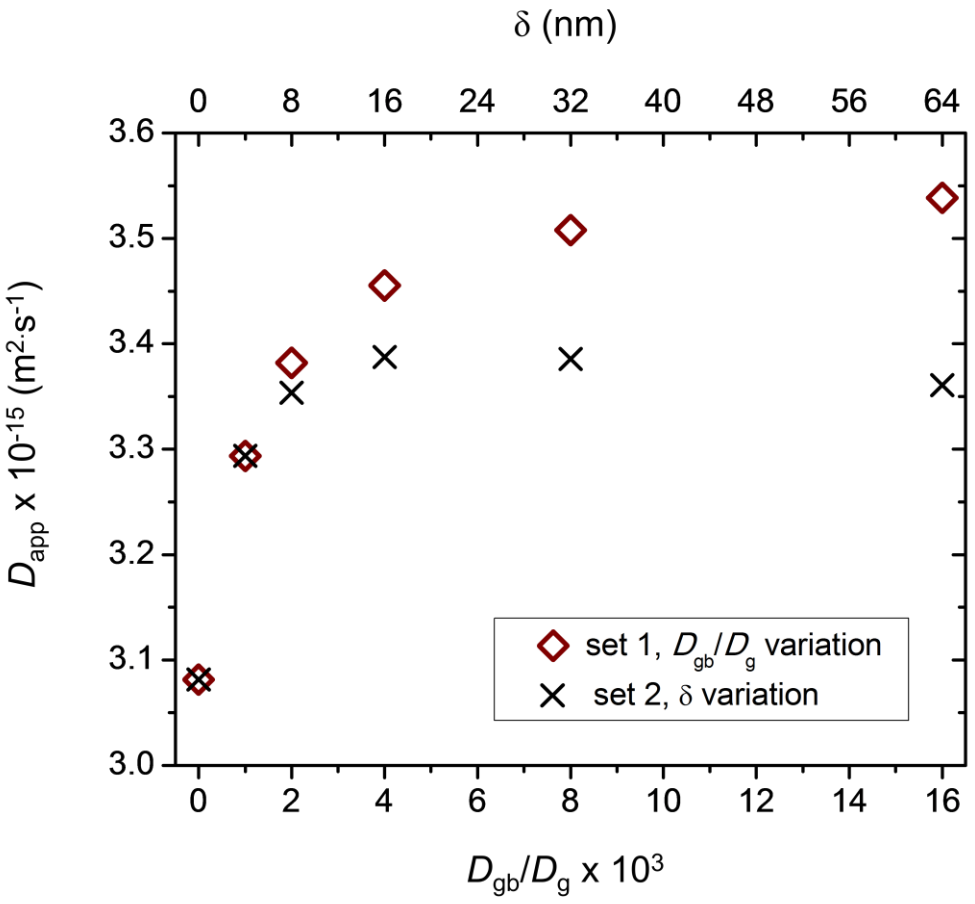

Figure 2.13: A summary of apparent diffusion coefficients based on the first reaction flux peak during charging from the 2D simulation.

contribution from the grain increases, as shown in Fig. 2.14a. With higher grain boundary diffusion coefficient, lithium ions can travel faster along a grain boundary. Due to the condition that the concentration at the grain/grain boundary interface needs to be equal, the increase in the grain boundary diffusion coefficient induces higher concentration gradient as well as species flux in the grain domain. Although not shown here, the magnitude of the concentration gradient increases in the grain domain with increasing D_{gb}. This implies that the diffusivity in the grain boundary affects the diffusivity in the bulk domain. The reason for the reaction flux contribution from the grain boundary remaining almost the same is as follows. Owing to the relatively higher lithium ion diffusivity in the grain boundary, a higher concentration of lithium ions are inserted to and extracted from the grain via the grain boundary. As a result, the average lithium ion concentration in the grain boundary, c_{gb}, falls more slowly during charging and rises more quickly during discharging compared to the average lithium ion concentration in the bulk or grain, c_g. Because the model assumes that OCP is a function of lithium ion concentration in both the grain and grain boundary domains, the potential in the grain boundary domain increases more slowly during charging and decrease more rapidly compared to the potential in the grain domain. Due to the concentration difference, given an applied potential, the surface overpotential and the time location of the reaction flux peaks are different at the grain/electrolyte interface and the grain boundary/electrolyte interface. As an example, Fig. 2.15a shows the time history of the total reaction flux during charge/discharge for a case where D_{gb}/D_g = 1,000 and δ = 16 nm. The reaction flux at the grain/electrolyte and grain boundary/electrolyte interfaces are plotted separately in Figures 2.15b and 2.15c, respectively. The first reaction flux peak at the grain-

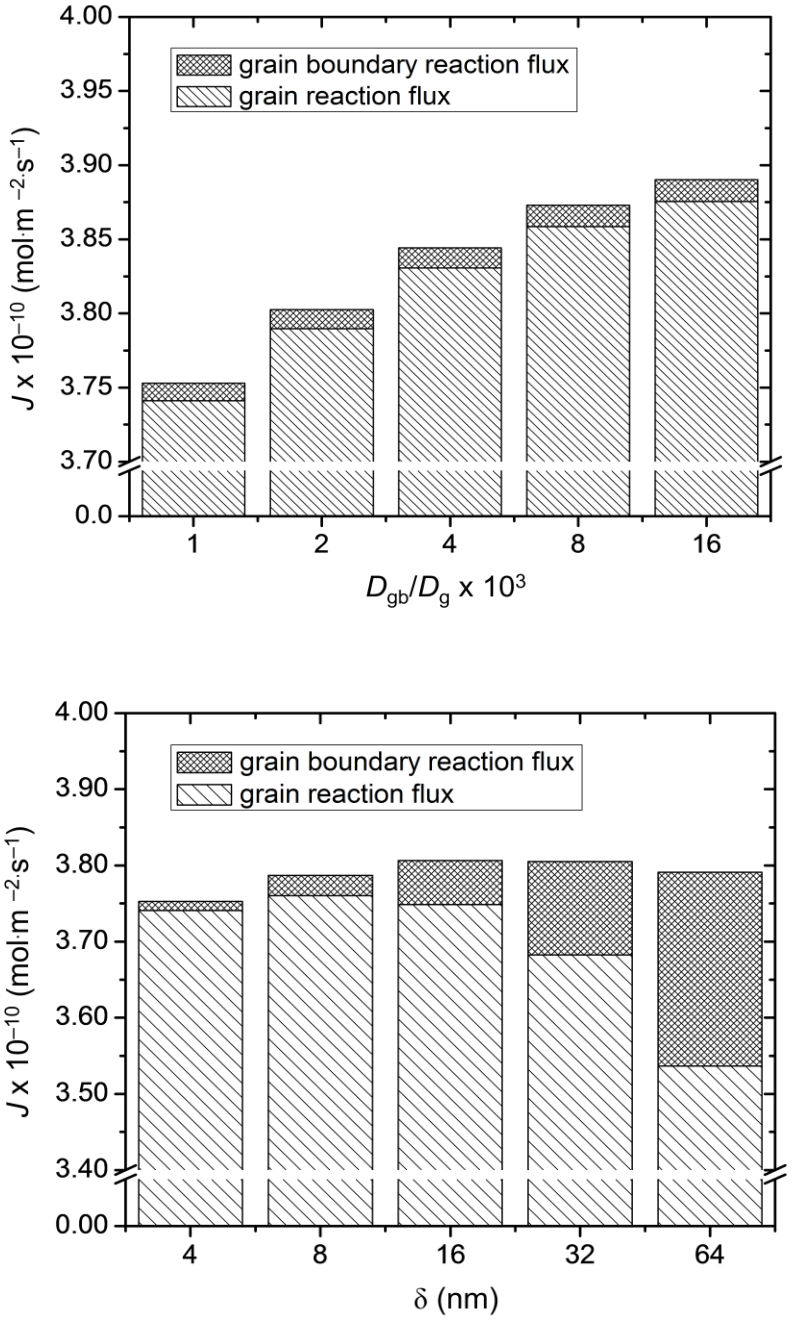

Figure 2.14: Reaction flux contributions from bulk and grain boundary domains: (above) set 1 – where the grain boundary diffusivity is a variable and (below) set 2 – where the grain boundary thickness a variable.

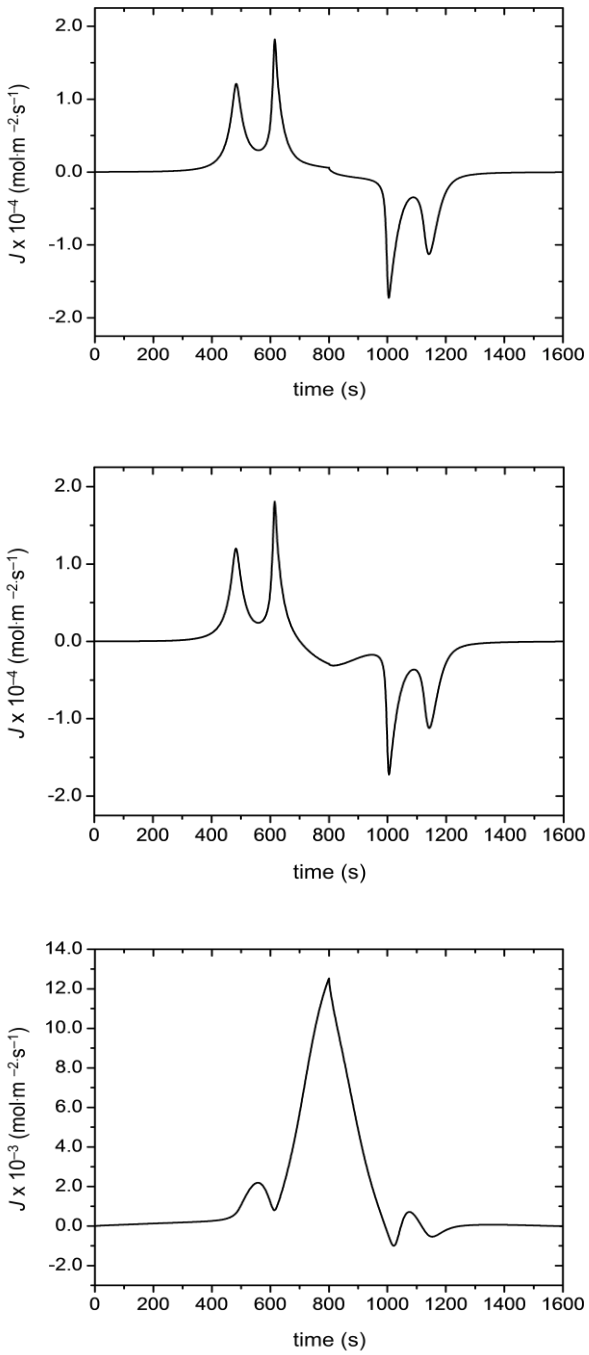

Figure 2.15: A time history of the reaction flux from a 2D particle with $D_{gb}/D_g = 10^3$ and $\delta = 16$ nm: (top) total reaction flux, (middle) reaction flux from the bulk/grain domain, and (bottom) reaction flux from the grain boundary domain.

electrolyte occurs at t = 483 s, whereas the first reaction flux peak at the grain boundary-electrolyte interface occurs at t = 558 s. Because the apparent diffusion coefficient is evaluated based on the overall reaction flux peak, the reaction flux at the grain boundary-electrolyte interface is evaluated before its first peak is reached. This illustrates why the reaction flux contribution from the grain boundary does not increase with increasing grain boundary diffusion coefficient.

In the second set, the reaction flux contribution from the grain boundary is approximately doubled as δ becomes a twofold, as shown in Fig. 2.14b. In contrast, the reaction flux contribution from the grain increases slightly from δ = 4 to δ = 8 then decreases with a further increase in the grain boundary thickness. There are two competing factors that affect species flux. The first is the concentration gradient and the second is the domain size. With increasing grain boundary thickness, the magnitude of the concentration gradient increases just like in the first set of simulations. On the other hand, the total number of lithium ions flowing from the grain decreases with shrinking domain size. Hence, the reaction flux contribution in the grain domain increases only to a certain grain boundary thickness threshold.

Grain Boundary Effect on Capacity Utilization

The two sets of particles were discharged with various C-rates, and their capacity utilizations were computed according to Eq. 22. The resulting capacity utilizations as a function of C-rates and grain boundary-surface-area-to-particle-volume ratio, s_{gb}/v_g, were then fitted with a second order polynomial surface; they are shown in Fig. 2.15. The surface fits shown in Figures 2.16a and 2.16b correspond to the first and second sets of particles, respectively. The s_{gb}/v_g ratio is normalized to its highest value. The two sets of particles show decreasing capacity utilization with increasing C-rates and decreasing s_{gb}/v_g ratio. At C/5 and lower, the capacity

utilization is 97% or higher for all particles in both sets, including the particles without grain boundary. In the first set, the particle without a grain boundary retains capacity utilizations of 94% and 90% at C-rates of 5C for 10C, respectively. In the presence of the grain boundary, the average capacity utilization increases to 98% for 5C and 96% for 10C. Conversely, in the second set, the capacity utilization of the particle without grain boundary is 74% and 61% at C-rates of 5C and 10C, respectively. The decrease in the capacity utilization in the second set is due to increased particle volume by a factor of 2.5^3 while the bulk diffusion length is fixed. In the presence of the grain boundary, the average capacity utilization increases to 85% for 5C and 73% for 10C. The marginal increase in the capacity utilization is appreciably greater in the second set despite that the grain boundary-surface-area-to-particle-volume, s_{gb}/v_g, is 2.5^2 lower compared to the smaller particles in the first set. Nonetheless, the overall trend of increasing capacity with grain boundary surface-area-to-particle-volume is consistent with increasing apparent diffusion coefficient with surface area-to-particle volume. Although capacity utilization tends to increase with grain boundary density, the particle with the highest s_{gb}/v_g ratio does not achieve the maximum capacity utilization. For example, with equal particle sizes, a particle with $s_{gb}/v_g = 4.0$ μm^{-1} achieves a capacity utilization of 89% while a particle with $s_{gb}/v_g = 10.4$ μm^{-1} achieves a capacity utilization of 84% when the C-rate is 5C. This shows that a grain boundary network structure can influence capacity utilization. To improve Li-ion battery power performance in composite electrodes, the average particle sizes have been reduced by various synthesis techniques and mechanical means. However, increasing electrode-electrolyte interfacial density may lead to higher capacity degradation due to increased side reactions [96-97] and dissolution [98]. To suppress such phenomena, surface coating on Li- ion cathodes has often been performed

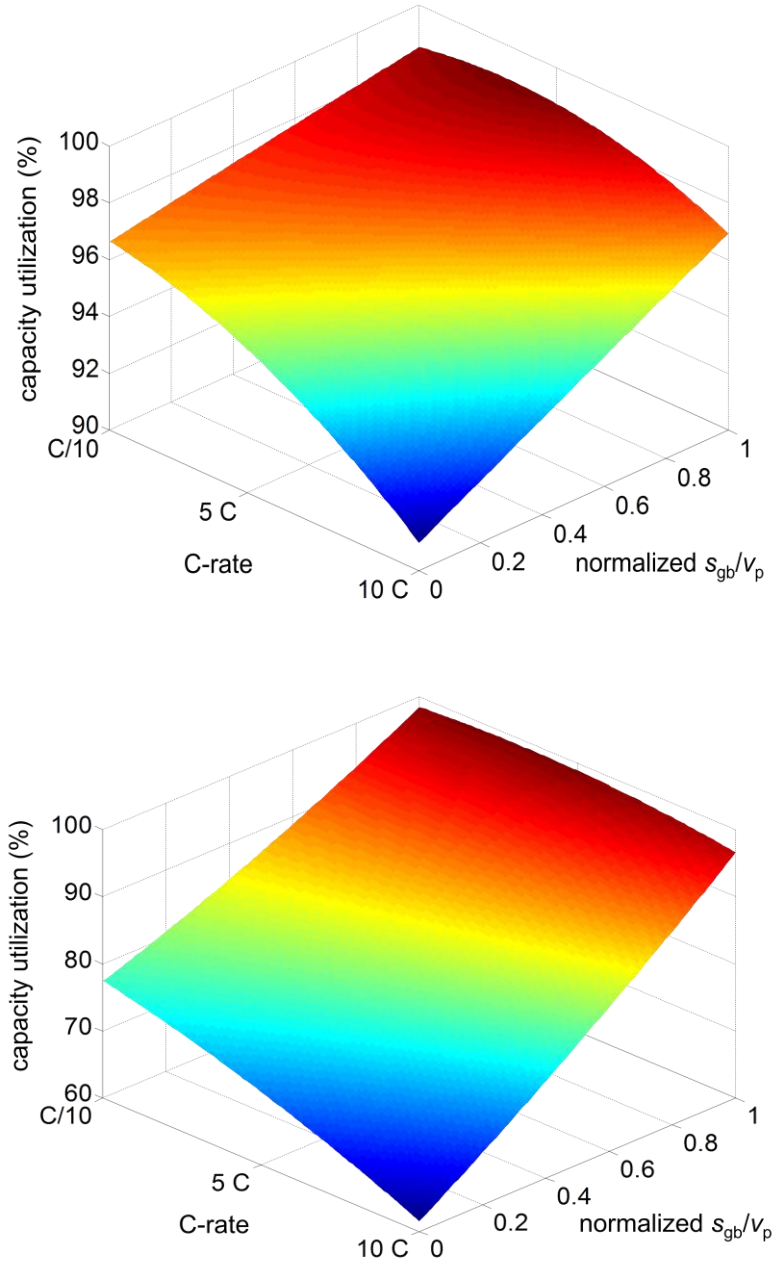

Figure 2.16: Second order surface fits of capacity utilization results from particles under the galvanostatic control simulation: (above) particles with the dimensions of the 2 x 1.2 x 1.2 μm^3 case and (below) particles with the dimensions of the 5 x 3 x 3 μm^3 case.

[99-100]. The same effect may be achieved without coating but by utilizing the grain boundary network structure. As grain boundaries can have an influence on Li^+ transport, intercalation-induced stress, and even phase transformation sites, grain boundary engineering Li-ion active materials may be an alternative avenue to enhance Li-ion battery performance.

CONCLUSIONS

The grain boundary effect on intercalation-induced stress, Li^+ diffusivity, and capacity utilization was investigated by implementing 2D Voronoi grain boundary structures embedded inside 3D $LiMn_2O_4$ particles. The main cause of intercalation-induced stress inside a single cathode particle is the lithium ion concentration gradient developed during charging and discharging. The net concentration gradient was reduced with the inclusion of high diffusion grain boundary pathways. Consequently, the maximum intercalation-induced stress also decreased. Although the maximum intercalation-induced stress tended to diminish with increasing grain boundary density, the actual stress level exhibited a high dependence on individual grain boundary network geometries. While intercalation-induced stress tended to be reduced in the presence of the grain boundary, the computed apparent diffusion coefficient, as well as the capacity utilization, increased. As discussed above, grain boundaries may have a significant role in determining the performance of Li-ion secondary batteries. Moreover, grain boundaries are inevitable in commercially available Li-ion active materials. For these reasons, grain boundaries should be controlled during synthesis in order to enhance the performance of Li-ion secondary batteries.

BIBLIOGRAPHY

1. J. Christensen and J. Newman, Journal of the Electrochemical Society **153** (6), A1019-A1030 (2006).

2. H. Haftbaradaran, J. Song, W. A. Curtin and H. Gao, Journal of Power Sources **196** (1), 361-370 (2011).

3. X. Zhang, W. Shyy and A. M. Sastry, Journal of the Electrochemical Society **154** (10), A910-A916 (2007).

4. J. Park, W. Lu and A. M. Sastry, Journal of the Electrochemical Society **158** (2), A201-A206 (2011).

5. C. S. Wang, U. S. Kasavajjula and P. E. Arce, Journal of Physical Chemistry C **111**, 16656-16663 (2007).

6. Y. J. Zhu and C. S. Wang, Journal of Physical Chemistry C **114** (6), 2830-2841 (2010).

7. N. Meethong, Y. H. Kao, M. Tang, H. Y. Huang, W. C. Carter and Y. M. Chiang, Chemistry of Materials **20** (19), 6189-6198 (2008).

8. R. Malik, D. Burch, M. Bazant and G. Ceder, Nano Letters **10** (10), 4123-4127 (2010).

9. S. Adams and R. P. Rao, Solid State Ionics **184** (1), 57-61 (2011).

10. J. Horvath, R. Birringer and H. Gleiter, Solid State Communications **62** (5), 319-322 (1987).

11. T. Mutschele and R. Kirchheim, Scripta Metallurgica **21** (2), 135-140 (1987).

12. Y. R. Kolobov, G. P. Grabovetskaya, M. B. Ivanov, A. P. Zhilyaev and R. Z. Valiev, Scripta Materialia **44** (6), 873-878 (2001).

13. J. C. Fisher, Journal of Applied Physics **22** (1), 74-77 (1951).

14. E. W. Hart, Acta Metallurgica **5** (10), 597-597 (1957).

15. I. V. Belova and G. E. Murch, Journal of Physics and Chemistry of Solids **64** (5), 873-878 (2003).

16. I. V. Belova and G. E. Murch, Nanodiffusion **19**, 25-33 (2004).

17. Y. Chen and C. A. Schuh, Journal of Applied Physics **101** (6) (2007).

18. Y. Chen and C. A. Schuh, Scripta Materialia **57** (3), 253-256 (2007).

19. L. G. Harrison, Transactions of the Faraday Society **57** (8), 1191-& (1961).

20. Y. Mishin and C. Herzig, Materials Science and Engineering a-Structural Materials Properties Microstructure and Processing **260** (1-2), 55-71 (1999).

21. H. Xia and L. Lu, Electrochimica Acta **52** (24), 7014-7021 (2007).

22. Y. S. Cohen and D. Aurbach, Electrochemistry Communications **6** (6), 536-542 (2004).

23. W. S. Kim, Journal of Power Sources **134** (1), 103-109 (2004).

24. S. C. Mui, J. Jasinski, V. J. Leppert, M. Mitome, D. R. Sadoway and A. M. Mayes, Journal of the Electrochemical Society **153** (7), A1372-A1377 (2006).

25. N. Balke, S. Jesse, A. N. Morozovska, E. Eliseev, D. W. Chung, Y. Kim, L. Adamczyk, R. E. Garcia, N. Dudney and S. V. Kalinin, Nature Nanotechnology **5** (10), 749-754 (2010).

26. L. Y. Beaulieu, D. Larcher, R. A. Dunlap and J. R. Dahn, Journal of the Electrochemical Society **147** (9), 3206-3212 (2000).

27. U. Kasavajjula, C. S. Wang and A. J. Appleby, Journal of Power Sources **163** (2), 1003-1039 (2007).

28. W. J. Zhang, Journal of Power Sources **196** (1), 13-24 (2011).

29. H. F. Wang, Y. I. Jang, B. Y. Huang, D. R. Sadoway and Y. T. Chiang, Journal of the Electrochemical Society **146** (2), 473-480 (1999).

30. M. R. Lim, W. I. Cho and K. B. Kim, Journal of Power Sources **92** (1-2), 168-176 (2001).

31. D. Y. Wang, X. D. Wu, Z. X. Wang and L. Q. Chen, Journal of Power Sources **140** (1), 125-128 (2005).

32. R. Kostecki and F. McLarnon, Electrochemical and Solid State Letters **7** (10), A380-A383 (2004).

33. F. Q. Yang, Materials Science and Engineering a-Structural Materials Properties Microstructure and Processing **409** (1-2), 153-159 (2005).

34. J. Chenminli and R. F. Mehl, Metallurgical Transactions a-Physical Metallurgy and Materials Science **9** (10), 1353-1380 (1978).

35. W. I. F. David, M. M. Thackeray, L. A. Depicciotto and J. B. Goodenough, Journal of Solid State Chemistry **67** (2), 316-323 (1987).

36. S. Prussin, Journal of Applied Physics **32** (10), 1876-1881 (1961).

37. D. Gryaznov, J. Fleig and J. Maier, Solid State Sciences **10** (6), 754-760 (2008).

38. J. Newman and K. E. Thomas-Alyea, *Electrochemical Systems*, 3rd ed. (John Wiley & Sons, Inc., New Jersey, 2004).

39. D. Zhang, B. N. Popov and R. E. White, Journal of the Electrochemical Society **147** (3), 831-838 (2000).

40. M. Doyle, J. Newman, A. S. Gozdz, C. N. Schmutz and J. M. Tarascon, Journal of the Electrochemical Society **143** (6), 1890-1903 (1996).

41. N. Yabuuchi, Y. Koyama, N. Nakayama and T. Ohzuku, Journal of the Electrochemical Society **152** (7), A1434-A1440 (2005).

42. T. H. Cho, S. M. Park, M. Yoshio, T. Hirai and Y. Hideshima, Journal of Power Sources **142** (1-2), 306-312 (2005).

43. M. Higuchi, K. Katayama, Y. Azuma, M. Yukawa and M. Suhara, Journal of Power Sources **119**, 258-261 (2003).

44. X. M. He, J. J. Li, Y. Cai, C. Y. Jiang and C. R. Wan, Materials Chemistry and Physics **95** (1), 105-108 (2006).

45. L. Q. Zhang, T. Yabu and I. Taniguchi, Materials Research Bulletin **44** (3), 707-713 (2009).

46. S. H. Park, C. S. Yoon, S. G. Kang, H. S. Kim, S. I. Moon and Y. K. Sun, Electrochimica Acta **49** (4), 557-563 (2004).

47. J. R. Wilson, J. S. Cronin, S. A. Barnett and S. J. Harris, Journal of Power Sources **196** (7), 3443-3447 (2011).

48. D. W. Shin, J. W. Choi, J. P. Ahn, W. K. Choi, Y. S. Cho and S. J. Yoon, Journal of the Electrochemical Society **157** (5), A567-A570 (2010).

49. J. B. Bates, N. J. Dudney, B. J. Neudecker, F. X. Hart, H. P. Jun and S. A. Hackney, Journal of the Electrochemical Society **147** (1), 59-70 (2000).

50. Z. G. Lu, H. Cheng, M. F. Lo and C. Y. Chung, Advanced Functional Materials **17** (18), 3885-3896 (2007).

51. H. Xia, L. Lu and M. O. Lai, Electrochimica Acta **54** (25), 5986-5991 (2009).

52. D. R. Clarke, Journal of the American Ceramic Society **70** (1), 15-22 (1987).

53. G. D. West, J. M. Perkins and M. H. Lewis, Journal of Materials Science **39** (22), 6687-6704 (2004).

54. C. Dupas-Bruzek, T. N. Tingle, H. W. Green, N. Doukhan and J. C. Doukhan, Physics and Chemistry of Minerals **25** (7), 501-514 (1998).

55. A. C. S. Sabioni, A. M. Huntz, F. Silva and F. Jomard, Materials Science and Engineering a-Structural Materials Properties Microstructure and Processing **392** (1-2), 254-261 (2005).

56. A. Atkinson, Solid State Ionics **12** (MAR), 309-320 (1984).

57. H. Haneda, I. Sakaguchi, A. Watanabe, T. Ishigaki and J. Tanaka, Journal of Electroceramics **4**, 41-48 (1999).

58. T. Okumura, T. Fukutsuka, Y. Uchimoto, N. Sakai, K. Yamaji and H. Yokokawa, Journal of Power Sources **189** (1), 643-645 (2009).

59. A. Thorvaldsen, Acta Materialia **45** (2), 587-594 (1997).

60. I. f. Automatik, Multi Parametric Toolbox (MPT), http://control.ee.ethz.ch/~mpt/ (accessed on Aug. 3, 2011).

61. R. P. Frankenthal and I. Shain, Journal of the American Chemical Society **78** (13), 2969-2973 (1956).

62. A. J. Bard and L. R. Faulkner, *Electrochemical Methods: Fundamentals and Applications*, 2nd ed. (John Wiley & Sons, Inc., 2001).

63. I. Uchida, H. Fujiyoshi and S. Waki, Journal of Power Sources **68** (1), 139-144 (1997).

64. J. Vetter, P. Novak, M. R. Wagner, C. Veit, K. C. Moller, J. O. Besenhard, M. Winter, M. Wohlfahrt-Mehrens, C. Vogler and A. Hammouche, Journal of Power Sources **147** (1-2), 269-281 (2005).

65. M. Holzapfel, A. Wursig, W. Scheifele, J. Vetter and P. Novak, Journal of Power Sources **174** (2), 1156-1160 (2007).

66. S. J. Wen, T. J. Richardson, L. Ma, K. A. Striebel, P. N. Ross and E. J. Cairns, Journal of the Electrochemical Society **143** (6), L136-L138 (1996).

67. L. J. Fu, H. Liu, C. Li, Y. P. Wu, E. Rahm, R. Holze and H. Q. Wu, Solid State Sciences **8** (2), 113-128 (2006).

68. C. Li, H. P. Zhang, L. J. Fu, H. Liu, Y. P. Wu, E. Ram, R. Holze and H. Q. Wu, Electrochimica Acta **51** (19), 3872-3883 (2006).

CHAPTER III

IN-SITU ATOMIC FORCE MICROSCOPY OF VOLUME EXPANSION IN $LIMN_2O_4$ MATERIAL AND ITS CORRELATION TO DIFFUSION AND PARTICLE MORPHOLOGY

INTRODUCTION

$Li_xMn_2O_4$ systems still remain of practical relevance to the field of rechargeable batteries, in terms of high voltage, low cost, abundance, and reduced toxicity. Stoichiometric $Li_{1.0}Mn_2O_4$ belongs to the space group Fd3m with cubic spinel phase structure and its cubic lattice parameter ranges from 8.232 to 8.255 Å [1-4]. At an average composition range of $0.27 < x \leq 1.00$ in $Li_xMn_2O_4$, the reduction proceeds in cubic phases with a *ca*. 7.4% unit cell volume expansion [1]. Furthermore, at an average composition range of $1.0 < x \leq 2.0$ in $Li_xMn_2O_4$ the reaction proceeds in two phases with the coexistence of a cubic $Li_{1.0}Mn_2O_4$-phase and a tetragonal $Li_{2.0}Mn_2O_4$-phase with a *ca*. 5.6% expansion in unit cell [1]. As lithium ions intercalate/ deintercalate the $Li_xMn_2O_4$ host material, internal strains within individual $Li_xMn_2O_4$ particles are induced due to inhomogeneous volume expansion/contraction. These internal strains may lead to dislocations, microcracks [5-6] and electrically isolated particle networks [7] leading to loss in energy capacity; nevertheless this is still a subject of debate.

Atomic force microscopy (AFM) has been often used to probe surface morphological change on Li-ion electroactive species. The solid electrolyte interphase (SEI) that forms from the reductive decomposition of the electrolyte during the initial few charge/discharge cycles tend to

have a direct influence on the initial capacity loss and storage life of Li-ion batteries. Therefore, a number of studies have used AFM to study the formation of the SEI [8-11]. Using AFM on carbon-based anodes has found that different solvents produce SEI layers with different surface morphologies [12], that electrolyte additives could produce more stable SEI layers [11], and that the SEI formation process takes in successive stages as a function of the negative electrode potential [13]. AFM has also been used to observe a linear reversible volume expansion of up to 204% in an amorphous tin-based thin-film anode [14]. AFM also has been utilized to study the positive electrode surface morphological changes. For the thin film V_2O_5 positive electrode, flattening of the electrode surface was observed with increasing numbers of cycles using *in situ* AFM [15]. In this study, it was concluded these irreversible surface modifications may correspond to the initial fatigue induced by multiple Li^+ ion intercalation/deintercalation. For particle $LiCoO_2$ positive electrodes on gold foil a dimensional change of *ca*. 1.7% was observed along the c_{hex} axis in an individual $LiCoO_2$ crystal [16]. With *in situ* AFM, one study observed small bar shaped textures appeared and disappeared on the surface of the $LiMn_2O_4$ electrode as bias potential sweep was applied [16]. Similarly, using *in situ* AFM, another study revealed that both cycling between 3.50 and 4.30 V at elevated temperature and storing the electrode at 75% depth of discharge (DOD) produced small round-shaped particles about 20 nm on the entire $LiMn_2O_4$ thin film surface [17]. However, the nature of the surface particles on $LiMn_2O_4$ electrodes is not fully understood in the above studies.

In this study, the intercalation-induced stress influence on Li^+ diffusivity is investigated both experimentally and numerically. First, the volume changes of individual $Li_xMn_2O_4$ particles during lithium intercalation/deintercalation are measured with *in situ* AFM. The volume change formation may be used in estimating the intercalation-induced stress. Lattice strain

measurements of $Li_xMn_2O_4$ as a function of Li^+ concentration are available in the literature. However, the volumetric strain as a function SOC at the particle level may be quite different because the volumetric strain is slowly initiated from the surface, particles consist of multiple crystals with crystallographic defects, and geometrical constraints may exist due to the particle shape irregularity. Moreover, as the intercalation-induced stress depends on Li^+ concentration distributions within particles, the stress level will also depend on the particle size and shape [18]. Although intercalation-induced stress could lead to fracturing of particles, the stress gradient could also enhance Li^+ diffusivity if the stress is below the material yield stress (discussed in Chapter 2). Hence, in the second part of this study, the influence of intercalation-induced stress on Li^+ diffusivity is quantified based on a modified galvanostatic intermittent titration technique (GITT). Objectives in this study are as follow:

1. Measure surface morphological change and volume expansion of $LiMn_2O_4$ particles with *in-situ* AFM while performing cyclic voltammetry technique
2. Quantify the intercalation-induced stress field contribution on Li^+ diffusivity with a modified galvanostatic intermittent titration technique (GITT)

METHODS

Sample Preparation for In-Situ AFM Experiment

To isolate the intrinsic properties of $Li_xMn_2O_4$ crystals, neither binder nor carbon additives were used in this AFM study. $Li_xMn_2O_4$ electrodes prepared for the *in situ* AFM experiments consisted of ultrasonically dispersed $Li_xMn_2O_4$ particles pressed onto a gold substrate. The following samples were prepared to observe the volume change of $Li_xMn_2O_4$ particles. First the particles and small pieces of gold foil (99.99%, Sigma-Aldrich) were added to

a beaker of methanol solution. The beaker was then placed in a sonication bath for 30 minutes to disperse particles. Finally the methanol solution was evaporated at room temperature so that only dispersed particles on the gold foil were left behind. To establish a firm contact between particles and the gold foil a compressive force was applied using an Instron Compression machine.

In-Situ AFM Measurements

Characterization of $LiMn_2O_4$ particle surface morphological change was performed with a Bruker-Nano Multimode AFM coupled with a Nanoscope IIIa controller and a BioLogic VMP3 battery cycler. The entire AFM system was placed inside an argon-filled glovebox. The AFM has the maximum scannable height of 5 μm in the z-direction and the field of view of 100 μm × 100 μm area. To scan particle morphologies immersed in an electrolyte, an AFM fluid (MMTMEC, Bruker-Nano) cell was used. The AFM fluid cell in a special type of cell used to scan and cycle particles simultaneously inside the AFM. The AFM fluid cell and its schematic diagram are shown in Fig. 3.1. The AFM fluid cell sits on top of the sample and the sealing of the electrolyte is accomplished by a capillary effect between the AFM fluid cell and the sample substrate. The lithium metal is placed around the circular groove inside the AFM fluid cell. An electrolyte is injected from the right inlet port and a copper wire that connects to the lithium metal is fed from the left inlet; the middle inlet port is left unused here. An electrolyte of 1.2 M $LiPF_6$ (Sigma-Aldrich) salt in etheylene carbonate (EC, 99.9% Fluka) : propylene carbonate (PC, 99.9% Fluka) (1:1 v/v) solvent was used. Moreover, lithium metal lithium metal (Alfa-Aesar) was used as the counter electrode. The AFM fluid cell was assembled inside a MBraun glovebox filled with argon gas (O_2, H_2O < 1ppm). All AFM images were collected in a contact mode with an AFM tip (Bruker Probes, SNL-10) that has a radius curvature of about 2 nm and a stiffness of about 0.2

N/m. While scanning the particle surface, a cyclic voltammetry (CV) test with a potential window between 2.8 V and 4.3 V vs Li/Li^+ was applied.

Quantification of Li^+ Diffusivity Enhancement by Intercalation-Induced Stress Field

The chemical potential gradient is the driving force for the movement of lithium ions. The species flux in terms of the chemical potential gradient can be written as:

$$\mathbf{J} = -Mc\nabla\mu \tag{1}$$

where **J** is the species flux, M is the lithium ion mobility, c is the concentration of lithium ions, and μ is the chemical potential. The electrochemical potential in a solid solution can be expressed as

$$\mu = \mu_0 + RT\ln\gamma x - \Omega\sigma_h . \tag{2}$$

where μ_0 is the chemical potential at the reference state, R is gas constant, T is absolute temperature, γ is the activity coefficient, x is the molar fraction of lithium ions, Ω is partial molar volume of lithium ion, and σ_h is the hydrostatic stress. In this study, we assumed active materials are spherical. The hydrostatic stress for spheres is given in Eq. 3

$$\sigma_h = \left(\sigma_r + 2\sigma_t\right)/3 = \frac{2\Omega E}{9\left(1-\nu\right)}\left(\frac{3}{r_0^3}\int_0^{r_0}\tilde{c}r^2dr - \tilde{c}\right), \tag{3}$$

where σ_r is radial stress and σ_t is tangential stress component. Moreover, E is Young's modulus, ν is Poisson's ratio, r_0 is particle radius, and $\tilde{c}$ is the concentration change of the diffusion species from the original (stress-free) value. Material properties of $LiMn_2O_4$ are given in Table 3.1. Substituting Eq. 2 and 3 into 1 yields the following expression for the species flux

$$\mathbf{J} = -D_{sd}^{Li}\left\{\left(\frac{\partial\ln\gamma}{\partial\ln x}+1\right)+c\frac{\Omega}{RT}\frac{2\Omega E}{9\left(1-\nu\right)}\right\}\frac{\partial c}{\partial r} . \tag{4}$$

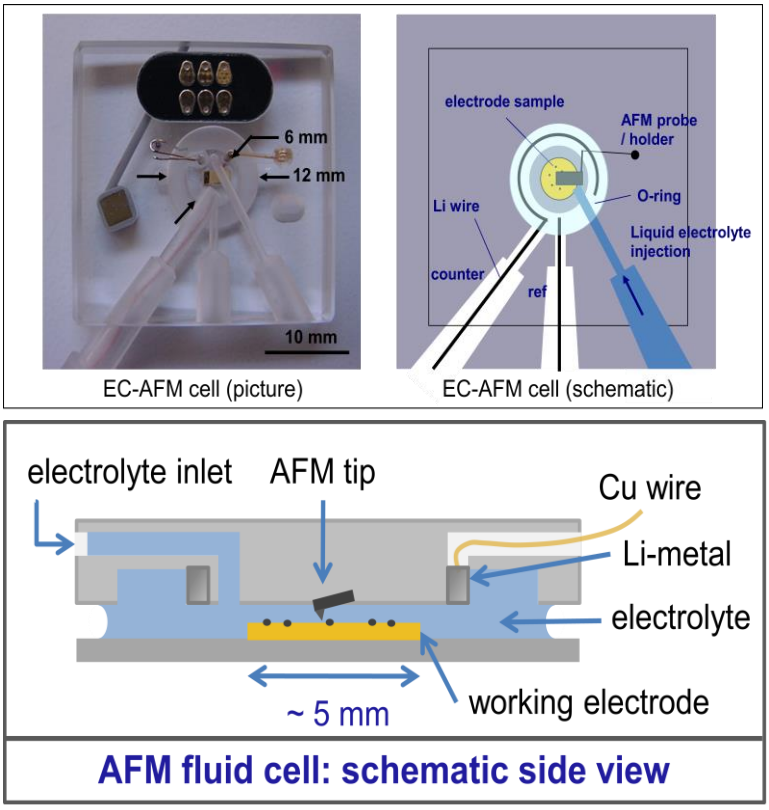

Figure 3.1: AFM fluid cell used in *in-situ* AFM experiment.

where D_{sd} is the self-diffusion coefficient. Assuming that the concentration c does not change significantly during an operation of the battery, Eq. 4 can be approximated as follows:

$$\mathbf{J} = -D_{sd}^{Li}\left\{\left(\frac{\partial \ln \gamma}{\partial \ln x}+1\right)+\bar{c}\,\frac{\Omega}{RT}\,\frac{2\Omega E}{9(1-\nu)}\right\}\frac{\partial c}{\partial r} = -D_{app}^{Li}\,\frac{\partial c}{\partial r}. \qquad (5)$$

The only difference between Eq. 4 and 5 is that inside the curly bracket, the concentration c is replaced with the average concentration $\tilde{c}$ concentration. Justification for this approximation is given in results section. The first term in the curly bracket is the thermodynamic factor that accounts for the ionic-to-ionic interactions and the second term is the intercalation-induced stress field contribution on the species flux. The thermodynamic factor may be calculated from the open-circuit potential curve. The open-circuit potential of $LiMn_2O_4$ is determined experimentally with approximately slow C/50 C-rate. In the stress field contribution term, the average concentration $\tilde{c}$ is also experimentally obtained for each constant current titration step during the GITT method. In the GITT method, a constant current rate of approximately C/10 was applied for 5 minutes. In the right hand side of Eq. 5, D_{app} is the apparent diffusion coefficient determined experimentally from the standard GITT method [19].

RESULTS

Electrochemical Behavior

Fig. 3.2 shows a cyclic voltammetry result from the AFM fluid cell. Typically $LiMn_2O_4$ has two sharp cathodic and anodic peaks around 4.1 V and 4.0 V, respectively. Instead two cathodic peaks appear around 4.25 V and 4.8 V and anodic peaks appear around 3.4 V and 3.7 V. In a coin-cell only 3~6 drops of electrolyte are used whereas in the fluid cell a much larger amount of electrolyte is used to fill the fluid cell. In addition, the distance between the cathode

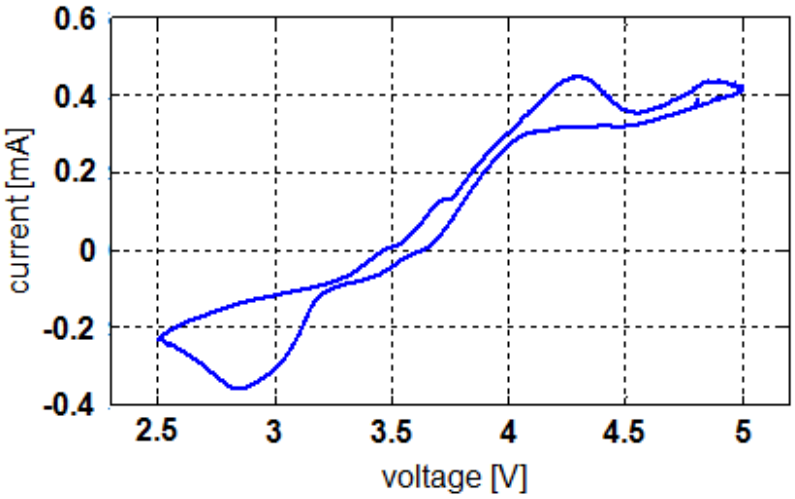

Figure 3.2: Cyclic voltammetry result on $LiMn_2O_4$ particles performed inside AFM fluid cell.

Symbol (unit)	Definition	Value
E (GPa)	Young's modulus	100
ν (-)	Poisson's ratio	0.3
Ω ($m^{3}{\cdot}mol^{-1}$)	partial molar volume	3.497×10^{-6} [18]
c_{max} ($mol{\cdot}m^{-3}$)	$LiMn_2O_4$ stoichiometric maximum concentration	2.29×10^{4}
F ($C{\cdot}mol^{-1}$)	Faraday's constant	96,487
T (K)	temperature	300
R ($J{\cdot}mol^{-1}{\cdot}K^{-1}$)	universal gas constant	8.314

Table 3.1: Simulation parameters related to LiMn2O4 material properties.

particles and the lithium metal anode is on the order of millimeter instead of typical tens of micrometers in normal cells. Therefore, the shift in cathodic and anodic peaks may be due to a large potential drop is expected across the electrolyte.

In-Situ AFM Scanning

Height evolution of two $LiMn_2O_4$ particles was observed by looking at their cross sections. The two *in situ* AFM scanned particles are shown in Figures 3.3 and 3.4. Although a greater number of images should had been produced to show the evolution of particle volume changes, a number of problems were encountered during the experiment. Because the AFM fluid cell is an open configuration, the electrolyte kept evaporating. Any drop in the electrolyte level could change the AFM laser reflection angle. Also a bubble may be trapped near the probe, and any contaminants suspending in the AFM fluid cell may be attracted to the probe interfering with the laser signal. In such cases the experiment needs to be stopped and recalibrated. Based on two images, the first particle had a *z*-directional strain of 10.7% in the potential range from 3.95 V to 4.15V as shown in Figure 3.3. Similarly based on three images, the second particle had a *z*-directional strain of 5.2% and 7.8% at two different cross sections in the potential range from 3.53V to 4.58V. The first and the second particle sizes are approximately 7.5 μm and 0.8 μm, respectively. The result is summarized in Table 3.2. In comparison, to the lattice strain measurements with XRD method, a single $LiMn_2O_4$ crystal undergoes about a 7.4 % volumetric strain between 3.5 V and 4.3 V.

The *z*-directional strain differences between the two particles may be due to the particle size assuming their grain sizes are similar. Nevertheless, a greater number of particles need to scanned with *in situ* AFM in order to determine their volume strains statistically. One of the limitations of the AFM setup is that only half the volume strain can be measured. Moreover, the

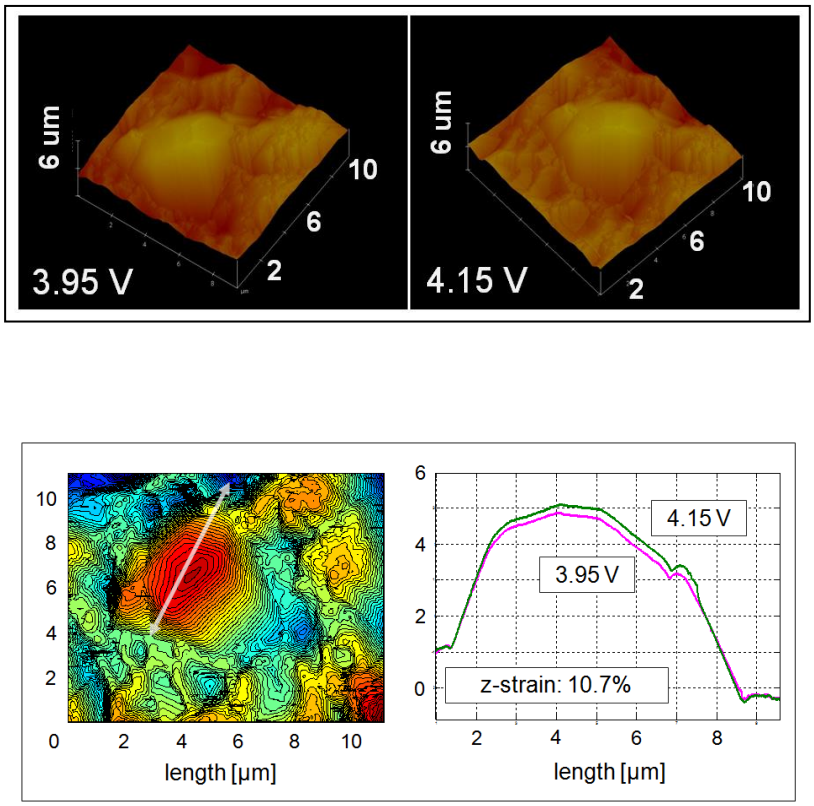

Figure 3.3: (above) The first particle in situ AFM images,
(below) cross sectional views of the first particle at different voltages

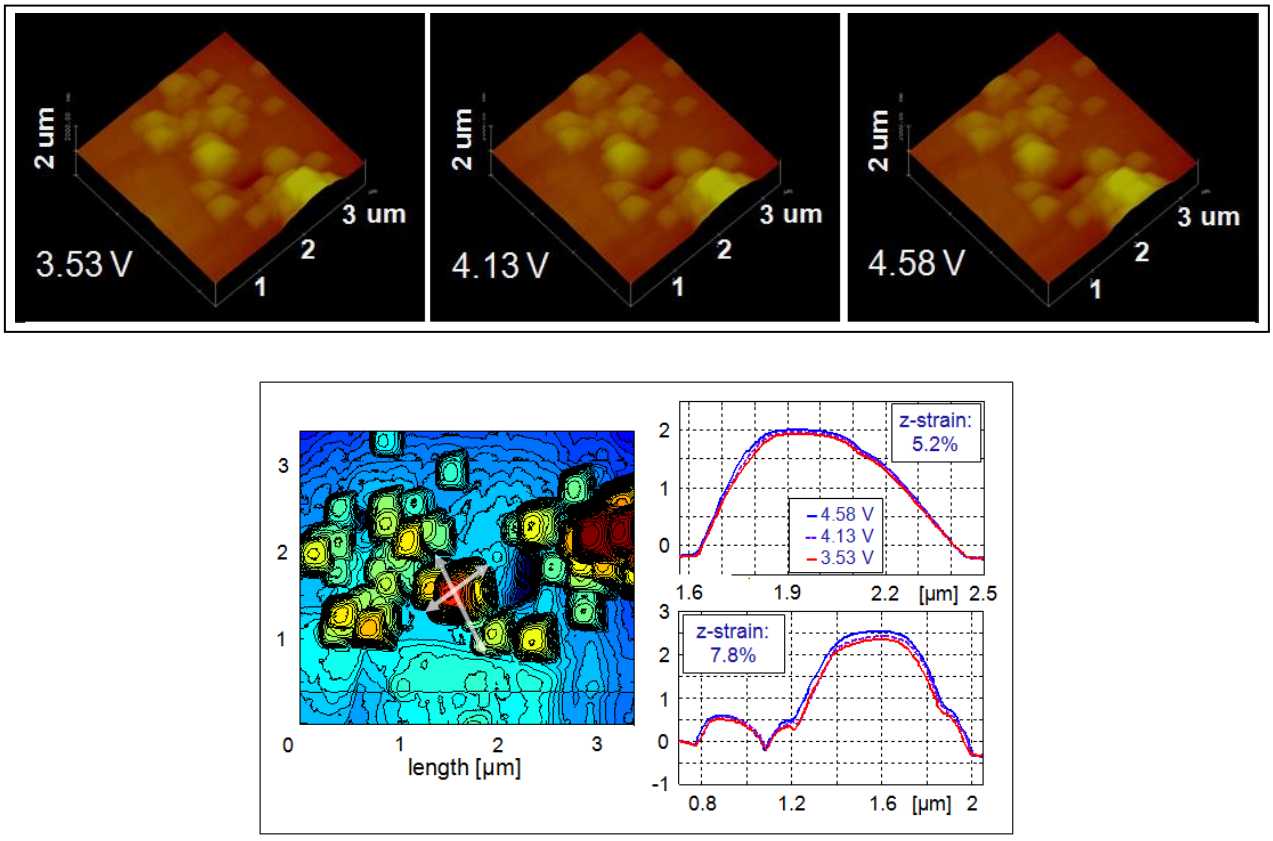

Figure 3.4: (above) The second particle in situ AFM images,
(below) cross sectional views of the particle at different voltages.

	Particle No. 1	**Particle No. 2**
Potential range [V]	3.95-4.15V	3.53-4.58V
Number of images	2	3
Approx. particle size [μm]	7.5 μm	0.8 μm
z-directional strain	10.7%	5.2% (first cross section) 7.8% (second cross section)

Table 3.2: Measured *z*-directional strains of two particles.

volume expansion of particles may be constrained by the substrate. Captured AFM images contain tilt angles in *x*-, *y*-, and *z*-directions. For example, in one-dimension, a tilted rectangular shape is a rhombus shape. In order to correct for the tilted angles in three-dimensions and analyze a complete a three-dimensional volume evolution, a reference plane or a fixed shape needs to be captured along with a particle.

Li^+ Diffusivity Enhancement by Intercalation-Induced Stress Field

To test the validity of species flux linearization in Eq. 5, lithium ion concentration profiles from the exact solution obtained using Eq. 4 and the approximated solution obtained using Eq. 5 are compared and shown in Figure 3.5. The concentration profiles are numerically determined using COMSOL Multiphysics Software. The profiles are simulated using 3 μm radius spherical particle. Initially the particle was at 20% SOC and the constant current of 5C was applied at the particle surface. Despite high current rate of 5C the approximated concentration profile did not deviate significantly from the exact concentration profile, as shown in Fig. 3.5. However, for larger current where Li^+ concentration change is significant, the linearization of species flux may become invalid.

The thermodynamic factor and the stress-field factor are obtained for each constant current titration step in the GITT method and they are shown in Figure 3.6. The thermodynamic factor peaks at about 50% SOC. This trend and the order of magnitude are similar to ones found in the literature for $LiMn_2O_4$. Unlike the maximum intercalation-induced stress which peaks at about 50% SOC, the stress factor also increases linearly with increasing lithium molar fraction in $LiMn_2O_4$. For $LiMn_2O_4$, the order of magnitude for the stress factor is about the same as the thermodynamic factor. For materials such as Si and Sn where the volume expansion/contraction is significantly higher, the stress factor may be greater than the thermodynamic factor.

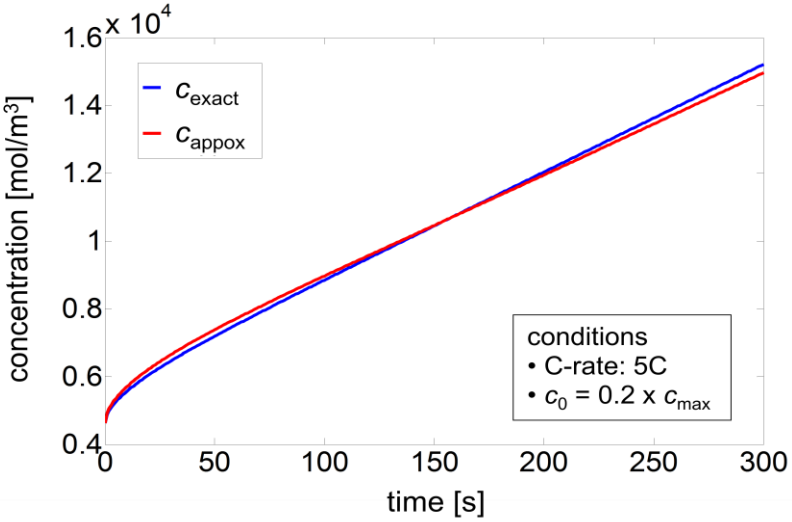

Figure 3.5: Concentration profiles comparison between exact and approximated solutions.

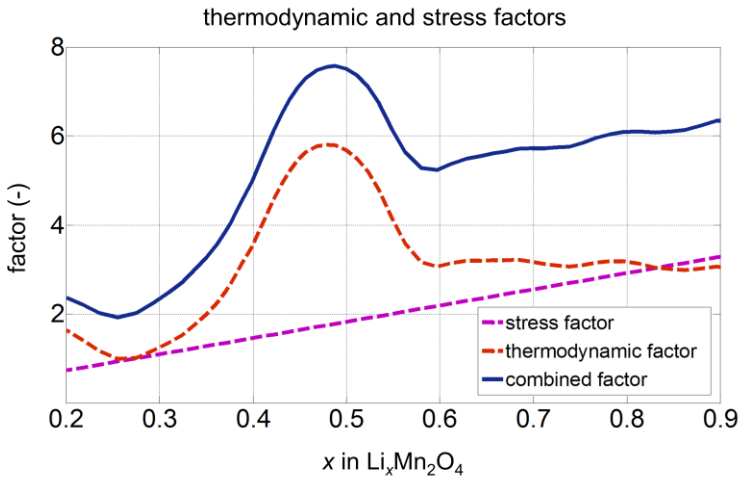

Figure 3.6: Thermodynamic and stress factors as a function of Li^+ concentration.

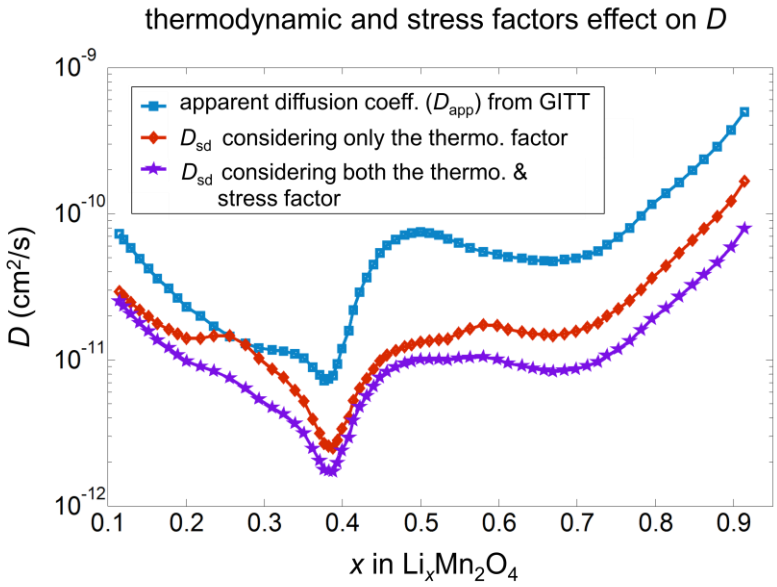

Figure 3.7: Apparent and self diffusion coefficients.

The apparent diffusion coefficients and self-diffusion coefficients as a function of lithium concentration obtained from GITT method are shown in Figure 3.7. The self-diffusion coefficient profile shown in red is where only the thermodynamic factor is considered. The self-diffusion coefficient profile shown in purple is where both the thermodynamic and stress factors are considered. As shown in Fig. 3.7, if only the thermodynamic factor is considered, one may be over-estimating the self-diffusion coefficient.

CONCLUSIONS AND FUTURE WORK

Two $LiMn_2O_4$ particles are scanned with *in situ* AFM to observe cross sectional evolutions. Based on observations of three cross sections a mean *z*-directional strain of 7.9 ± 2.8% is observed in the 3.5V~4.5V range. For future work, the strain measurements will be compared with simulation results to validate the intercalation-induced model and estimate the intercalation-induced stress induced developed inside particles.

The stress field contribution in the Li+ diffusion coefficient is approximately quantified using the modified GITT model. If only the thermodynamic factor is considered the apparent diffusion coefficient is enhanced by approximately 3.3 on average over $0.2 \leq x \leq 0.9$ range (x in $Li_xMn_2O_4$). If both the thermodynamic and the stress factor are considered, the combined effect enhances the apparent diffusion coefficient by approximately 5.3 on average over the same lithium concentration range. As future work, we want to test whether the stress factor scales linearly with the particle size. Moreover, we would want to determine the thermodynamic and stress factors in other active materials with much higher volume expansion/contraction (e.g., silicon) and compare with results from $LiMn_2O_4$.

BIBLIOGRAPHY

1. Ohzuku, T.; Kitagawa, M.; Hirai, T., Electrochemistry of manganese-dioxide in lithium nonaqueous cell .3. X-ray diffractional study on the reduction of spinel-related manganese-dioxide. *Journal of The Electrochemical Society* **1990,** *137* (3), 769-775.

2. Thackeray, M. M.; Dekock, A.; Rossouw, M. H.; Liles, D.; Bittihn, R.; Hoge, D., Spinel electrodes from the li-mn-o system for rechargeable lithium battery applications. *Journal of The Electrochemical Society* **1992,** *139* (2), 363-366.

3. Gummow, R. J.; Dekock, A.; Thackeray, M. M., Improved capacity retention in rechargeable 4v lithium lithium manganese oxide (spinel) cells. *Solid State Ion.* **1994,** *69* (1), 59-67.

4. Paulsen, J. M.; Dahn, J. R., Phase diagram of li-mn-o spinel in air. *Chem. Mat.* **1999,** *11* (11), 3065-3079.

5. Wang, D. Y.; Wu, X. D.; Wang, Z. X.; Chen, L. Q., Cracking causing cyclic instability of lifepo4 cathode material. *Journal of Power Sources* **2005,** *140* (1), 125-128.

6. Wang, H. F.; Jang, Y. I.; Huang, B. Y.; Sadoway, D. R.; Chiang, Y. T., Tem study of electrochemical cycling-induced damage and disorder in licoo2 cathodes for rechargeable lithium batteries. *J. Electrochem. Soc.* **1999,** *146* (2), 473-480.

7. Kostecki, R.; McLarnon, F., Local-probe studies of degradation of composite lini0.8co0.15al0.05o2 cathodes in high-power lithium-ion cells. *Electrochem. Solid State Lett.* **2004,** *7* (10), A380-A383.

8. Jeong, S. K.; Inaba, M.; Iriyama, Y.; Abe, T.; Ogumi, Z., Surface film formation on a graphite negative electrode in lithium-ion batteries: Afm study on the effects of co-solvents in ethylene carbonate-based solutions. *Electrochimica Acta* **2002,** *47* (12), 1975-1982.

9. Matsumura, Y.; Wang, S.; Yamaguchi, C.; Mondori, J.; Matsui, H., A study of the surface morphology of a disordered carbon electrode. *J. Power Sources* **1998,** *74* (2), 246-251.

10. Yazami, R., Surface chemistry and lithium storage capability of the graphite-lithium electrode. *Electrochim. Acta* **1999,** *45* (1-2), 87-97.

11. Matsuoka, O.; Hiwara, A.; Omi, T.; Toriida, M.; Hayashi, T.; Tanaka, C.; Saito, Y.; Ishida, T.; Tan, H.; Ono, S. S.; Yamamoto, S., Ultra-thin passivating film induced by vinylene carbonate on highly oriented pyrolytic graphite negative electrode in lithium-ion cell. *J. Power Sources* **2002,** *108* (1-2), 128-138.

12. Inaba, M.; Siroma, Z.; Kawatate, Y.; Funbiki, A.; Ogumi, Z., Electrochemical scanning tunneling microscopy analysis of the surface reactions on graphite basal plane in ethylene carbonate-based solvents and propylene carbonate. *J. Power Sources* **1997,** *68* (2), 221-226.

13. Leroy, S.; Blanchard, F.; Dedryvere, R.; Martinez, H.; Carre, B.; Lemordant, D.; Gonbeau, D., Surface film formation on a graphite electrode in li-ion batteries: Afm and xps study. *Surf. Interface Anal.* **2005,** *37* (10), 773-781.

14. Tian, Y.; Timmons, A.; Dahn, J. R., In situ afm measurements of the expansion of nanostructured sn-co-c films reacting with lithium. *Journal of The Electrochemical Society* **2009,** *156* (3), A187-A191.

15. Swiatowska-Mrowlecka, J.; Maurice, V.; Klein, L.; Marcus, P., Nanostructural modifications of v2o5 thin films during li intercalation studied in situ by afm. *Electrochem. Commun.* **2007,** *9* (9), 2448-2455.

16. Kuriyama, K.; Onoue, A.; Yuasa, Y.; Kushida, K., Atomic force microscopy study of surface morphology change in spinel limn2o4: Possibility of direct observation of jahn-teller instability. *Surf. Sci.* **2007,** *601* (10), 2256-2259.

17. Doi, T.; Inaba, M.; Tsuchiya, H.; Jeong, S. K.; Iriyama, Y.; Abe, T.; Ogumi, Z., Electrochemical afm study of limn2o4 thin film electrodes exposed to elevated temperatures. *J. Power Sources* **2008,** *180* (1), 539-545.

18. Zhang, X.; Shyy, W.; Sastry, A. M., Numerical simulation of intercalation-induced stress in li-ion battery electrode particles. *J. Electrochem. Soc.* **2007,** *154* (10), A910-A916.

19. Wen, C. J.; Boukamp, B. A.; Huggins, R. A.; Weppner, W., Thermodynamic and mass-transport properties of lial. *J. Electrochem. Soc.* **1979,** *126* (12), 2258-2266.

CHAPTER IV

A SENSITIVITY STUDY OF TRANSPORT AND KINETIC MATERIAL PROPERTIES ON CELL ELECTROCHEMICAL BEHAVIOR

INTRODUCTION

A lithium-ion (Li-ion) cell is often allowed to operate within a fixed state-of-charge (SOC) range or a potential window to minimize its capacity degradation. Despite the effort the cell capacity degradation is inevitable. When degradation occurs, not only cell capacity decreases but also an individual electrode operating potential window may shift with respect to a reference electrode, further altering the cell electrochemical response. The cell operating temperature also has a significant influence on the electrochemical behavior. Generally, when the cell temperature is about 50 °C or higher capacity degradation mechanisms accelerate and when the temperature is about −20 °C or lower the cell performance significantly deteriorates due to increased activation losses associated with cell material properties. Hence, to accurately predict a cell electrochemical behavior, thermodynamic, kinetic, and transport material properties need to be measured as a function of both lithium ion (Li^+) concentration, c, and temperature, T. However, measured cell material properties always have associated uncertainties, and some may change with time due to various chemical and mechanical degradation mechanisms.

The cell open circuit potential (OCP) is determined by the thermodynamic properties of the positive and the negative electrodes. During cycles, however, the actual cell potential profile will deviate from the cell OCP due to polarization, or losses. This polarization can be classified

into three types – (i) activation, (ii) concentration, and (iii) ohmic. The activation polarization describes the loss associated with the charge transfer kinetics during an electrochemical reaction. The concentration polarization is the loss associated with the diffusive mass transport limitations. Lastly, the ohmic polarization represents the potential drop due to electronic and ionic resistivity in the electrodes and electrolyte, respectively. The potential loss will not only depend on material properties which are dependent on SOC and temperature, but also on cell loading conditions because different types of potential losses occur on different timescales. For example, the potential drop due to an ohmic loss will occur instantaneously, whereas the potential drop due to diffusive mass transport limitations will span over a longer period.

In a cell, various phenomena occur in sequence. For instance, during discharge lithium ions deintercalate from anode by an electrochemical reaction process, move across the electrolyte by both diffusive and migratory modes of transport, and finally intercalate and diffuse into cathode. In this simplified process, the slowest process will evidently determine the cell rate capability. Because cell material properties may change with cell degradation, state-of-charge, temperature, and the loading conditions, the slowest process could also change depending on the overall operating environment.

In this chapter, the sensitivity of various cell transport and kinetic material properties on the electrochemical behavior is investigated using an electrochemical (P2D) model. The sensitivity is performed using an isothermal electrochemical pseudo-2-dimension (P2D) model to simplify the analysis. The model is then modified to become temperature-dependent, and it is utilized to estimate material properties of a commercial LG Chem P1.4 prismatic cell. Finally, once the cell input parameters are calibrated against the experimental cell data, potential losses

associated with various transport and kinetic parameters are computed in order to determine the rate-limiting factor at a given temperature level. The objectives are threefold:

1. Perform a sensitivity analysis of various transport and kinetic cell parameters with an isothermal electrochemical P2D cell model
2. Based on the sensitivity study finding, estimate material properties of a commercial LG Chem P1.4 cell cycled at +25 °C
3. Quantify potential losses associated with transport, kinetic, and ohmic parameters and identify rate-limiting parameters at various temperatures

METHODS

To assess the sensitivity of predictions to transport and kinetic cell parameters, an isothermal-electrochemical pseudo-2-dimensional (IEC-P2D) model is utilized. After the assessment, the model is modified to include temperature-dependence and used in estimating internal cell material properties of an LG Chem P1.4 experimental cell. The following describes the governing equations in the Li-ion cell model.

Isothermal-Electrochemical Pseudo-2-Dimensional Model

The physics-based electrochemical P2D model solves the potentials based on the conservation of charge. The charge conservation in the electrodes and the electrolyte is described in Eq. 1 and Eq. 2, respectively.

$$\nabla \cdot \left(-\sigma_s^{eff} \nabla \Phi_s \right) + j = 0 \tag{1}$$

$$\nabla \cdot \left\{ \kappa_e^{eff} \left[\nabla \Phi_e - \frac{2RT}{F} \left(1 + \frac{d \ln f_{\pm}}{d \ln c_e} \right) \left(1 - t_+ \right) \nabla \ln c_e \right] \right\} + j = 0 . \tag{2}$$

The porosity influence on material properties is accounted for with Bruggeman relationship shown in Eq. 3,

$$\lambda^{eff} = \lambda \varepsilon^{\gamma} \tag{3}$$

where λ may take on any material property, ε is the volume fraction of the material, and γ is Bruggeman constant. Based on the conservation of mass, the lithium ion concentration within a spherical active material particle as well as the electrolyte phase is computed with Eq. 4 and Eq. 5, respectively.

$$\frac{\partial c_s}{\partial t} + \frac{1}{r^2}\nabla\left(-r^2 D_s \nabla c_s\right) = 0 \tag{4}$$

$$\varepsilon_e \frac{\partial c_e}{\partial t} + \left[\nabla \cdot \left(-D_e^{eff} \nabla c_e\right) - \frac{j}{F}\left(1 - t_+\right)\right] = 0 . \tag{5}$$

The charge transfer at the electrode-electrolyte interface is governed by the Butler-Volmer electrochemical reaction kinetics shown in Eq. 6.

$$i = i_0 \left\{ \exp\left(\frac{\beta F}{RT}\eta\right) - \exp\left[\frac{(1-\beta)F}{RT}\eta\right]\right\}. \tag{6}$$

The surface or kinetic overpotential, η, and the exchange current density, i_0, in Eq. 6 are

$$i_0 = Fk\left(c_s\right)^{\beta}\left(c_e\right)^{\beta}\left(c_{s,\max} - c_{s,surf}\right)^{1-\beta}, \tag{7}$$

$$\eta = \Phi_s - \Phi_e - U\left(c_s / c_{s,\max}\right). \tag{8}$$

The specific surface area, S_a, relates the current density, i, used in Eq. 6 and the local volumetric current density, j, used in Equations 1 and 2,

$$j = S_a i \,. \tag{9}$$

Thermal Modeling

To include temperature dependence to the isothermal model, the following heat equation is added to the isothermal model:

$$\rho C_{p,k} \frac{dT}{dt} = K_k \nabla^2 T + q \,. \tag{10}$$

The subscript *k* represents two electrodes and electrolyte phases in a cell. Neglecting the heat due to enthalpy of mixing and phase transformation in electrodes, the heat generation per unit volume, *q*, is expressed as[1]:

$$q = \sum_k j\left(\Phi_s - \Phi_e - U_k\right) + \sum_k jT \frac{\partial U_k}{\partial T} + \sigma_s^{eff} \nabla\Phi_s \cdot \nabla\Phi_s + \kappa_s^{eff} \nabla\Phi_e \cdot \nabla\Phi_e + \kappa_s^{eff} \nabla \ln c_e \cdot \nabla\Phi_e \,. \tag{11}$$

In Eq. 11, the first term on the right represents the irreversible heat due to the electrochemical reaction at two electrode-electrolyte interfaces. The second term on the right is the reversible heat arising from the entropy changes in the electrodes. The third term represents the ohmic heat from the electrode, and the fourth and fifth terms represent the ohmic heat associated with migratory and diffusive transport of lithium ions in the electrolyte phase, respectively. The boundary condition applied at two ends of cell is

$$-K_j \nabla T = h\left(T - T_{env}\right) \,. \tag{12}$$

The open circuit potential (OCP) of an individual active material as a function of temperature is shown in Eq. 13.

$$U_i = U_{i,ref} + \frac{\Delta s}{zF}\left(T - T_{ref}\right) = U_{i,ref} + \left(\frac{dU}{dT}\right)_p \left(T - T_{ref}\right). \quad (13)$$

LG Chem P1.4 cell is made up of three different types of active materials, namely $LiMn_2O_4$ (LMO) and $LiNi_{1/3}Mn_{1/3}Co_{1/3}O_2$ (NMC) for cathode and graphite (Li_xC_6) for anode. The changes in the open circuit potential with respect to temperature under a constant pressure at a given state-of-charge (SOC) for LMO [2], and NMC [3], and graphite [4] are obtained from the literature. As for the electrolyte, it is speculated that additive-enhanced gel-type or carbonate-based solvents containing $LiPF_6$ salts is used. With this assumption, ranges of cell transport and kinetic material properties found in the literature are summarized in Table 4.1. Due to a limited availability of experimentally measured reaction rate constants in the literature, the corresponding ranges come from a pool of values used in simulations and approximations from Tafel plots found in the literature. Table 4.1 also contains fixed cell dimensional and thermal parameters used in the simulation. In regards to thermal properties, the specific heat capacity of the whole cell is obtained by adiabatic caloriemeter experiments, whereas the heat transfer coefficient is approximated from the temperature cooling profile. Densities and planar thermal conductivities of different phases are obtained from the literature.

Assuming transport and kinetic material properties follow an Arrhenius-type temperature-dependent relationship the associated thermal activation energy for different properties are listed in Table 4.2. Cathode Li^+ diffusivity measurements as a function of temperature are very limited in the literature. Nonetheless they are assumed to follow an Arrhenius-type relationship and the associated activation energy is estimated based on the graphite activation energy level. Although the electronic conductivity of graphite and the transference number would change with temperature, they are assumed as constants here based

on the following assumption – the graphite electronic conductivity is quite high regardless of temperature variations [5] and the Li^+ transference is a weak function of temperature [6]. Assuming they are not rate limiting factors even in low temperature, constant values are used.

Parameter Sensitivity Study

The sensitivity of the transport and kinetic input cell parameters on the model prediction is investigated with the isothermal-electrochemical half-cell model. Parameters and their ranges used in the sensitivity are shown in Table 4.3. Each variable is set to either low or high value one at a time while the rest of parameters are set to their baseline values. With one additional run with all five parameters set to their baseline values, a total of 11 simulation cases are performed. In each run, the cell is discharged from a fully charged state to a cutoff potential of 2.5 V with C/1-rate followed by a current relaxation. After each simulation run, the following are quantified: (i) the initial voltage, (ii) the time for the average concentration gradient in the electrolyte phase to reach a quasi steady state once discharging starts, (iii) cell capacity utilized, (iv) the time for the recovery potential to reach an equilibrium state, and (v) the recovery potential. The average concentration gradient change across the cell thickness at a specific point in time, t_i, is computed using Eq. 14.

$$\frac{\partial c_{e,avg}}{\partial t_i} = \frac{1}{L_{cell}} \int_{Lcell} \frac{\partial c_e}{\partial t_i} dx \,. \tag{14}$$

It is arbitrarily defined here that the gradient change in the electrolyte has reached a quasi steady state when the term on the right in Eq. 14 has reached 5×10^{-3} $mol \cdot m^{-3} \cdot s^{-1}$ or less. Moreover, in this study, it is assumed that the recovery potential reached an equilibrium when the recovery potential change is equal to or less than 1 $\mu V \cdot s^{-1}$.

Symbol	definition	unit	anode	electrolyte	cathode
D_s	Li^+ diffusion coefficient	$m^2 \cdot s^{-1}$	10^{-15}~10^{-11} [7-10]	–	10^{-16}~10^{-12} [11-16]
σ_s	$LiMn_2O_4$ electronic conductivity	$S \cdot m^{-1}$	100	–	10^{-4}~10^{0} [17-20]
k	reaction rate constant	$m^{2.5} \cdot mol^{-0.5} \cdot s^{-1}$	10^{-13}~10^{-9} [21-26]	–	10^{-13}~10^{-9} [21-26]
β	symmetry factor	–	0.5	–	0.5
D_e	electrolyte diffusion coefficient	$m^2 \cdot s^{-1}$	–	$(1\text{~}10) \times f_1(c_e)$ [6, 27-29]	–
κ_e	electrolyte ionic conductivity	$S \cdot m^{-1}$	–	$(0.1\text{~}1.5) \times f_2(c_e)$ [6, 29]	–
t_+	transference number	–	–	0.25~0.75[6, 30-32]	–
$1+ \ln f_\pm / d\ln c_e$	mean molar activity function	–	–	$f_3(c_e)$ [32]	–
ρ	average density	$kg \cdot m^{-3}$	1350 [33]	1100 [33]	1300 [33]
C_p	specific heat capacity	$J \cdot kg^{-1} \cdot K^{-1}$		1040 for all	
K	planar thermal conductivity	$W \cdot m^{-1} \cdot K^{-1}$	1 [33]	0.3 [33]	1.5 [33]
h	heat transfer coefficient	$W \cdot m^{-2} \cdot K^{-1}$		20 for all [33]	
ε_s	solid phase vol. fraction	–	0.6073	0.2900	0.5621
ε_f	filler vol. fraction	–	0.1777	–	0.1529
r_p	particle radius	µm	8	–	7.5
γ	Bruggeman constant	–		1.53 for all	
L	thickness	µm	50	25	57
A_{cell}	prismatic cell cross-sec. area	m^2		0.0285 for all	

$$f_1(c_e) = 10^{-10} \cdot \exp\left(-\frac{0.7 c_e}{1000}\right) \tag{15}$$

$$f_2(c_e) = 0.1 + 1.134\left(\frac{c_e}{1000}\right) \Big/ \left(1 + 0.2\left(\frac{c_e}{1000}\right) + 0.08\left(\frac{c_e}{1000}\right)^4\right) \tag{16}$$

$$f_3(c_e) = 1 + c_e\left[\frac{-1.0178}{21 + 0.9831\sqrt{c_e}}\left(\frac{1}{\sqrt{c_e}} - \frac{0.9831}{1 + 0.9831\sqrt{c_e}}\right) + 1.5842\right] \tag{17}$$

Table 4.1: Ranges of transport and kinetic parameters as well as fixed thermal and dimensional parameters.

Symbol	Definition	Unit	Activation energy, E_a (kJ/mol)	Ref.
D_{pos}	Li^+ diffusion coeff. − $LiMn_2O_4$	$m^{2}{\cdot}s^{-1}$	~40	assumed
D_{neg}	Li^+ diffusion coefficient − graphite	$m^{2}{\cdot}s^{-1}$	~40	assumed
σ_{pos}	electronic conductivity −	$S{\cdot}m^{-1}$	40~60	17, 19-20, 34
σ_{neg}	electronic conductivity −	$S{\cdot}m^{-1}$	n/a	-
k_{pos}	reaction rate constant − cathode side	$m^{2.5}{\cdot}mol^{-0.5}{\cdot}s^{-1}$	~50	34-36
k_{neg}	reaction rate constant − anode side	$m^{2.5}{\cdot}mol^{-0.5}{\cdot}s^{-1}$	50~67	37-38
κ_e	electrolyte Li^+ ionic conductivity	$S{\cdot}m^{-1}$	~20	6
D_e	electrolyte diffusion coefficient	$m^{2}{\cdot}s^{-1}$	~15	6
$d\ln f_{\pm}/d\ln c_e$	mean molar activity coefficient	−	~5	6
t_{plus}	transference number	−	n/a	-

Table 4.2: Thermal activation energy associated with each transport and kinetic material properties.

Symbol	Definition	Unit	Low	Baseline	High
D_{pos}	active material diffusion coeff.	$m^{2}{\cdot}s^{-1}$	1×10^{-14}	1×10^{-13}	1×10^{-12}
σ_{pos}	electronic conductivity	$S{\cdot}m^{-1}$	0.1	1	10
k_{pos}	reaction rate constant	$m^{2.5}{\cdot}mol^{-0.5}{\cdot}s^{-1}$	1×10^{-13}	1×10^{-11}	1×10^{-9}
κ_e	electrolyte Li^+ ionic conductivity	$S{\cdot}m^{-1}$	$1 \times f_1(c_e)$	$5 \times f_1(c_e)$	$10 \times f_1(c_e)$
D_e	electrolyte diffusion coefficient	$m^{2}{\cdot}s^{-1}$	$0.10 \times f_2(c_e)$	$0.84 \times f_2(c_e)$	$1.50 \times f_2(c_e)$

Table 4.3: A design of experiment table for the isothermal EC-P2D sensitivity study.

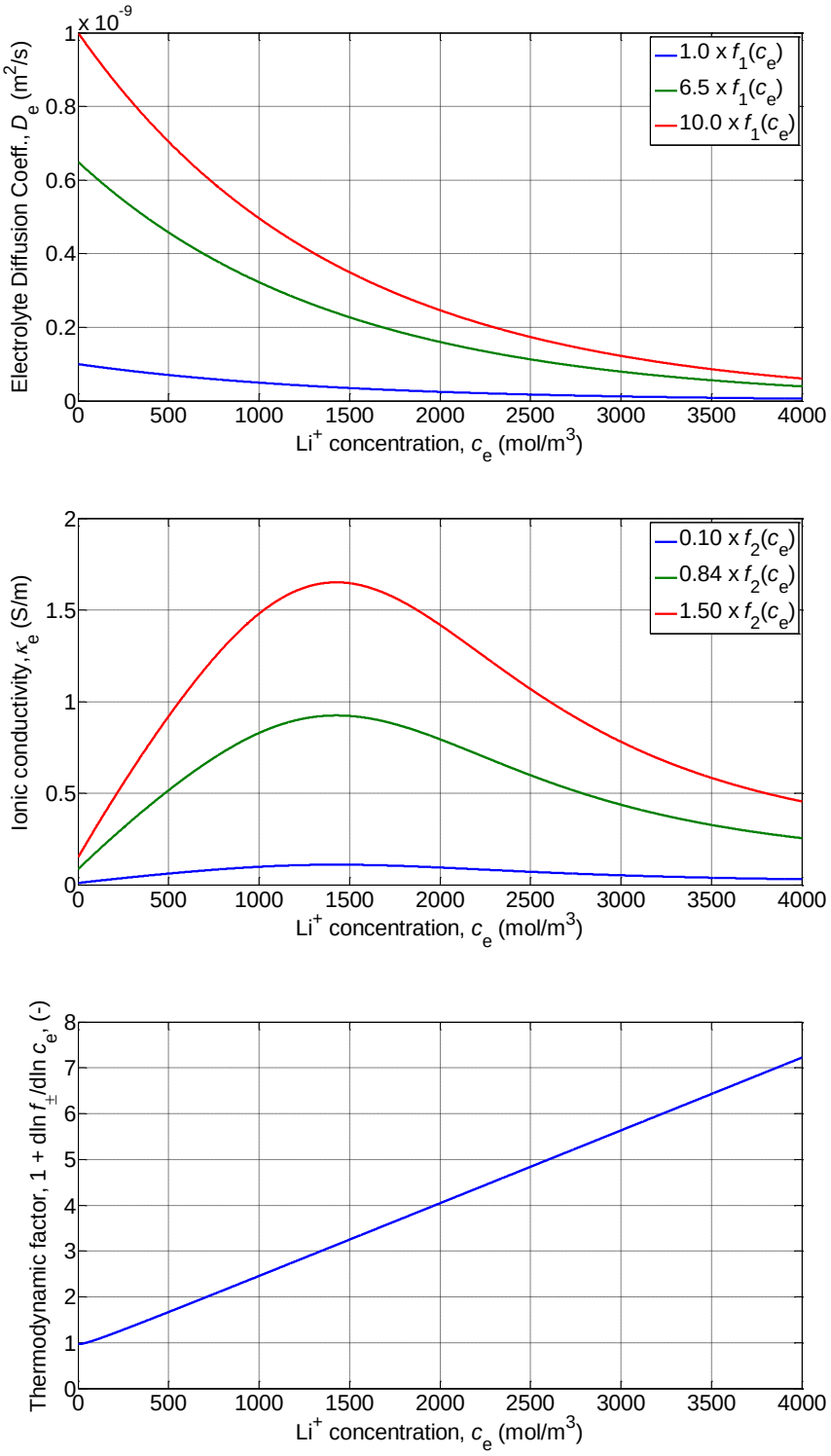

Figure 4.1: Transport and kinetic properties that are a function of Li^+ concentration, c_e: (top) electrolyte Li^+ diffusion coefficient, D_e, (middle) electrolyte ionic conductivity, κ_e, (bottom) thermodynamic factor of the electrolyte, $f_\pm$.

RESULTS AND DISCUSSION

Sensitivity Study

The sensitivity of the electronic conductivity, σ_{pos}, on 1C constant current discharge profile is shown in Fig. 4.2. When the electronic conductivity is lowered by an order of magnitude from 10 to 1 $S \cdot m^{-1}$ and from 1 to 0.1 $S \cdot m^{-1}$ the entire discharge profile shifts downward by about 0.6 mV and 6.0 mV, respectively. Although not shown in Fig. 4.2, if the conductivity is further reduced from 0.1 to 0.01 $S \cdot m^{-1}$ the entire discharge profile shifts downward by about 60.0 mV. Hence, the electronic conductivity and the cell potential are inversely proportional as expected according to Ohm's law. Based on this simple sensitivity test, as long as the electronic conductivity is higher than 0.1 $S \cdot m^{-1}$, it would not have a significant influence on the cell performance. The Li^+ ionic conductivity, κ_e, in the electrolyte phase has a similar effect as the electronic conductivity and the result is shown in Fig. 4.3. If κ_e is lowered from 1.5 × $f_2(c_e)$ to 0.84 × $f_2(c_e)$ and from 0.84 × $f_2(c_e)$ to 0.10 × $f_2(c_e)$ the entire discharge profile shifts downward again by about 4.0 mV and 70 mV, respectively. Although the ionic conductivity and potential should follow Ohm's law, the downward shift is not exactly linear because the ionic conductivity is a function of Li^+ concentration.

The potential consumed in the electrochemical reaction is equal to the surface overpotential, η, in the Butler-Volmer equation in Eq. 6. For $\beta = 0.5$, the potential loss due to the reaction rate constant can be computed directly by solving the Butler-Volmer equation in terms of η as shown in Eq. 18 [39].

$$\eta = \frac{2RT}{F} \ln\left\{ \frac{j}{2i_0} + \left[\left(\frac{j}{2i_0} \right)^2 + 1 \right]^{1/2} \right\}, \tag{18}$$

The potential loss for different reaction rate constants is shown in Fig. 4.4. As shown in Fig. 4.4, the reaction rate constant acts as an effective ohmic loss up to about 50 % SOC; it then increases in the lower SOC range. This is because the exchange current density, i_0, is inversely proportional to the lithium ion surface concentration. Physically, a higher potential would be required to insert lithium ions into a particle with a higher Li^+ concentration. The charge transfer resistance measured with an electrochemical impedance spectroscopy (EIS) method also shows a rising trend towards the end-of-discharge [40]. The ohmic behavior of the reaction rate constant can also be observed from discharge profiles shown in Fig. 4.5. With decreasing reaction rate constant, the entire discharge profile shifts downward. Because the reaction rate constant acts as an ohmic term, an ohmic resistance associated with the SEI layer may be incorporated into the reaction rate constant, making it the effective reaction rate constant.

When a cell is discharged, a lithium ion concentration gradient starts to develop within the electrolyte phase. Lower Li^+ diffusivity would create a higher Li^+ concentration gradient and this will lead to a higher potential drop across the electrolyte phase. However, the concentration gradient is developed over time because lithium ions need to diffuse across the electrolyte thickness. Hence, unlike the conductive terms, the potential loss occurs over a period of time. Moreover, due to the associated timescale to reflect on the discharge potential profile, the electrolyte Li^+ diffusivity has a smoothing effect on the discharge profile curvature. The potential profiles for different electrolyte Li^+ diffusivity is shown in Fig. 4.6. Although the starting potential is the same for all three cases, the potential drop slowly builds up and the largest potential drop occurs with the lowest Li^+ diffusivity. In Fig. 4.7, the sensitivity of the solid phase Li^+ diffusivity, $D_{s,pos}$, on discharge potential profile is shown. With decreasing solid phase Li^+ diffusivity, the Li^+ concentration at the surface accumulates more quickly during discharge.

Because the electrode potential is determined by the Li^+ concentration at the particle surface, a cell would reach its cut-off potential faster. Furthermore, unlike the Li^+ concentration gradient in the electrolyte, the Li^+ concentration gradient in the solid phase would not be reflected on the discharge potential profile. Rather, the Li^+ concentration gradient in the solid phase will be reflected in the recovery potential part of the curve.

Transport and kinetic material properties affect the recovery potential in a similar manner to the discharge potential. When a current is suddenly relaxed, the potential drop due to electronic and ionic conductivities would be recovered instantaneously. The reaction rate constant would also have a parallel effect because it also behaves like an ohmic term. However, the Li^+ concentration gradients developed in the electrolyte and the electrode require additional time to disappear. Hence, the slow rise of the recovery potential are due to diffusive transport properties. Typically, Li^+ diffusion in the electrode is at least several orders of magnitude smaller than Li^+ diffusion in the electrolyte. Hence, the time for the recovery potential to reach an equilibrium potential is often dictated by the solid phase Li^+ diffusion coefficient.

Table 4.4 summarizes the sensitivity of the transport and kinetic properties on the electrochemical behavior discussed above. At 1C-rate, the cell capacity is not significantly affected by any transport and kinetic properties. Also the influence of diffusive terms on the starting potential is negligible. As indicated in Table 4.4 column 5, the time for the concentration gradient in the electrolyte to reach a quasi steady state during discharge depends mainly on the electrolyte Li^+ diffusivity. As for the time for the recovery potential to reach a steady state, the solid phase Li^+ diffusivity is the most dominant factor followed by the electrolyte Li^+ diffusivity. Lastly, transport properties of the solid phase, D_s and σ_s, and the reaction rate constant, k, have the biggest influence on the final recovery potential.

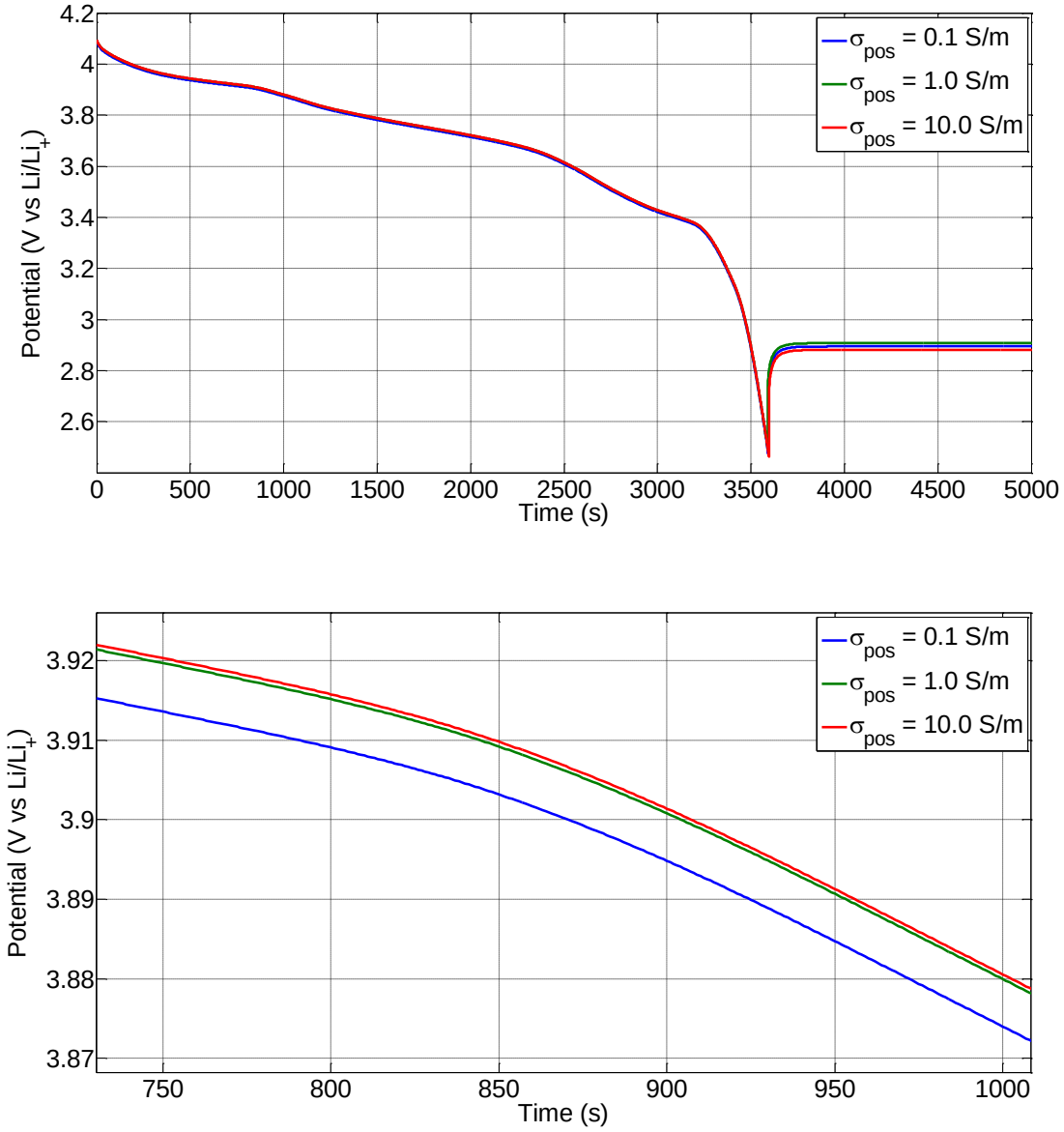

Figure 4.2: (top) The electronic conductivity influence on the cell electrochemical behavior, (bottom) A close-up view of the above figure.

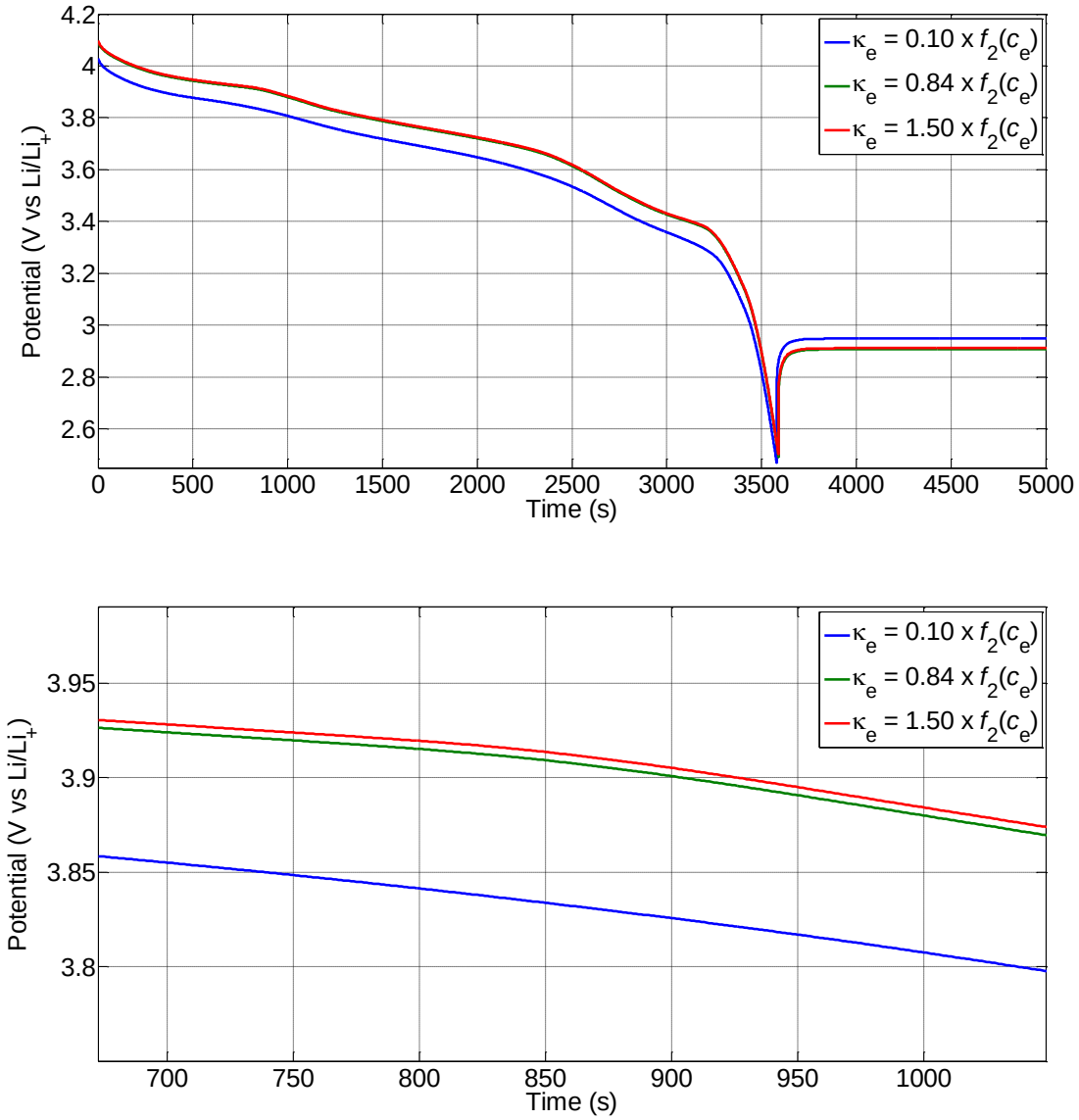

Figure 4.3: (top) The ionic conductivity influence on the cell electrochemical behavior, (bottom) A close-up view of the above figure.

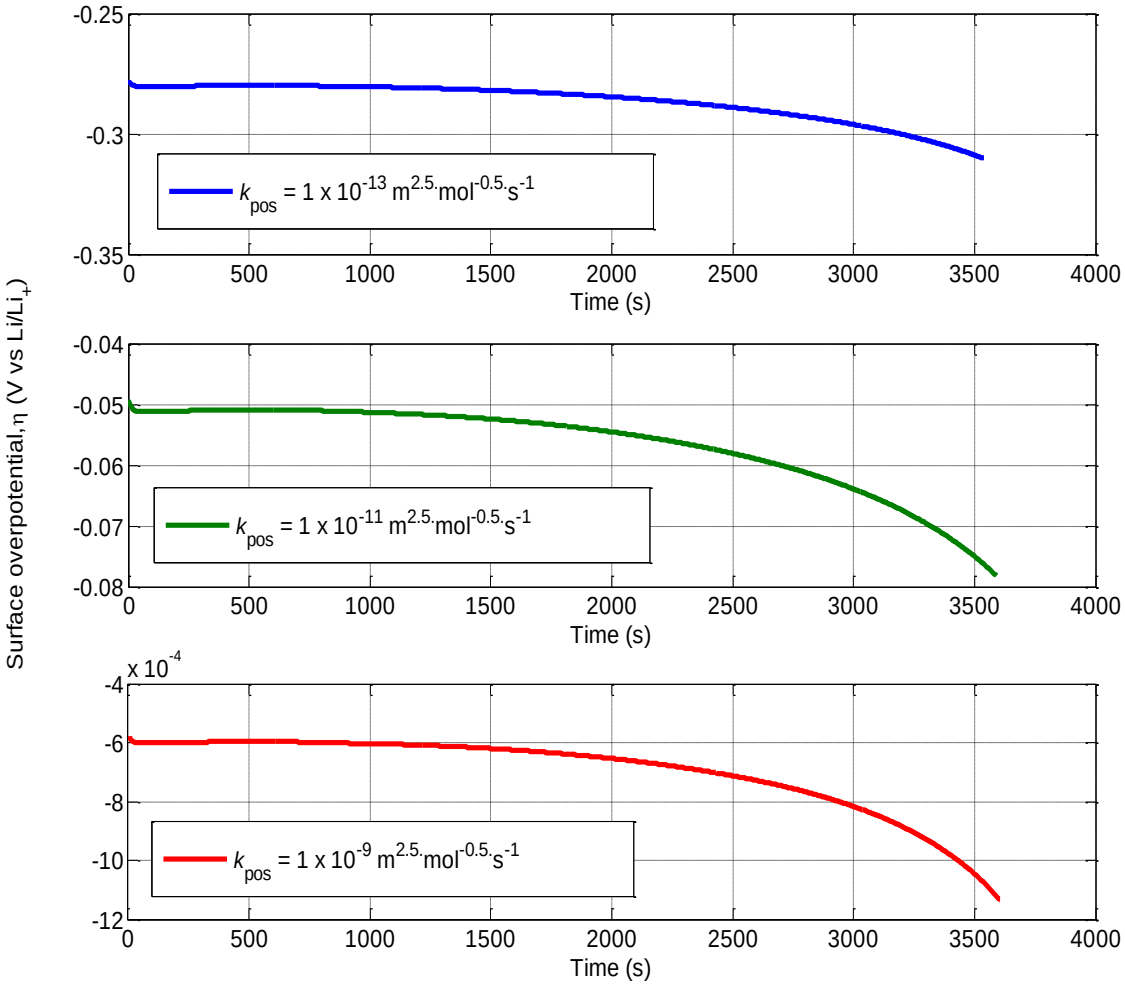

Figure 4.4: Surface overpotential during discharge for various reaction rate constants.

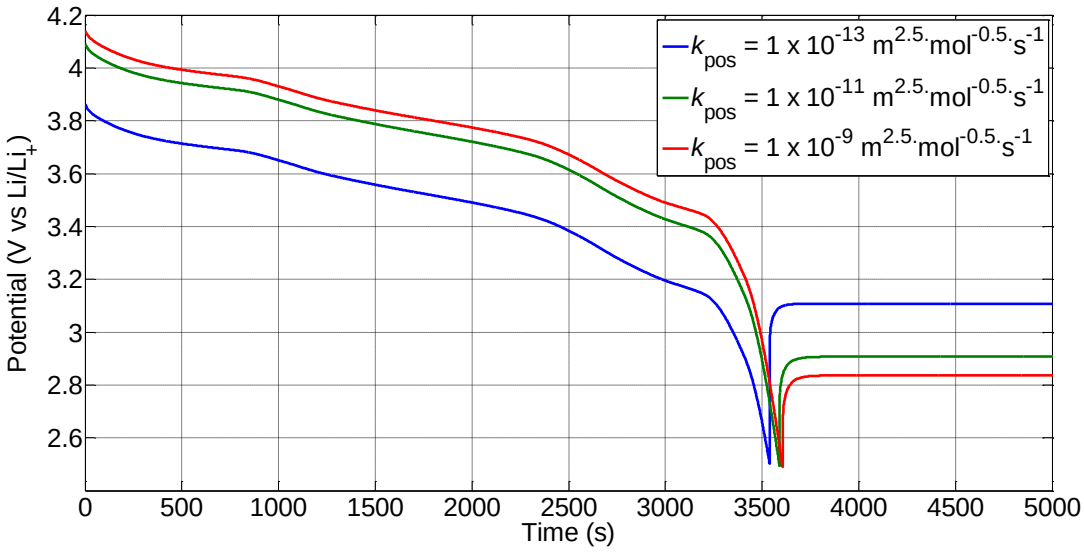

Figure 4.5: Reaction rate constant influence on the cell electrochemical behavior.

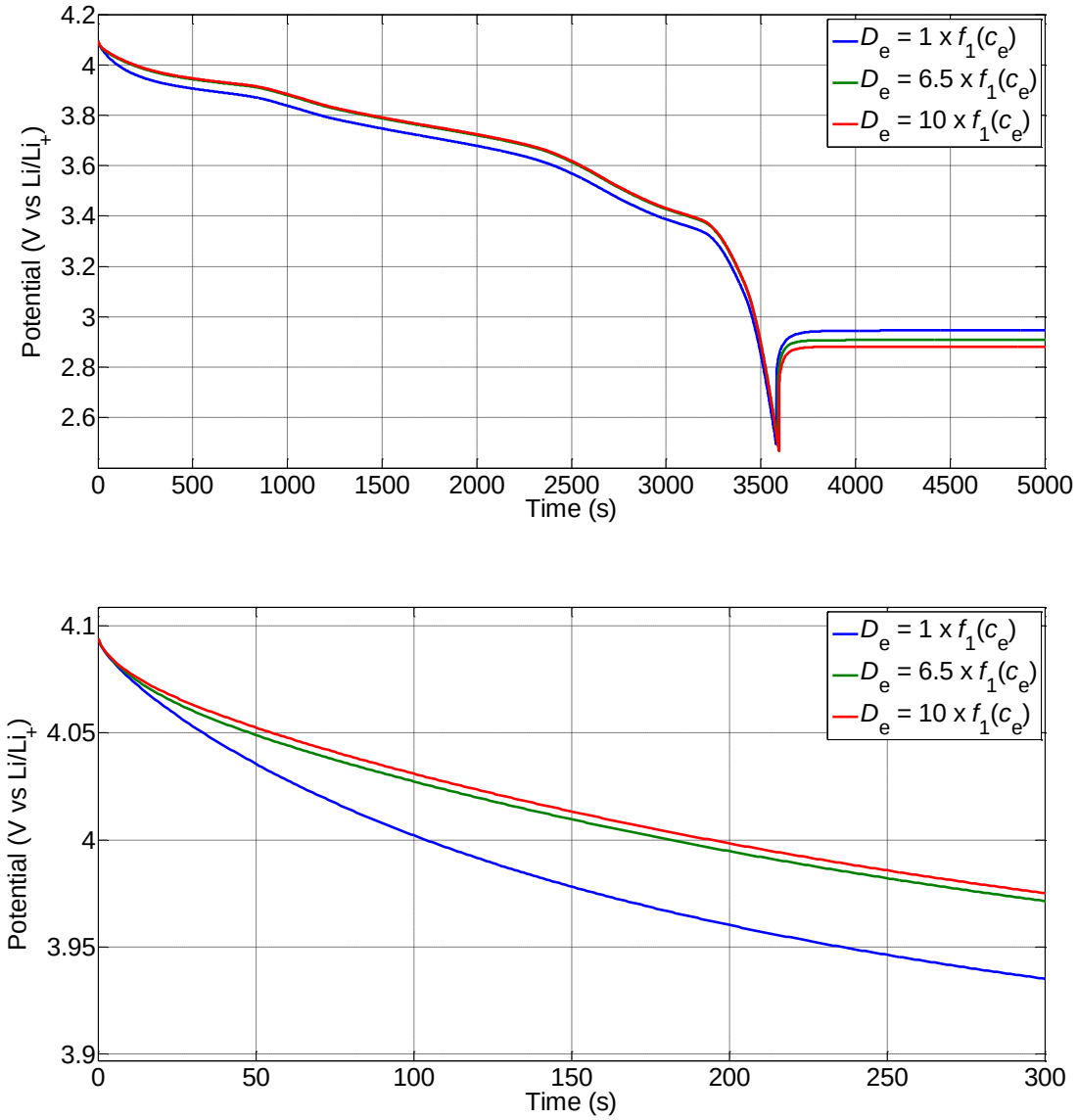

Figure 4.6: (Top) Electrolyte Li^+ diffusivity influence on the electrochemical behavior, (bottom) A close-up view of the above figure.

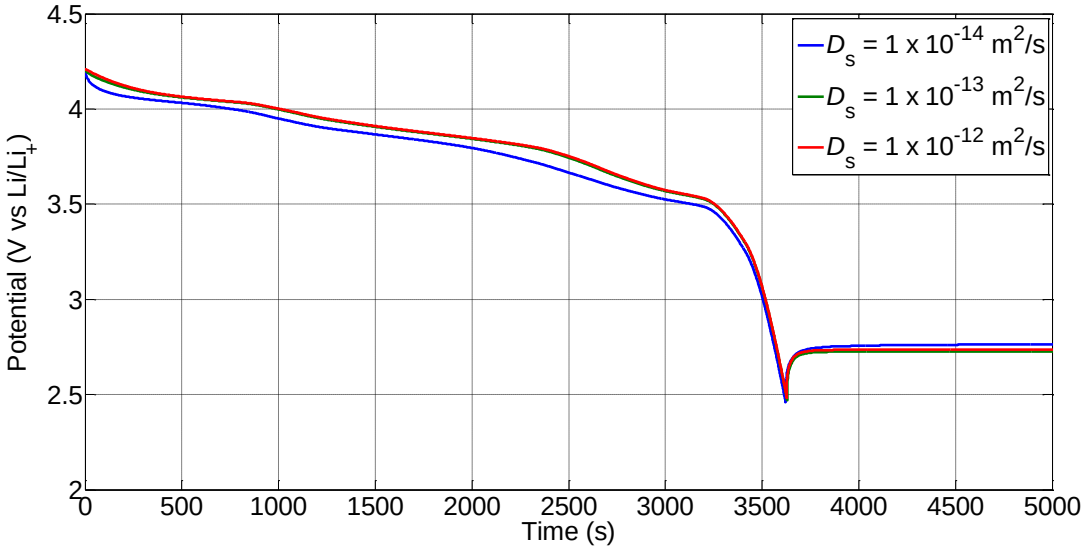

Figure 4.7: Solid phase Li^+ diffusivity influence on the cell electrochemical behavior.

Run	Case	Initial voltage drop	Capacity not utilized	Time for avg. dc_e/dt to reach a quasi steady state	Time taken for recovery potential to reach $dV/dt \leq 1\mu V/s$	Recovered potential
1	baseline	81 mV	1.39 %	58 s	145 s	0.255 V
2	σ_s : Low	130 mV	1.77 %	57 s	126 s	0.318 V
3	σ_s : High	88 mV	1.42 %	57 s	145 s	0.261 V
4	κ_e : Low	90 mV	1.47 %	58 s	147 s	0.262 V
5	κ_e : High	78 mV	1.36 %	58 s	145 s	0.253 V
6	k : Low	184 mV	2.00 %	58 s	143 s	0.359 V
7	k : High	49 mV	1.04 %	64 s	187 s	0.201 V
8	D_e : Low	81 mV	1.64 %	382 s	474 s	0.297 V
9	D_e : High	81 mV	1.36 %	38 s	145 s	0.254 V
10	D_s : Low	88 mV	1.99 %	58 s	1276 s	0.350 V
11	D_s : High	80 mV	1.36 %	58 s	130 s	0.249 V

Table 4.4: A summary of the sensitivity test.

Model Calibration

With the sensitivity study results, the cell model input parameters are calibrated against LG Chem P1.4 cell data. Each cell is discharged from a fully charged state to a cut-off potential of 2.5 V with 1C-rate followed by a current relaxation. Based on the sensitivity study finding, the following procedure is used in the calibration process. First, it is assumed that at an ambient temperature of 25 °C, the electronic conductivities of both negative and positive electrodes are not rate-limiting. The electronic conductivity of graphite greater than 100 $S \cdot m^{-1}$ in the temperature range considered in this study [5]. At the positive electrode side, it is assumed that the electronic conductivity is also not rate-limiting due to the inclusion of conductive additives. Hence, the first step is to adjust the reaction rate constants to fit the starting potential. The second step is to adjust the solid phase Li^+ diffusivity to fit the magnitude of the recovery potential. The next step is adjust the porosity of the two electrodes to fit the cell capacity. Once the simulation curve reasonably matches the experimental data, the calibrated input parameters are used to fit cell discharged with three other C-rates. The last step is to assess the simulation results by comparing specific parts of the curve against the experimental data. Also with the set of calibrated input parameters, potential losses associated with kinetic, transport, and ohmic properties are computed. Figure 4.8 shows the fitted results at an ambient temperature of 25 °C. The discharge portion of the four curves are in a good agreement with the experimental results. However, the recovery portion of the profile is either under- or over-predicted. Moreover, in the simulation, the rate of recovery potential change is faster than the experiments. This indicates that diffusive terms may have been overestimated. The temperature rise between the experiment and the simulation at room temperature is shown in Fig. 4.9.

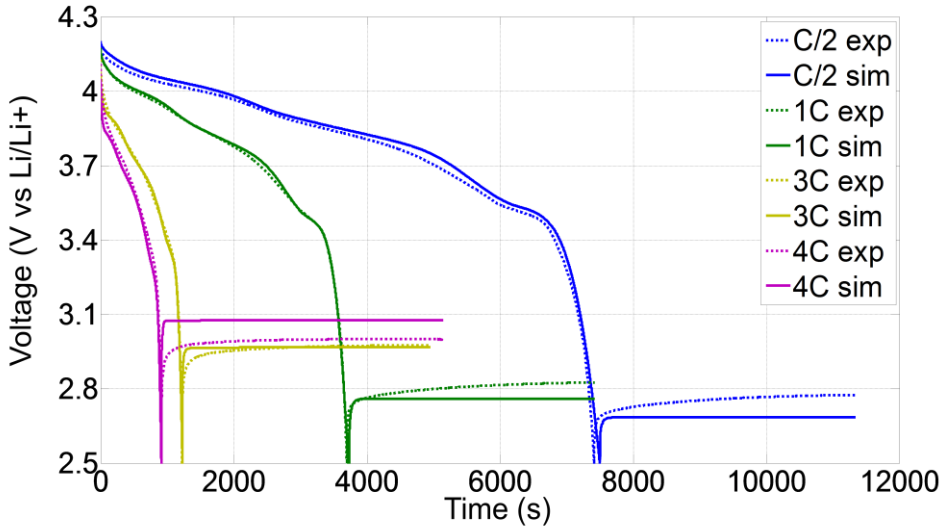

Figure 4.8: Constant current discharge fitting results for various C-rates. The solid lines represent the simulation and the dotted lines represent the experimental measurements.

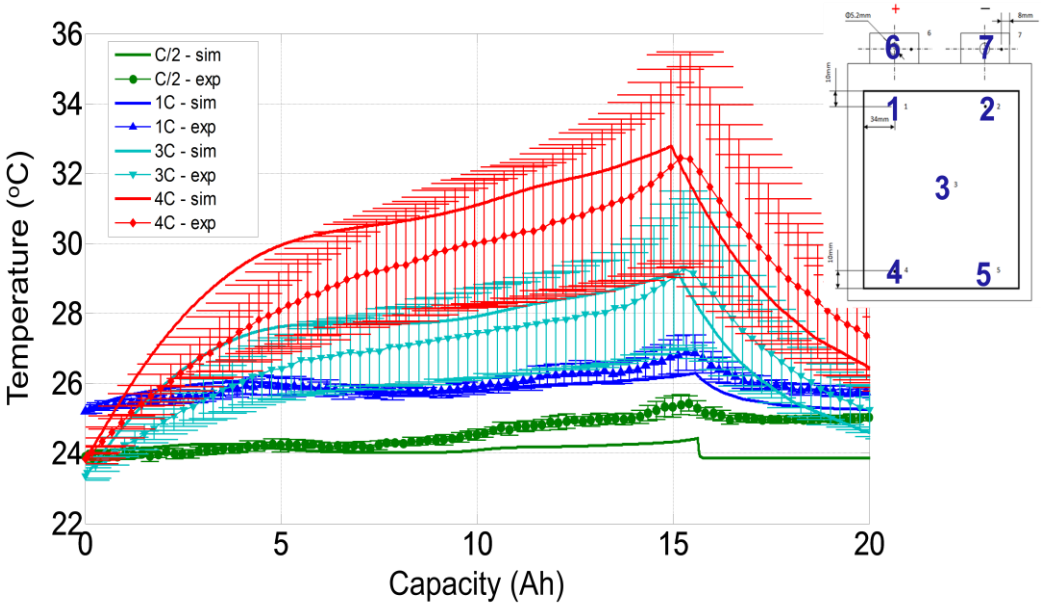

Figure 4.9: Simulation and experiment cell temperature rise comparison. The solid lines represent the simulation and the dotted lines with bars represent the experimental measurements.

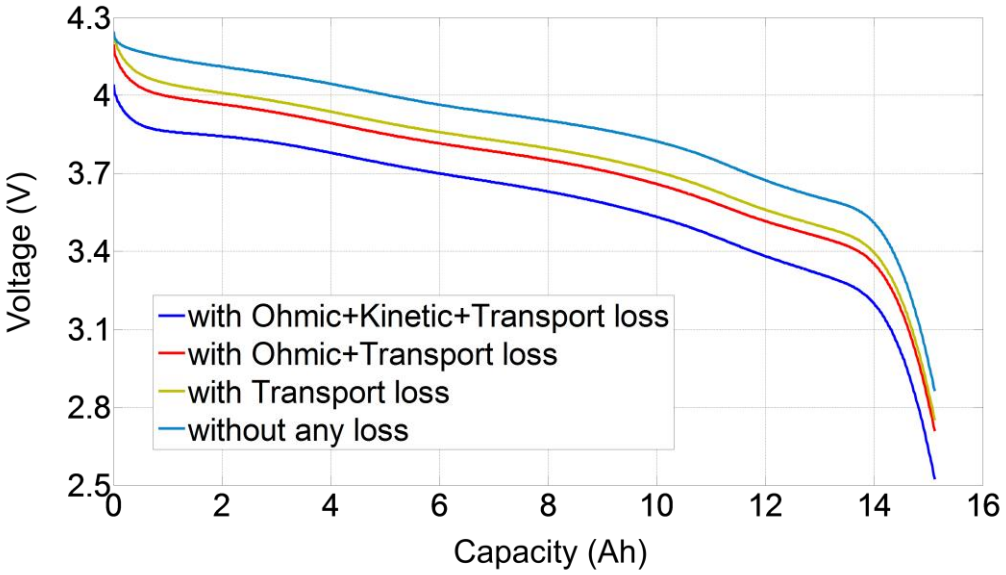

Figure 4.10: 4C discharge profiles with and without various types of losses.

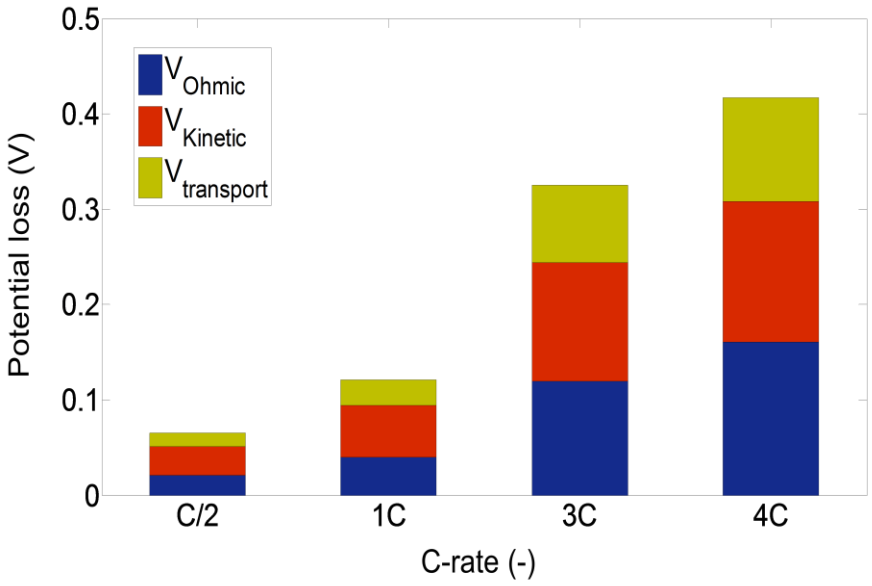

Figure 4.11: Average potential losses associated with different types of material properties.

In Fig. 4.9, the solid lines represent simulation results and the dotted lines represent the average and the standard deviations associated with temperature measurements at seven different locations on the cell. The temperature rise trend from the simulation is in a good agreement with the experimental data. At 4C, the temperature rise in P1.4 cell is approximately 10 °C. Therefore, it is expected that the thermal effect on cell performance is small. For the set of calibrated input cell parameters, potential losses associated with transport, kinetic, and ohmic parameters are computed. Figure 4.10 shows simulated 4C discharge profiles with and without different types of losses. The very bottom profile in Fig. 4.10 is the normal discharge profile in the presence of all types of losses. The three discharge profiles above that represent discharge profiles in the absence of kinetic loss, in the absence of kinetic and ohmic losses, and in the presence of no loss. The average potential loss during at the four different C-rates are calculated and shown in Figure 4.11. According to Fig. 4.11, all types of losses increase with C-rates. Also the kinetic loss is as large as the ohmic loss at all four C-rates, and the combined transport and kinetic loss is greater than the ohmic loss at all four different C-rates.

CONCLUSIONS AND FUTURE WORK

The kinetic loss associated with the reaction rate constant acts as an effective ohmic loss up to about 50 % SOC then increases towards the end-of-discharge. This rise causes a cell to reach a cut-off potential faster. The Li^+ concentration gradient in the electrolyte is reflected in both the discharge and relaxation part of potential profile whereas the Li^+ concentration gradient in the solid phase is reflected only in the relaxation part of the curve. For future work, to improve the fitting of the relaxation potential part of the curve, a more detailed sensitivity study of the electrode and the electrolyte Li^+ diffusivity need to be performed. Also, to investigate the

ambient temperature effect on the cell performance, the same calibration process will be performed with the cell data cycled at different temperatures. To further validate the calibration process, a standard pulse-power test will be simulated and compared with experimental results.

BIBLIOGRAPHY

1. Bernardi, D.; Pawlikowski, E.; Newman, J., A general energy-balance for battery systems. *J. Electrochem. Soc.* **1985,** *132* (1), 5-12.

2. Thomas, K. E.; Bogatu, C.; Newman, J., Measurement of the entropy of reaction as a function of state of charge in doped and undoped lithium manganese oxide. *J. Electrochem. Soc.* **2001,** *148* (6), A570-A575.

3. Lu, W.; Belharouak, I.; Vissers, D.; Amine, K., In situ thermal study of li1+x ni1/3co1/3mn1/3 (1-x)o-2 using isothermal micro-clorimetric techniques. *J. Electrochem. Soc.* **2006,** *153* (11), A2147-A2151.

4. Reynier, Y. F.; Yazami, R.; Fultz, B., Thermodynamics of lithium intercalation into graphites and disordered carbons. *J. Electrochem. Soc.* **2004,** *151* (3), A422-A426.

5. Buerschaper, R. A., Thermal and electrical conductivity of graphite and carbon at low temperatures. *Journal of Applied Physics* **1944,** *15* (5), 452-454.

6. Valoen, L. O.; Reimers, J. N., Transport properties of lipf6-based li-ion battery electrolytes. *J. Electrochem. Soc.* **2005,** *152* (5), A882-A891.

7. Takami, N.; Satoh, A.; Hara, M.; Ohsaki, I., Structural and kinetic characterization of lithium intercalation into carbon anodes for secondary lithium batteries. *J. Electrochem. Soc.* **1995,** *142* (2), 371-379.

8. Umeda, M.; Dokko, K.; Fujita, Y.; Mohamedi, M.; Uchida, I.; Selman, J. R., Electrochemical impedance study of li-ion insertion into mesocarbon microbead single particle electrode part 1. Graphitized carbon. *Electrochim. Acta* **2001,** *47* (6), 885-890.

9. Shim, J.; Striebel, K. A., Electrochemical characterization of thermally oxidized natural graphite anodes in lithium-ion batteries. *Journal of Power Sources* **2007,** *164* (2), 862-867.

10. Levi, M. D.; Aurbach, D., Diffusion coefficients of lithium ions during intercalation into graphite derived from the simultaneous measurements and modeling of electrochemical impedance and potentiostatic intermittent titration characteristics of thin graphite electrodes. *J. Phys. Chem. B* **1997,** *101* (23), 4641-4647.

11. Shui, M.; Gao, S.; Shu, J.; Zheng, W. D.; Xu, D.; Chen, L. L.; Feng, L.; Ren, Y. L., Lini1/3co1/3mn1/3o2 cathode materials for lib prepared by spray pyrolysis. Ii. Li+ diffusion kinetics. *Ionics* **2013,** *19* (1), 47-52.

12. Zhang, X.; Mauger, A.; Jiang, W. J.; Groult, H.; Julien, C. M., Diffusion of li+ ions in lini1/3mn1/3co1/3o2. In *Nanostructured materials for energy storage and conversion*, Zaghib, K.; Chiu, W.; Ramani, V.; Liaw, B. Y.; Julien, C.; Mustain, W.; VanSchalkwijk, W., Eds. Electrochemical Soc Inc: Pennington, 2011; Vol. 35, pp 89-94.

13. Deng, J. Q.; Xi, L. J.; Wang, L. H.; Wang, Z. M.; Chung, C. Y.; Han, X. D.; Zhou, H. Y., Electrochemical performance of lini1/3co1/3mn1/3o2 thin film electrodes prepared by pulsed laser deposition. *Journal of Power Sources* **2012,** *217*, 491-497.

14. Guyomard, D.; Tarascon, J. M., Li metal-free rechargeable limn2o4/carbon cells - their understanding and optimization. *J. Electrochem. Soc.* **1992,** *139* (4), 937-948.

15. Kanoh, H.; Feng, Q.; Hirotsu, T.; Ooi, K., Ac impedance analysis for li+ insertion of a pt/lambda-mno2 electrode in an aqueous phase. *J. Electrochem. Soc.* **1996,** *143* (8), 2610-2615.

16. Dokko, K.; Nishizawa, M.; Mohamedi, M.; Umeda, M.; Uchida, I.; Akimoto, J.; Takahashi, Y.; Gotoh, Y.; Mizuta, S., Electrochemical studies of li-ion extraction and insertion of limn2o4 single crystal. *Electrochem. Solid State Lett.* **2001,** *4* (9), A151-A153.

17. Molenda, J.; Swierczek, K.; Kucza, W.; Marzec, J.; Stoklosa, A., Electrical properties of limn2o4-delta at temperatures 220-1100k. *Solid State Ionics* **1999,** *123* (1-4), 155-163.

18. Marzec, J.; Swierczek, K.; Przewoznik, J.; Molenda, J.; Simon, D. R.; Kelder, E. M.; Schoonman, J., Conduction mechanism in operating a limn2o4 cathode. *Solid State Ionics* **2002,** *146* (3-4), 225-237.

19. Hussain, O. M.; Krishna, K. H.; Vani, V. K.; Julien, C. M., Structural and electrical properties of lithium manganese oxide thin films grown by pulsed laser deposition. *Ionics* **2007,** *13* (6), 455-459.

20. Nakamura, K.; Shimokita, K.; Sakamoto, Y.; Hirano, H.; Michihiro, Y.; Moriga, T., Power law behaviors of electrical conductivities in lithium manganese oxides. *Solid State Ionics* **2012,** *225*, 538-541.

21. Doyle, M.; Newman, J.; Gozdz, A. S.; Schmutz, C. N.; Tarascon, J. M., Comparison of modeling predictions with experimental data from plastic lithium ion cells. *J. Electrochem. Soc.* **1996,** *143* (6), 1890-1903.

22. Gu, W. B.; Wang, C. Y., *Thermal-electrochemical coupled modeling of a lithium-ion cell*. Electrochemical Society Inc: Pennington, 2000; Vol. 99, p 748-762.

23. Arora, P.; Doyle, M.; White, R. E., Mathematical modeling of the lithium deposition overcharge reaction in lithium-ion batteries using carbon-based negative electrodes. *J. Electrochem. Soc.* **1999,** *146* (10), 3543-3553.

24. Zhang, D.; Popov, B. N.; White, R. E., Modeling lithium intercalation of a single spinel particle under potentiodynamic control. *J. Electrochem. Soc.* **2000,** *147* (3), 831-838.

25. Santhanagopalan, S.; Guo, Q. Z.; Ramadass, P.; White, R. E., Review of models for predicting the cycling performance of lithium ion batteries. *Journal of Power Sources* **2006,** *156* (2), 620-628.

26. Kumaresan, K.; Sikha, G.; White, R. E., Thermal model for a li-ion cell. *J. Electrochem. Soc.* **2008,** *155* (2), A164-A171.

27. Kondo, K.; Sano, M.; Hiwara, A.; Omi, T.; Fujita, M.; Kuwae, A.; Iida, M.; Mogi, K.; Yokoyama, H., Conductivity and solvation of li+ ions of lipf6 in propylene carbonate solutions. *J. Phys. Chem. B* **2000,** *104* (20), 5040-5044.

28. Sun, X.; Lee, H. S.; Yang, X. Q.; McBreen, J., Improved elevated temperature cycling of limn2o4 spinel through the use of a composite lif-based electrolyte. *Electrochem. Solid State Lett.* **2001,** *4* (11), A184-A186.

29. Ding, M. S.; Jow, T. R., How conductivities and viscosities of pc-dec and pc-ec solutions of libf4, lipf6, libob, et4nbf4, and et4npf6 differ and why. *J. Electrochem. Soc.* **2004,** *151* (12), A2007-A2015.

30. Mauro, V.; D'Aprano, A.; Croce, F.; Salomon, M., Direct determination of transference numbers of liclo4 solutions in propylene carbonate and acetonitrile. *Journal of Power Sources* **2005,** *141* (1), 167-170.

31. Zhao, J. S.; Wang, L.; He, X. M.; Wan, C. R.; Jiang, C. Y., Determination of lithium-ion transference numbers in lipf6-pc solutions based on electrochemical polarization and nmr measurements. *J. Electrochem. Soc.* **2008,** *155* (4), A292-A296.

32. Stewart, S.; Newman, J., Measuring the salt activity coefficient in lithium-battery electrolytes. *J. Electrochem. Soc.* **2008,** *155* (6), A458-A463.

33. Chen, S. C.; Wang, Y. Y.; Wan, C. C., Thermal analysis of spirally wound lithium batteries. *J. Electrochem. Soc.* **2006,** *153* (4), A637-A648.

34. Qiu, X. Y.; Zhuang, Q. C.; Zhang, Q. Q.; Cao, R.; Qiang, Y. H.; Ying, P. Z.; Sun, S. G., Investigation of layered lini1/3co1/3mn1/3o2 cathode of lithium ion battery by electrochemical impedance spectroscopy. *J. Electroanal. Chem.* **2012,** *687*, 35-44.

35. Smart, M. C.; Whitacre, J. F.; Ratnakumar, B. V.; Amine, K., Electrochemical performance and kinetics of li1+x(co1/3ni1/3mn1/3)(1-x)o-2 cathodes and graphite anodes in low-temperature electrolytes. *Journal of Power Sources* **2007,** *168* (2), 501-508.

36. Yamada, I.; Abe, T.; Iriyama, Y.; Ogumi, Z., Lithium-ion transfer at limn2o4 thin film electrode prepared by pulsed laser deposition. *Electrochem. Commun.* **2003,** *5* (6), 502-505.

37. Abe, T.; Sagane, F.; Ohtsuka, M.; Iriyama, Y.; Ogumi, Z., Lithium-ion transfer at the interface between lithium-ion conductive ceramic electrolyte and liquid electrolyte - a key to enhancing the rate capability of lithium-ion batteries. *J. Electrochem. Soc.* **2005,** *152* (11), A2151-A2154.

38. Jow, T. R.; Marx, M. B.; Allen, J. L., Distinguishing li+ charge transfer kinetics at nca/electrolyte and graphite/electrolyte interfaces, and nca/electrolyte and lfp/electrolyte interfaces in li-ion cells. *J. Electrochem. Soc.* **2012,** *159* (5), A604-A612.

39. Prada, E.; Di Domenico, D.; Creff, Y.; Bernard, J.; Sauvant-Moynot, V.; Huet, F., Simplified electrochemical and thermal model of lifepo4-graphite li-ion batteries for fast charge applications. *J. Electrochem. Soc.* **2012,** *159* (9), A1508-A1519.

40. Wang, L.; Zhao, J. S.; He, X. M.; Gao, J.; Li, J. J.; Wan, C. R.; Jiang, C. Y., Electrochemical impedance spectroscopy (eis) study of lini1/3co1/3mn1/3o2 for li-ion batteries. *Int. J. Electrochem. Sci.* **2012,** *7* (1), 345-353.

CHAPTER V

CONCLUSIONS AND FUTURE WORK

Various transport and kinetic phenomena that affect the Li-ion cell rate capability are discussed in this study. Phenomena inside a cell typically occur in sequence during cell operation. Therefore, given a set of fixed transport and kinetic material properties, the slowest transport and kinetic process will dictate the cell rate capability. However, many transport and kinetic parameters are a function of Li^+ concentration, temperature, aging mechanisms, and even loading conditions. Therefore, a rate-limiting factor can change and will depend on the overall cell operating condition.

A Li-ion cell model with a particle containing grain boundaries was modeled to investigate the grain boundary effect on Li^+ diffusivity as well as Li^+ intercalation-induced stress. A Voronoi grain size distribution is used in creating particles with different grain boundary densities. It was found that with increasing grain boundary density, not only the particle capacity utilization is enhanced but also the maximum intercalation-induced stress is reduced by lowering the Li^+ concentration gradient inside a particle. In addition, the Li^+ diffusivity enhancement due to grain boundaries could significantly outweigh the enhancement due to intercalation-induced stress gradient. Depending on the crystal structures of active materials, the Li^+ diffusion pathway can be one-, two-, and three-dimensional. Therefore, an inclusion of the anisotropic Li^+ diffusivity effect into the model will be valuable in assessing various other types of Li-ion active materials. Volumetric strains of $LiMn_2O_4$ active material particles were measured using *in-situ*

AFM system. The volumetric strain measurements can be used in validating the stress level developed in particles of different shapes and sizes. Also the Li^+ diffusivity enhancement due to intercalation-induced stress field was approximated numerically using a modified GITT method. For $LiMn_2O_4$ materials, the order of the intercalation-induced Li^+ diffusivity enhancement is comparable to the thermodynamic factor that enhances Li^+ diffusivity.

The sensitivity of various cell transport and kinetic material properties on cell electrochemical behavior was investigated using an isothermal electrochemical P2D model. Based on the sensitivity study, it was found that different types of material properties can affect different parts of cell operating potentials. Using the sensitivity study finding as a guideline, material properties of a commercial cell were estimated using a thermal-electrochemical P2D model. For the given commercial cell, the combined potential loss due to transport and kinetic losses was greater than the potential loss due to ohmic loss regardless of current discharge rate. Future work related to this work is proposed in the following:

- A detailed sensitivity study of electrode and electrolyte Li^+ diffusivities on the voltage relaxation part of the curve. The study finding may improve the accuracy of Li^+ diffusivity estimation.
- The literature suggests that reaction rate constants may depend on C-rates as well as the direction of electrochemical reaction. Moreover, the effective reaction rate constants will likely evolve due to chemical degradation mechanisms at the electrode-electrolyte interface. Hence, an experimental study related to measuring the reaction rate constants is suggested.